

Dipl. Natw. ETH Martin Ritter

**A landmark-based method
for the geometrical 3D calibration
of scanning microscopes**

Die vorliegende Arbeit entstand am Heinrich-Pette-Institut für Experimentelle Virologie und Immunologie an der Universität Hamburg (HPI) und am Institut für Geodäsie und Geoinformationstechnik der Technischen Universität Berlin.

Impressum

**A landmark-based method for the geometrical
3D calibration of scanning microscopes**

2007

Herausgeber:

Bundesanstalt für Materialforschung und -prüfung (BAM)

Unter den Eichen 87

12205 Berlin

Telefon: +49 30 8104-0

Telefax: +49 30 8112029

E-Mail: info@bam.de

Internet: www.bam.de

Copyright © 2007 by Bundesanstalt für
Materialforschung und -prüfung (BAM)

Verlag und Vertrieb:

Wirtschaftsverlag NW

Verlag für neue Wissenschaft GmbH

27568 Bremerhaven

Telefon: +49 471 94544-0

Telefax: +49 471 94544-77

Layout: BAM-Arbeitsgruppe Z.64

ISSN 1613-4249

ISBN 978-3-86509-630-2

A landmark-based method for the geometrical 3D calibration of scanning microscopes

vorgelegt von
Dipl. Natw. ETH Martin Ritter
aus Ruggell, Fürstentum Liechtenstein

von der Fakultät VI
der Technischen Universität Berlin
zur Erlangung des akademischen Grades

Doktor der Ingenieurwissenschaften
– Dr.-Ing. –

genehmigte Dissertation

Vorsitzender: Prof. Dr.-Ing. Lothar Gründig
Gutachter: Prof. Dr.-Ing. Olaf Hellwich
Prof. Dr.-Ing. Jörg Albertz
Dr. rer. nat. Heinz Hohenberg

Tag der wissenschaftlichen Aussprache: 30. Oktober 2006

Berlin 2007
D 83

ABSTRACT

This thesis presents a new strategy and a spatial method for the geometric calibration of 3D measurement devices at the micro-range, based on spatial reference structures with nanometer-sized landmarks (nanomarkers). The new method was successfully applied for the 3D calibration of scanning probe microscopes (SPM) and confocal laser scanning microscopes (CLSM). Moreover, the spatial method was also used for the photogrammetric self-calibration of scanning electron microscopes (SEM).

In order to implement the calibration strategy to all scanning microscopes used, the landmark-based principle of reference points often applied at land survey or at close-range applications has been transferred to the nano- and micro-range in the form of nanomarker. In order to function as a support to the nanomarkers, slope-shaped step pyramids have been developed and fabricated by focused ion beam (FIB) induced metal deposition. These FIB produced 3D microstructures have been sized to embrace most of the measurement volume of the scanning microscopes. Additionally, their special design allows the homogenous distribution of the nanomarkers. The nanomarkers were applied onto the support and the plateaus of the slope-step pyramids by FIB etching (milling) as landmarks with as little as several hundreds of nanometers in diameter. The nanomarkers are either of point-, or ring-shaped design. They are optimized so that they can be spatially measured by SPM and CLSM, and, imaged and photogrammetrically analyzed on the basis of SEM data. The centre of the each nanomarker serves as reference point in the measurement data or images. By applying image processing routines, the image (2D) or object (3D) coordinates of each nanomarker has been determined with subpixel accuracy.

In contrast to the spatial reference structures applied for the spatial calibration method introduced here, present calibration methods for scanning microscopes use sequential measurements of 2D lattice and height step structures. This means that the determination of the scale factor for the height measurement yields an average value for the full scan area. Thus, the height scale factor remains independent of the lateral scanning position, and, therefore, it will be impossible to determine the coupling of the lateral coordinate axes and the z-axis as a shear factor with the sequential calibration method. On this account, an affine geometrical model has been used here, that allows for scale factors in all space directions, and, for coupling between all coordinate axes. With the help of the correlative analysis of the measurement data of all measurement methods applied (SPM, CLSM and photogrammetric SEM), for the first time, all scale factors, as well as the linear coupling of the probes used for the height measurement could be determined dependent on the lateral scanning position.

It could be shown that the scanning movement of the SPM and the CLSM is erroneous. Due to hysteresis effects and guidance errors of the scanning generators,

due to errors and peculiarities of the control cycle, and because of misaligned attachment of the probe with respect to the scanning plane, the measurement coordinate system is not identical to the ideal reference coordinate system. Scale and orthogonality of the measurement coordinate system have to be calibrated and corrected, in order to maintain the traceability to the SI-unit meter, and, therefore, to allow for quantitative dimensional 3D measurements. However, the correlative analysis of the SPM, CLSM and photogrammetric SEM measurement data after 3D calibration resulted in mean residues in the measured coordinates of as little as 13 nm. Without the coupling factors the mean residues are up to 6 times higher. By taking into account the orthogonality of the measurement coordinate axes when performing a 3D calibration, a comparative and quantitative analysis of 3D scanning microscopy has been made possible.

ZUSAMMENFASSUNG

Die vorgelegte Arbeit stellt ein neue Strategie und ein daraus abgeleitetes Verfahren zur geometrischen Kalibrierung von 3D Messgeräten im Mikrobereich vor. Das Verfahren beruht auf der Anwendung von räumlichen Kalibrierstrukturen mit Nanomessmarken (Nanomarker). Es konnte erfolgreich für die 3D Kalibrierung von Rasterkraftmikroskopen (SPM) und konfokalen Laserrastermikroskopen (CLSM) eingesetzt werden. Im Rahmen von vergleichenden Untersuchungen wurden die 3D Kalibrierstrukturen ebenfalls für die photogrammetrische Selbstkalibrierung im Rasterelektronenmikroskop (SEM) verwendet.

Für die Umsetzung der Kalibrierstrategie wurde sowohl für die eigentliche 3D Kalibrierung, als auch für die photogrammetrische Selbstkalibrierung, das in der Nahbereichsphotogrammetrie verwendete Prinzip von Messmarken in Form von Nanomarkern auf den Mikro- und Nanobereich übertragen. Als Träger für die Nanomarker dienen neu entwickelte, räumliche Mikrostrukturen in Gestalt von mehrstufigen Pyramiden mit schrägen Seitenflanken, hergestellt mit der Technologie der Focused Ion Beam (FIB) induzierten Metalldeposition. Die 3D Mikrostrukturen sind so konzipiert, dass sie den grössten Teil des Messvolumens von Rasterkraftmikroskopen erfassen und durch ihre Form die gleichmässige Verteilung der Nanomarker im Messvolumen der Rastergeräte ermöglichen.

Die Nanomarker wurden durch FIB-Ätzung (Milling) als Messmarken mit einem Durchmesser von wenigen 100 Nanometern auf die Basis und die Stufenplateaus der pyramidalen Mikrostrukturen aufgebracht. Die Nanomarker besitzen eine optimale Gestalt, welche sowohl eine optimale räumliche Messung mit SPM und CLSM erlaubt, als auch die photogrammetrische Berechnung der Koordinaten der Nanomarker bei Aufnahmen der Kalibrierstrukturen im SEM. Die Mittelpunkte der Nanomarker dienen als Referenzpunkte in den Messdaten, deren Bild- bzw. Objektkoordinaten mit Hilfe von digitalen Bildverarbeitungsmethoden in Subpixelgenauigkeit bestimmt wurden.

Im Gegensatz zu den hier verwendeten räumlichen Referenzstrukturen beruhen bisherige Kalibriermethoden für Rastermikroskope auf sequentiellen Kalibriermessungen von 2D Gitter- und Höhenstrukturen. Das bedeutet, dass die Bestimmung des Massstabsfaktors für die Höhenmessung einer Mittelwertbildung über den gesamten Datensatz entspricht, und damit unabhängig ist von der jeweiligen lateralen Rasterposition. Daher ist es mit dem sequentiellen Kalibrierverfahren nicht möglich, Kopplungen zwischen den lateralen Koordinatenachsen und der z-Achse in Form eines Scherungsfaktors zu bestimmen. Aus diesem Grund wurde für die hier vorgestellte 3D Kalibrierung ein geometrisches Modell verwendet, welches Massstabsfaktoren in alle Raumrichtungen, und Achsenkopplungen zwischen allen Koordinatenachsen zulässt. Mit der korrelativen Analyse der Messdaten der drei Messmethoden (SPM, CLSM

und photogrammetrische SEM) konnten erstmals direkt alle Massstäbe, sowie lineare Kopplungen der im jeweiligen Messgerät verwendeten Sonde für die Höhenmessung in Abhängigkeit von ihrer lateralen Messposition erfasst werden.

Es zeigte sich, dass die während der Messungen mit SPM und CLSM ausgeführte Rasterbewegung fehlerbehaftet ist. Durch Hystereseeffekte und Führungsabweichungen der Rastergeneratoren, durch Fehler und Eigenheiten im Regelkreis, in der Anbringung der Sonde sowie in der Signaldetektion weicht das Messkoordinatensystem der Mikroskope von einem idealen Referenzkoordinatensystem ab. Massstab und Orthogonalität der Achsen der Messkoordinatensysteme müssen kalibriert und korrigiert werden, um die Messpunktabstände auf die SI-Einheit Meter zurückzuführen und damit quantitative 3D Messungen zu ermöglichen.

Die korrelative Analyse der SPM, CLSM und SEM Messdaten der Nanomarker ergab bei Berücksichtigung aller ermittelten Kalibrierparameter Restdifferenzen von minimal etwa 13 nm. Ohne Verwendung der Kopplungsparameter zwischen den lateralen und der vertikalen Achsen liegt der Wert um bis zu sechs Mal höher. Durch die Berücksichtigung der räumlichen Kopplungen bei der 3D Kalibrierung ist also erstmals eine direkte Vergleichbarkeit von Rasterverfahren im Mikro- und Nanobereich möglich geworden.

ABBREVIATIONS

1D, 2D, 3D	One-dimensional, two-dimensional, three-dimensional
AFM	Atomic force microscopy, atomic force microscope
BSE	Backscattered electrons
CLSM	Confocal laser scanning microscope
dpi	Dots per inch
EM	Electron microscopy, electron microscope
ESEM	Enironmental scanning electron microscope
FEG	Field emission gun
FIB	Focused ion beam
FOV	Field of view
FWHM	Full width half maximum
Ga	Gallium
GIS	Gas insertion system
GUI	Graphical user interface
HFV	Horizontal field width
IC	Integrated circuit
kV	Kilo Volt
LaB ₆	Lanthanium hexaboride
LMIS	Liquid metal ion source
LSE	Least-squares estimation
metSPM	metrological SPM
Pt	Platinum
PTB	Physikalisch-Technische Bundesanstalt
PWD	Patterning working distance
ROI	Region of Interest
SE	Secondary electrons
SEM	Scanning electron microscopy, scanning electron microscope
SI	Secondary ions
SNR	Signal-to-noise ratio
SPM	Scanning probe microscope, scanning probe microscopy
TEM	Transmission electron microscopy, transmission electron microscope
W	Tungsten

CONTENTS

Abstract	iii
Zusammenfassung	v
Abbreviations	vii
1 Introduction	1
2 3D Scanning Microscopy	5
2.1 Principles of scanning microscopy	5
2.1.1 Scanning parameters	6
2.1.2 The scanning movement	6
2.1.3 Magnification and scale	7
2.1.4 Digital signal processing	7
2.2 Scanning probe microscopy (SPM)	9
2.2.1 Foundations of atomic force microscopy (AFM)	10
2.2.2 Measurement modes of AFM	13
2.3 Scanning electron microscopy (SEM)	14
2.3.1 Foundations of SEM	15
2.3.2 SEM signal formation	16
2.3.3 Fundamental terms in electron optics	17
2.3.4 Environmental SEM	21
2.4 Photogrammetric SEM	23
2.4.1 Photogrammetry	24
2.4.2 Photogrammetric analysis of SEM data	27
2.5 Confocal laser scanning microscopy (CLSM)	29
2.5.1 Confocal principle	29
2.5.2 Basic terms of CLSM	30
2.5.3 CLSM application	30
3 Landmark-based 3D calibration	33
3.1 Coordinate measurements	33
3.1.1 General aspects of measuring	33
3.1.2 Landmark-based calibration	34
3.1.3 Calibration by parameter estimation	35
3.2 SPM and CLSM calibration model	36
3.2.1 Two-step SPM calibration parameter retrieval	37
3.2.2 One-step SPM and CLSM calibration model	38
3.3 Photogrammetric SEM calibration	41
3.3.1 Calibration standards for SEM	41

3.3.2	SEM calibration	42
4	FIB 3D calibration object fabrication	45
4.1	The focused ion beam instrument	45
4.1.1	Principles of FIB	46
4.1.2	Application of FIB	46
4.1.3	The liquid metal ion source	47
4.1.4	Beam-solid interactions	48
4.1.5	Imaging Detectors	49
4.2	Patterning modes	49
4.2.1	Milling	50
4.2.2	Deposition	52
4.3	FIB fabrication of 3D calibration structures	54
4.3.1	Design guidelines	55
4.3.2	Nanomarker design	57
4.4	FIB-fabrication of reference structures	60
4.4.1	Sample preparation for FIB	60
4.4.2	Parameters of the deposition process	61
4.4.3	Automatizing the FIB production process	64
4.4.4	Results	66
4.5	SPM measurement of Arrays A and F	68
4.5.1	SPM measurement setup	68
4.5.2	AFM measurement results	69
4.6	Accuracy of FIB deposition	72
5	Control point determination	75
5.1	Coordinate determination strategy	75
5.2	Template matching by correlation	76
5.2.1	Cross-correlation	77
5.2.2	Subpixel coordinate determination	77
5.2.3	Template centering and adjustment	79
5.3	Coordinate accuracy in synthetic data	85
5.3.1	Ellipse fitting accuracy	85
5.3.2	Template matching accuracy	86
5.4	Coordinate accuracy in real data	88
5.4.1	Image coordinate determination	90
5.4.2	Object coordinate determination	92
6	Metrology and industry application	95
6.1	Photogrammetric calibration of SEM	95
6.1.1	Characterization of positioning and tilting stages	97
6.1.2	Full SEM calibration	102
6.1.3	Calibration of XL30 ESEM	106
6.2	One-step 3D calibration	107
6.2.1	SPM 3D calibration	107
6.2.2	CLSM 3D calibration	109
6.3	Correlative measurements	111

6.3.1	Landmark-based correlative measurements	111
6.3.2	Systematic error analysis by correlative measurements	112
7	Discussion and outlook	117
	Bibliography	123
	Acknowledgements	133

CHAPTER 1

INTRODUCTION

A major factor in the success of technologies and structural research in the micro- and nanometer range has been the ability to visualize small features and to measure at this scale (fig. 1.1). The invention of electron microscopes (EM) opened the gate to a world below the resolution of light microscopes. By the use of electrons instead of light, geometrical features of micro- and nanostructures could be determined. For a long time, only the scanning electron microscope (SEM) and the transmission electron microscope (TEM) were able to reach nanometer resolution. Later on, when scanning probe microscopy (SPM) was invented, the field of nanotechnology evolved, which today is very important to research and technique, and not just due to its interdisciplinary character.

Together with the confocal laser scanning microscope (CLSM), the SPM and the SEM belong to the most common measurement tools applied in life-sciences, materials research, quality control and metrology at micro-range and below for 2D and 3D analysis [Wendt 94, Joy 00, Yoshida 03]. SPM and CLSM allow direct 2.5 or 3D

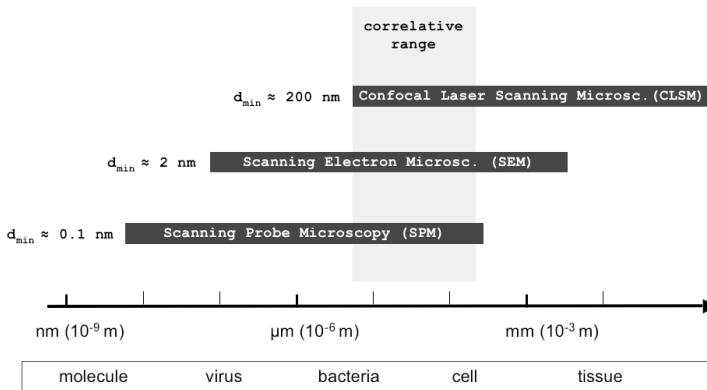


Figure 1.1: Lateral resolution and range of common scanning microscope techniques

coordinate measurements, respectively. In the case of SEM, the spatial information has to be reconstructed indirectly from the images, e.g. by photogrammetric means.

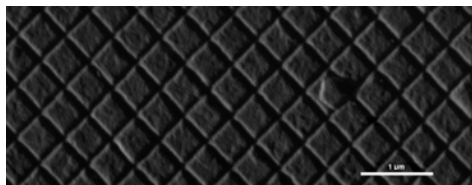
Quantitative scanning microscopy

Although scanning microscopy is often used for the sake of imaging, visualization and qualitative analysis, it is more and more applied for quantitative 3D measure-

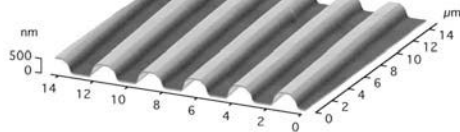
ments, especially in the field of nanotechnology, where dimensional metrology aspects of measurements are critical [Schattenburg 02], or, as [Wilkening 04] states: “Measurements are the backbone of all research and development. Production and quality assurance even require quantitative and traceable measurements, respectively. And such is valid also for the nano-world: a reliable production requires accurate measuring”. However, establishing coordinate measurement devices for the micro-scale and nano-range that are traceable directly to the meter requires effort, technology, knowledge and infrastructure that often only national standardization or metrology laboratories like the PTB (Germany) or NIST (USA) can afford [Bienias 98]. Therefore, most of the scanning microscopes operated have to be calibrated by physical transfer standards. The fabrication of such highly accurate dimensional standards for that scale is a challenge, and the calibration procedure itself has to be considered carefully [Dziomba 05].

Physical transfer standards

Whereas for CLSM, no specific dimensional transfer standards are available, SEM magnification is usually calibrated by reference gratings, and resolution is determined by critical dimension (CD) test structures made of very small particles [Joy 00]. For



(a) Calibration grating for SEM with 2160 lines/mm (Sira, Chislehurst, UK)



(b) TGZ03 step height calibration structure (500 nm) for SPM (MikroMash, Tallinn, Estonia)

Figure 1.2: Examples of pitch featured reference structures for scanning microscopes

the SPM, up to now a variety of new dimensional standards has been developed [PTB 04, Koenders 04, Nanosensors 05], among them gratings that can also be used for the calibration of other scanning microscopes. The characteristic common to all standards for scanning microscopy at the micro- and nano-range is that they are made of 1D or 2D pitch features, that is, repetitive structures either in the lateral direction, such as gratings (fig. 1.2a), or in the vertical direction, such as repetitive step heights (fig. 1.2b).

Aim of this work

Within this thesis, a landmark-based geometrical calibration strategy for scanning microscopy is introduced using 3D reference structures in contrast to the existing 1D and 2D pitch-feature based calibration procedures (fig. 1.2). The fabrication of 3D micro-reference structures is accomplished by focused ion beam (FIB) induced metal deposition. On the 3D reference structures, so-called nanomarkers are applied that

serve as landmarks (control points) with distinct 3D coordinates. Unlike pitch feature calibration methods, this approach not only allows the calibration of scanning microscopes in one step (one-step 3D calibration), without decoupling the lateral from the height calibration, but also provides the opportunity to perform coordinate measurements that are almost independent of the peculiarities of the given 3D scanning techniques and thus, enabling a correlative analysis of the individual coordinate measurements (fig. 1.1).

Content

Chapter 2 provides an overview of the scanning process and a basic introduction to 3D scanning microscopy, in particular the scanning probe microscope (SPM), the scanning electron microscope (SEM) in combination with photogrammetry, and the confocal laser scanning microscope (CLSM). Chapter 3 deals with measurement accuracy and calibration in the micro- and nano-range, and explains the alternative calibration strategy based on landmarks that is presented in this work. Chapter 4 introduces the focused ion beam instrument (FIB) and its applications. Several types of landmarks, here referred to as nanomarkers are introduced and analyzed. Also, the fabrication of spatial reference structures for the landmark-based strategy is shown in detail, as well as the geometrical characterization of the fabricated reference structures with SPM measurements. Chapter 5 demonstrates the determination of the nanomarker positions with image processing methods. An in-depth description of the image processing methods applied and the results obtained is given. In chapter 6, the results of the landmark-based calibration strategy are presented. First, the calibration of a SEM at a broad range of magnification is accomplished. Second, the calibration of three types of SEM is shown, as well as a comparison of pitch-featured calibration of a SPM versus the one-step 3D calibration by landmarks. By the use of specially shaped nanomarkers, a CLSM is also one-step calibrated. Finally, the necessity of using correlative measurements is demonstrated by comparing the measured nanomarker coordinates of all three 3D measurement methods and conducting a subsequent error analysis and error correction. Chapter 7 discusses the results and gives an outlook of further development and future applications of the landmark-based calibration method.

3D SCANNING MICROSCOPY

Before the invention of scanning microscopes, scanning had to be invented. In 1843, the Scottish clockmaker A. Bain was granted the British patent no. 9475 “*Electric time pieces and telegraphs.*” He described the principle of dissecting an image by scanning, and his patent implemented the idea into the first fax machine [McMullan 90]. A printed proposal of applying scanning to microscopy was made for the first time by E. H. Singe in the year 1928 [McMullan 95], in order to overcome the Abbe¹ limit on resolution [2.1]. The Abbe limit d_{min} is defined as the exact spacing in the specimen that can be resolved when the numerical aperture of the objective lens N_A is large enough to capture the first order diffraction pattern produced in a diffraction-limited microscope at a specific wavelength λ :

$$d_{min} = \frac{\lambda}{2 \cdot N_A} \quad (2.1)$$

Singe must have been a visionary, because only a few years later he also proposed the use of piezoelectric actuators (piezos) for the scanning movement [McMullan 95]. Today, piezos are essential for many applications in micro- and nanotechnology, and they generate the scanning movement of various micro-range measurement systems [Bhushan 04]. For example, they are to be found in every scanning probe microscope, as well as in confocal laser scanning microscopes, just to name two.

2.1 PRINCIPLES OF SCANNING MICROSCOPY

The term “scanning microscopy” is used for micro-range measurement systems that consist of several components: the probe, the scan generator, the specimen and the detector. The probe can be a fine tip, as in atomic force microscopes (AFM); a charged particle beam, as in electron microscopes (SEM) or focused ion beam (FIB) devices; or a laser beam, as in confocal laser scanning microscopes (CLSM).

Scanning microscopes collect information about a region of interest (ROI) in a serial manner (fig. 2.1). This is achieved either by a line-by-line movement of the probe across the area A that is making up the ROI, or by a line-by-line movement of the specimen stage by the area A with respect to the stationary probe. Due to the peculiarities of this scanning movement, two scan directions can be discerned: a fast scan direction (L) and a slow scan direction (H). The fast scan direction is defined by a discrete or continuous movement along one axis of the ROI. The slow scan direction is made up of the sequential single lines added along the axis perpendicular to the fast scan direction.

¹Abbe, Ernst (1840-1905)

2.1.1 Scanning parameters

Assuming use of digital scanning systems, a set of parameters can be defined for describing the scanning process (table 2.1). Usually, the operator has control of

Table 2.1: Parameters of the digital scanning process

A	Area of the ROI = $L \cdot H$
N_s	number of scan steps
d_s	step size
d_e	probe (beam) diameter
d_o	probe (beam) overlap
t_d	dwel time
t_l	loop time
t_r	refresh time [4.1]
k	scanning position

the scan speed and, hence, the loop time t_l , by choosing the dwell time t_d , and additionally the overlap d_o and the probe diameter d_e as in FIB instruments. The step size d_s is related to the probe diameter and the overlap [2.2].

$$d_s = d_e \cdot (1 - d_o). \quad (2.2)$$

In digital scan systems, d_s describes the discrete distance the probe is moved from one scan point to the next (fig. 2.1a). In analogue systems, the step size would be the distance within which a resulting signal is integrated. The step size leads to the total number of scan steps, N_s , which is the number of discrete steps chosen for the digital scan, and which usually corresponds to the number of discrete pixels in a resulting image of the ROI [2.3]

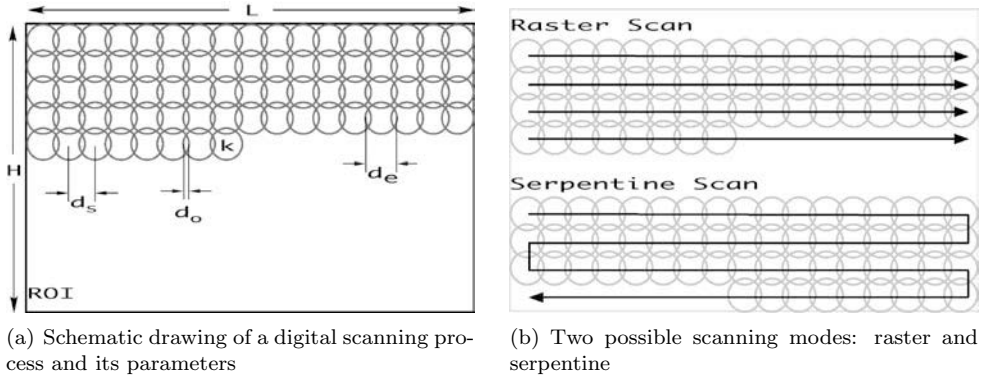
$$N_s = \frac{A}{d_s^2}. \quad (2.3)$$

Therefore, if only considering the dwell time t_d as the time consuming parameter of the scan procedure, the total loop time t_l of a scan can be written as [2.4]

$$t_l = t_d \cdot N_s = \frac{t_d \cdot W \cdot L}{(d_e \cdot (1 - d_o))^2}. \quad (2.4)$$

2.1.2 The scanning movement

Two scanning movements are conventionally used: raster and serpentine (fig. 2.1b). The raster movement starts the data acquisition of every line from only one side of the ROI, whereas the serpentine movement alternates the starting point and the scan direction. Because of hysteresis effects in most scanning systems, the raster movement is usually chosen for data acquisition [Gibson 97]. However, AFM data acquisition in both directions, reverse and forward, is sometimes applied for signal averaging and lateral force measurements [Bhushan 04]. In FIB applications, the serpentine scanning movement is necessary for accurate nanofabrication [Ritter 05].



(a) Schematic drawing of a digital scanning process and its parameters

(b) Two possible scanning modes: raster and serpentine

Figure 2.1: The principle of scanning

2.1.3 Magnification and scale

Microscopes are primarily used to make small objects visible to the human eye by magnifying them. Unlike the magnification of optical systems, M_{opt} , that is calculated from the magnification of the lens m_{lens} and the ocular $m_{eyepiece}$

$$M_{opt} = m_{lens} \cdot m_{eyepiece}, \quad (2.5)$$

the magnification of scanning microscopes, M_{scan} , is defined as the width of a line B in the output system divided by the width of the scanned line b on the specimen

$$M_{scan} = \frac{B}{b}. \quad (2.6)$$

Normally, scanned data are digitized, e.g., as an image. Then, magnification and resolution can be set in relation to the image coordinate system:

$$M_{scan} = c \cdot \frac{k_{con}}{r_{dpi}}, \quad (2.7)$$

where c is the scale [$Pixel/\mu m$], r_{dpi} is the resolution [dpi], and k_{con} is the conversion factor [$\mu m/inch$]. Eventually, the scale factor for the slow scan direction and the scale factor for the fast scan direction are not identical and have to be determined separately by applying [2.6] for the two scan directions.

As M_{scan} can only be specified for nearly planar specimen, usually the horizontal field width (HFW), which equals L (table 2.1) is used for the quantification of the data. Additionally, the HFW doesn't depend on resolution, which is another advantage.

2.1.4 Digital signal processing

In modern scanning microscopes, the signal measured by the detector is digitized at some point of the signal processing chain, usually by some kind of analogue-digital

converter. First, a discrete data matrix of the ROI is sampled, either by already discrete scanning steps, or by converting a continuously scanned signal into discrete steps. The digitized ROI consists of a finite number of picture elements (pixels), in which each pixel corresponds to an area determined by the area of the ROI, divided by the number of pixel elements. The signal data for each pixel are then quantized to a finite range h , where $h = 2^n$ Bits and $8 \leq n \leq 32$. The result can be a digital image, or the measurement data in form of a matrix $h(w_k)$.

The probe, specimen and detector interact in the process of data acquisition. Because of the raster movement, any scanned ROI consists of signal information that is gathered within a time span (“time piece”), t_d , the dwell time. If discrete raster steps are performed by the scanning device, the signal is sampled within t_d at a discrete location. In case of a continuous raster movement, in most devices an integrated signal of the distance the probe moves within t_d is sampled.

In SEM, for example, the dwell time is the only method to improve the signal-to-noise ratio (SNR), when recording an image with a defined probe. In order to characterize the interaction of the probe, the specimen and the detector, the method of convolution is used. Convolution is a mathematical way of combining two signals to form a third signal and can be modeled in time or spatial domain [Smith 97]. Because of the distinctive features of a scanning system, scanning microscopy is in both, the spatial and time domains, as described by [Yan 02]:

$$h(w(t)) = \int_0^{+\infty} f(u(t))g[w(t) - u(t)]\left(\frac{du}{dt}\right)dt \quad (2.8)$$

In this model, the scanning system consist of three coordinate systems: the real world coordinate system \mathbf{X} , the specimen coordinate system \mathbf{u} and the probe coordinates \mathbf{v} . Usually, the detected signal $h(w)$ is synchronized either with the specimen coordinates, if the specimen is moved in the scanning process, or with the probe coordinates, if it is the probe that rasters over the specimen and the overlap of the projection between the probe $g(v)$ and the specimen profile $f(u)$ is recorded at instantaneous time t . In the first case, w is linked with u and in the second case, w is linked with v (fig. 2.2). True convolution-based acquisition mode can be assumed, if the specimen response is an interaction-volume-based function and the detector is coordinate sensitive. However, for most scanning imaging systems where specimen profile and event-sensitive detectors are used, the data acquisition process is in correlation-based mode [Yan 02]. In SEM, the observed signal $h(w)$ corresponds to the number of electrons collected by the detector within t_d . For the AFM, $h(w)$ is correlated to the net force resulting from interactions between tip and sample. In CLSM, the output signal $h(w)$ is composed by the number of incoming photons within t_d , either emitted or reflected from the specimen (table 2.2).

A lot of research is being undertaken to study and to fully understand the impulse response of the various probes applied in scanning microscopy [Frase 04, Ke 01, Reimer 87b, Villarrubia 96, Wendt 02, Wilson 89]. However, the analysis of the response function will not be emphasized here. The focus will be pointed to the generation of 3D data from the scanning process and its geometrical distortions: of

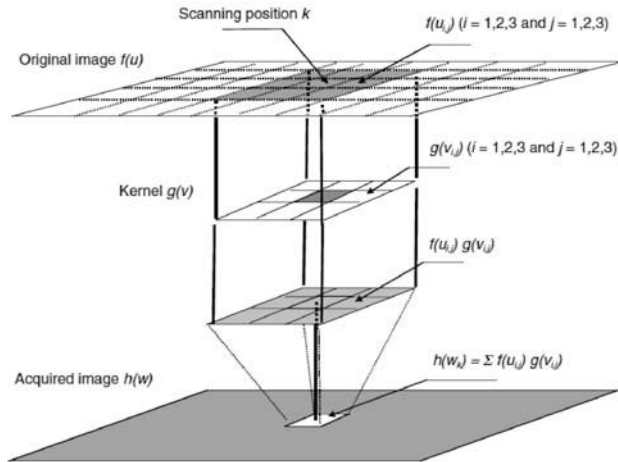


Figure 2.2: Digital image processing in the spatial domain [Yan 02]

Table 2.2: Output signals in scanning microscopy

	AFM	SEM	CLSM
input signal $f(u)$	applied force	primary electrons	laser photons
impulse response $g(v)$	specimen probe interaction	specimen probe interaction	specimen probe interaction
output signal $h(w)$	\int net force	\int secondary electrons	\int reflected photons

the 3 scanning microscopes described in table 2.2, only the output signal $h(w)$ of the SPM and the CLSM can be directly linked to spatial coordinates due to a 3D scanning movement, for example, if using a scan stage with integrated laserinterferometers [Büchner 99]. The output signal of the SEM remains within the 2D coordinate system of the scanned area of the electron beam. Therefore, no direct 3D presentation of SEM data is possible. However, by applying photogrammetric processing to the SEM data, the imaged specimen topography can be reconstructed. A basic introduction to the SPM, the SEM and the CLSM is given in the following sections.

2.2 SCANNING PROBE MICROSCOPY (SPM)

The term scanning probe microscopy refers to the family of local surface-sensitive techniques (fig. 2.3), a technology that began with the invention of the scanning tunneling microscope (STM) by [Binnig 82], and soon led to the presentation of the most popular member of the family, the atomic force microscope (AFM) [Binnig 86]. Commercial production of SPM started in 1987 with the first STM, and with the first AFM in 1989 [Bhushan 04]. A common characteristic of all SPM devices is a tip probe that interacts with the specimen surface and exploits a short-range physical interaction. The most important branches of the SPM family are the scanning force

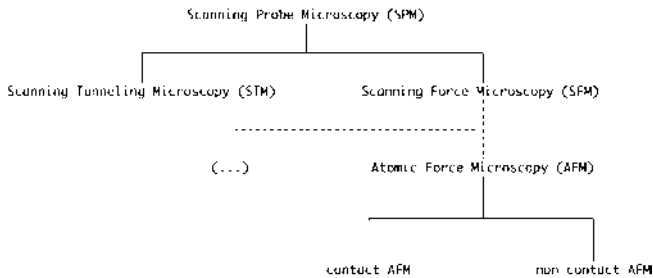


Figure 2.3: The scanning probe microscopy family [Gibson 97]

microscopes (SFM) and the scanning tunneling microscopes (STM). Scanning force microscopes (SFM), such as AFM, are defined by a flexible cantilever carrying the tip. Appropriate levers allow the measurement of small atomic forces (less than 1 nN) present in the AFM between the tip and the sample surface [Binnig 86]. The small forces cause deflection of the cantilever beam, which can be registered with the help of a laser beam or fiber interferometers. This information is generally used for creating a topography model of the surface. The AFM group includes measurement devices for repulsive forces (contact AFM), attractive forces (non-contact or ncAFM) and lateral (friction) forces (FFM or LFM). Other members of the SFM branch also include devices to detect electrostatic force (EFM), magnetic force (MFM) and electrical conductance (ECM). As the focus of this thesis is within the range of atomic force microscopical applications, the list is by far not complete and a more detailed introduction to scanning probe microscopy is given in [Bhushan 04], chapters 11 and 13.

2.2.1 Foundations of atomic force microscopy (AFM)

AFM produce 2.5 D data of sample surfaces. Small forces or changes in force between tip and sample cause motion and deflection of the flexible, very light cantilever while it is scanned over the surface. This motion information is recorded by a sensor, brought into a feedback loop and interpreted as topographic information.

Therefore, any typical AFM system (fig. 2.4) consists of a cantilever with the probe tip; a piezo-actuator driven scanner unit that moves the probe or the stage laterally and vertically; a sensor unit containing a motion sensitive photodetector for the measurement of the cantilever deflection by a laser beam; and a feedback loop system that enables the scanner to maintain the parameters needed for the desired measurement mode, e.g., contact or non-contact mode.

In principle, the cantilever deflection follows Hooke's law of the displacement d of a spring from equilibrium

$$F = -k \cdot d, \quad (2.9)$$

where k is the spring constant and F is the force applied. The spring constant k is a measure of the stiffness of the cantilever and approximated by

$$k = \frac{Y \cdot b \cdot h^3}{4 \cdot l^4}, \quad (2.10)$$

where Y is Young's modulus, b is the width, h the height and l the length of the cantilever. Young's modulus describes the ratio of stress to strain and is a material parameter varying from $\simeq 10^{10}$ to 10^{12} Pa, with the largest value for diamond, and with $0.107 \cdot 10^{-12}$ for silicon.

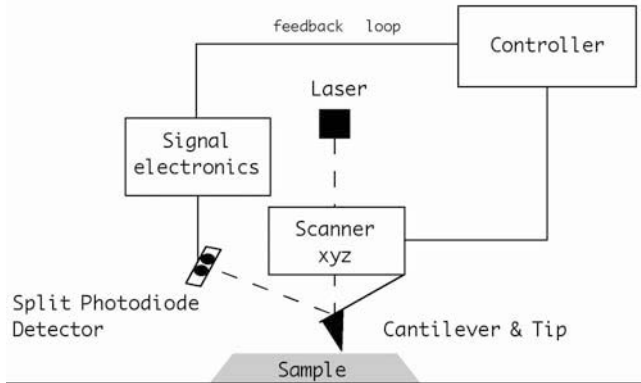


Figure 2.4: Schematic drawing of an SPM instrument

AFM scanning unit

Positioning of the probe in SPM is usually made possible by the use of piezoelectric ceramics. These materials feature a crystal structure that changes if the electric potential applied also changes. They alter their volume, but, most important, they expand or contract in a near linear fashion, although with large hysteresis. Various configurations of such ceramics are being fabricated. All of them are characterized by specific expansion coefficients and can therefore be used for numerous applications. Two types of piezoelectric (“piezos”) scanners are commonly mentioned in SPM: tube scanners and tripod scanners. Tube scanners are cylinders with one continuous inner electrode and four outside electrodes divided into quadrants. Applying a voltage to an appropriate quadrant causes lateral movement, or, if all quadrants are used, vertical movement. By applying opposite voltage to opposing quadrants, the cylinder bends. Tube scanners are only used for scanning of small ROI. Tripod scanners consist of three independent piezos, mounted orthogonally in order to allow lateral and vertical movement. The probe is mounted at the top of the z-piezo and rastered relative to the sample. Because all piezos of the tripod scanner system are discrete units, this configuration creates fewer distortions if applied to the scanning of large areas, but does show coupling effects between the single axes [Bhushan 04].

Therefore, modern SPM use a combination of a piezo scantable for lateral positioning, even for large areas, and a piezo tube for the z-motion [Tyrell 04]. Eventually,

capacitive sensors and strain gauges are used for position monitoring [Dziomba 05]. An even more accurate position monitoring is achieved by metrological SPM (met-SPM) [Bienias 98] that allow direct traceability to the meter *via* the laser-wavelength of integrated laser-interferometers [Büchner 99]. A classification of SPM according

Table 2.3: Metrological SPM classification [Dziomba 05]

Category	Description	Calibration
A	metSPM with integrated laser interferometers	directly traceable
B	SPM with integrated sensors for position monitoring B1-“Closed-loop” with active position control (feedback circuit) B2-“Open-loop” with passive monitoring	high-quality standards with uncertainty $u_d = 10^{-5}$
C	Conventional SPM with positioning by scanner settings	regular standards ($u_d = 10^{-3}$)

to accuracy and traceability aspects is currently under way [Dziomba 05]. Until now, classification of SPM into metrological categories according to their properties has resulted in a preliminary list as in table 2.3.

AFM probe

Figure 2.5 shows a SEM image of an AFM cantilever. Most commonly, cantilevers are made of silicon. The cantilever is either designed in a triangular “V” shape, or in an “I” shape, which is a simple rectangular beam protruding from the body. One

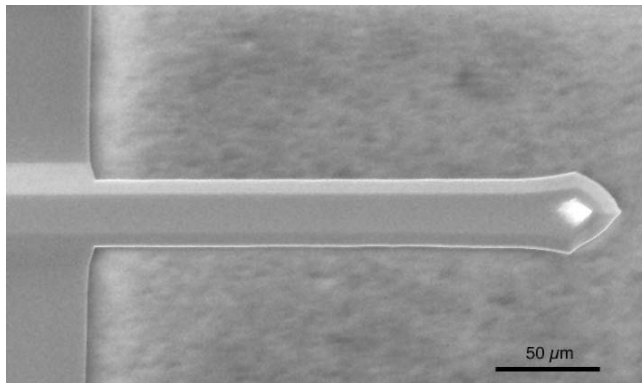


Figure 2.5: SEM image of a typical AFM cantilever

crucial parameter of the AFM probe is the resonant frequency ω_0 of the cantilever, which is determined by Young’s modulus Y [2.10], the material density ρ and the probe geometry [2.11]:

$$\omega_0 = \frac{1.029 \cdot h}{l^2} \sqrt{\frac{Y}{\rho}} = \sqrt{\frac{k}{m}}, \quad (2.11)$$

in which l is the length of the cantilever beam, h is its height, and its mass is m . Higher values for the resonant frequency - at least larger than 10 kHz - are desired in order to minimize the most disturbing external vibration and electrical noise occurring at 1 Hz to 50 Hz or to prevent excitation due to the probe trace-retrace move. The desired combination of a low spring constant k [2.9] and a high resonant frequency [2.11] for contact imaging can be achieved by reducing the mass of the cantilever. The other crucial parameter is the probe tip. Ideally, the tip should be of a sharp delta-shape and consist of a stiff, durable and nonreactive material. The tip geometry is especially important, as it can affect data obtained by AFM, and artifacts can be caused due to tip convolution of the surface [Grütter 92]. Two tip characteristics play an important role in the formation of false data: the radius of the tip and the aspect ratio of tip length to tip width forming the apex angle. A large tip curvature decreases the capability of imaging small structures. Tips with a radius of 10 nm are commercially available. The apex angle of tips used to be 30° , making it difficult to image slopes steeper than that. Modern tips with high aspect ratio are available with an apex angle of 10° .

AFM sensor unit

The deflection of the cantilever is used as a zero detector and, therefore, carries the topographical information. Several strategies have been developed to read out this information [Meyer 92]. Amongst them, the detection of an electron tunneling current (similar to the STM application by [Binnig 82]), capacitance detection, optical interferometry and laser beam deflection have all been used to measure the cantilever deflection, the last being the most common method in commercial systems [Bhushan 04].

2.2.2 Measurement modes of AFM

Interactions between sample and AFM probe tip are characterized by repulsive short range and attractive long range forces, with a zero interaction force at a fraction of a nanometer (fig. 2.6). The long range forces are weak attractive van der Waals forces that are present until the separation distance becomes so small that the electron clouds begin to repel each other electrostatically. From that distance and closer, short range forces between the sample and tip atoms start to repulse each other. Both types of forces can be used for topographical measurements: short range forces for contact mode, and long range forces for non-contact AFM mode.

Contact mode

The repulsion of short range forces is used for the contact mode, mainly for topographical measurements. Forces of 10^{-6} N to 10^{-8} N can be detected by the deflection of the cantilever. For the contact mode, the tip is brought to the sample surface and adjusted at a force or deflection F_0 . The most common method is then to keep F_0 constant by the help of a feedback loop during the measurement, hence the expression *constant force*. The measured value of deflection is recorded by the

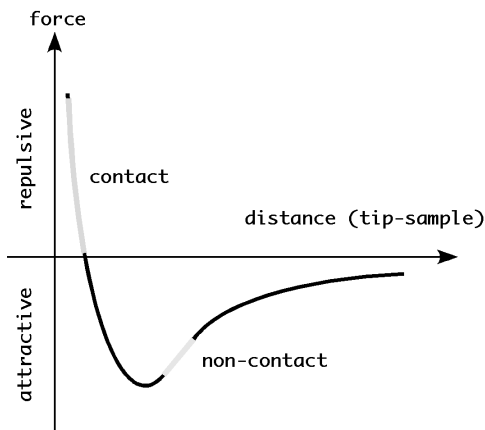


Figure 2.6: Force variation at distance in the SPM between probe and sample [Jalili 04]

sensor and compared to F_0 . The resulting error signal is used to actuate the z-piezo by an appropriate voltage in order to reestablish F_0 . Because the speed of a feedback loop is always limited, the measurement speed is limited with the *constant force* method. Another, faster method is the *constant height* method, in which no z-piezo alignment occurs during the scan. Only the measurement of the cantilever deflection is recorded for the topographic mapping. A major drawback of the *constant height* method is the fact that no steep and high steps may be present in the sample. At such steps, the danger of breaking the tip is obvious.

Non-contact mode

In non-contact mode, the cantilever oscillates at 5 - 15 nm above the sample surface, mainly in the range of attractive van der Waals forces. These are small forces in the range of 10 - 12 pN, hence much smaller than in contact mode, and can be detected by a shift in amplitude, phase or frequency of the oscillating cantilever. The change is recorded, fed into the feedback loop, and corrected by vertical movement of the probe. For the non-contact mode, a relatively stiff cantilever with a high resonant frequency is needed in order to prevent “jump-to-contact” when bringing the cantilever to the appropriate distance from the sample.

2.3 SCANNING ELECTRON MICROSCOPY (SEM)

In 1929, Stintzing proposed a scanned electron beam instrument for the analysis of small particles that could not be resolved by light microscopy in a variety of patents [McMullan 95]. Shortly after his patent application, Ruska and coworkers, who expressed the same idea in 1932, engineered the first transmission electron microscope (TEM). The term ‘electron microscope’ itself was published for the first time in scientific papers by Brüche in 1931 and by Ruska and Knoll in 1932. The first scanning

microscope, a transmission scanning microscope (STEM), was developed by von Ardenne, who in 1933 imaged the surface of Cu_2O . In 1935 Knoll, co-inventor of the TEM, published images from solid samples, using a scanning electron beam for direct surface imaging. These are considered to be the first scanning electron microscope (SEM) images [Pfefferkorn 84, McMullan 95].

2.3.1 Foundations of SEM

The principle components of an SEM are an electron gun which will generate the electron beam; an electron-optical column whose purpose is to produce a small electron probe at the specimen surface; a vacuum system, in order to allow a maximum mean free length of path for the electrons; and a detector system for image formation or analytical modes (fig. 2.7). The electron gun consists of a filament (cathode) and

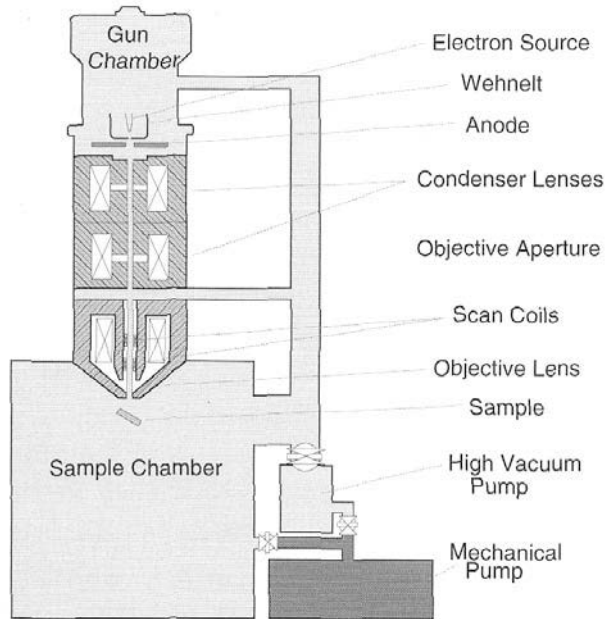


Figure 2.7: Schematic drawing of a scanning electron microscope (SEM) [PEO 96]

an anode. The the electron gun both generates electrons at the filament tip and accelerates the emitted electrons by applying a voltage difference of 0.1 kV to 30 kV between anode and cathode. The anode accelerates the emitted electrons to an energy

$$E = e \cdot U, \quad (2.12)$$

and to a non-relativistic de Broglie wavelength

$$\lambda = \frac{h}{\sqrt{2 \cdot m_e \cdot U_e \cdot e}}, \quad (2.13)$$

in which h is the Planck constant, m_e the mass of an electron, e the elementary charge of an electron², and U is the acceleration voltage applied. Electron volts [eV] are used as units, in order to visualize the dependency on the acceleration voltage U . The electrons generated and accelerated by the voltage difference in the electron gun are then demagnified by a condenser system and brought to a scanning movement by deflection coils within the electron-optical column. The final lens focuses the beam onto the specimen surface with a probe diameter of 1-10 nm and a total electron-probe current I_p of 10^{-9} to 10^{-12} A [Reimer 98]. A minimum vacuum of $1 \cdot 10^{-4}$ to

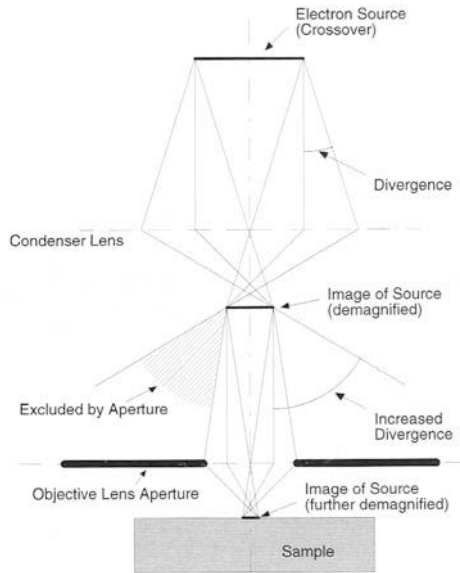


Figure 2.8: Ray geometry in the SEM electron-optical column (redrawn after [PEO 96])

$1 \cdot 10^{-6}$ Pa is needed for SEM operation, depending on the type of gun used: field-emission guns (FEG) require the ultra-high vacuum, whereas thermoionic cathodes (e.g., LaB₆) need only high-vacuum conditions.

2.3.2 SEM signal formation

The SEM signal is generated at the specimen surface. Thus, electrons of the probe, also named primary beam electrons (PE), interact with the atoms of the surface. Due to elastic and inelastic scattering processes, electrons of a broad energy spectrum are emitted from the sample surface (fig. 2.9). The gradual diminution of the electron energy by the scattering events forms an interaction volume with a finite depth R of the electrons. The size of R varies from a few nanometers up to several micrometers, as it depends on the material density and electron energy [Kanaya 72]. The types of signal generated by electron-specimen interactions consist of backscattered electrons (BSE), secondary electrons (SE), Auger electrons (AE), X-rays and even light. Some

² $h = 6.6256 \cdot 10^{-34} \text{ Js}, m_e = 9.109 \cdot 10^{-31} \text{ kg}, e = 1.602 \cdot 10^{-19} \text{ C}$

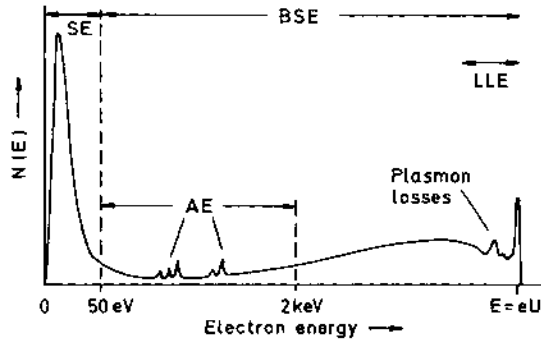


Figure 2.9: Energy spectrum of secondary electrons (SE) and backscatter electrons (BSE) [Reimer 98]

of the interaction energy is transferred to heat. Emitted electrons with energies lower than 50 eV are classified as SE, whereas electrons with a higher energy are defined as BSE (fig. 2.9). Both SE and BSE are used in the SEM for imaging purposes.

SE imaging

SE are generated by inelastic collisions [Reimer 98]. Due to their low energy, SE can be easily collected by a detector that has a positively biased grid in front of it. The most commonly used type of detector is the Everhart-Thornley [Everhart 60] type. As the secondary electrons hit the scintillator of the Everhart-Thornley detector, the electrical energy is converted into photons. The photons are forwarded via a light pipe to a photomultiplier tube. In the photomultiplier tube, the photons are converted back to electrical energy, undergoing cascading events across a series of dynodes to enrich the signal. The signal is further refined in the preamplifier and amplifier before being digitized or projected onto the screen of the viewing cathode ray tube.

Topographic contrast mechanisms

The basic contrast formed in SEM is topographic contrast, as the SE yield η_{SE} depends on the local tilt of the specimen surface [Reimer 98]: the larger the angle between incident beam and surface normal, the larger the number of secondary electrons that are within escape depth R (fig. 2.10a, b). In addition to the pure surface tilt contrast, there are also other topographic contrast mechanisms on bulk specimen [Reimer 98], such as edge contrast (fig. 2.10c).

2.3.3 Fundamental terms in electron optics

Although the electron beam acts like a light source and the magnetic lenses like glass lenses in conventional microscopy, there are fundamental differences between light

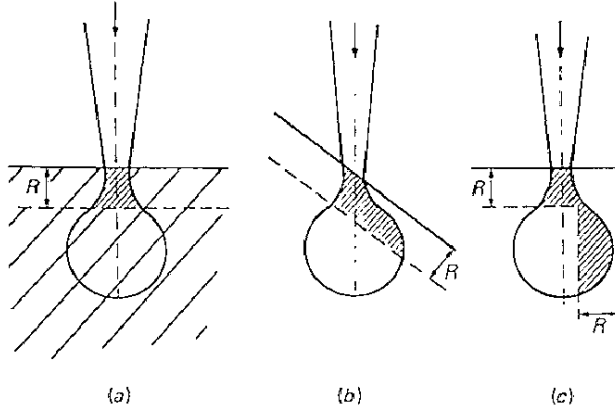


Figure 2.10: SE pure surface tilt and edge topographic contrast [Watt 85]

microscopy and electron microscopy. The most obvious differences are the signal formation and contrast mechanisms mentioned above in SEM that do not have analogies in light optics.

SEM probe formation

A SEM system cannot resolve features smaller than the geometric probe size d_0 , a term also called “spot size”

$$d_0 = C_0 \alpha_p^{-1} \quad (2.14)$$

that is inversely proportional to the probe aperture α_p [Reimer 98]. But SEM lenses exhibit certain kinds of aberrations: spherical aberration, chromatic aberration, axial astigmatism and diffraction error, whereas the axial astigmatism can be compensated. Spherical aberration is expressed by the spherical aberration coefficient C_s . It occurs because electrons farther away from the optical axis z are focused closer to the magnetic lens. The diameter d_s of the plane of least confusion is:

$$d_s = 0.5 C_s \alpha^3. \quad (2.15)$$

Chromatic aberration occurs due to the energy spread ΔE of accelerated electrons [2.12] and is expressed by the chromatic aberration coefficient C_c . Therefore, not all the electrons move at equal speed and paths of slower electrons are bent more strongly than the paths of faster electrons at the magnetic lens. The resulting disc of least confusion has a diameter d_c :

$$d_c = C_c \frac{\Delta E}{E} \alpha. \quad (2.16)$$

SEM objective lenses contain a aperture limiting diaphragm in order to keep spherical and chromatic aberrations small (fig. 2.8). The diaphragm causes an Airy disc at the focal plane with half-width-full-maximum diameter d_d :

$$d_d = 0.61 \frac{\lambda}{\alpha}, \quad (2.17)$$

in which λ is the de Broglie wavelength of the electrons and α is the aperture of the objective lens. The resulting effective probe diameter, d_e , is bigger than d_0 , as the aberrations mentioned above [2.15, 2.16, 2.17] have to be taken into account. The effective probe diameter can then be written

$$d_e = \sqrt{d_0^2 + d_d^2 + d_s^2 + d_c^2}, \quad (2.18)$$

as summarized in [Stegmann 99].

Resolution

It is obvious that the resolution of a SEM cannot be better than the effective probe diameter d_e [2.18]. However, no simple definition of resolution can be given for SEM imaging modes. The effective resolution d_e is further impaired by the delocalization of SE generation due to the interaction volume of the incident electron probe with the specimen (fig. 2.9) [Seiler 76] and the signal-to-noise ratio (SNR) [Wells 74]. Moreover, resolution also depends on contrast forming mechanisms that are themselves related to the specimen structure. It is generally accepted that resolution of the SEM in SE mode is limited to the order of 1-2 nm, but not necessarily identical with the electron probe size. Therefore, an image based definition should be applied for

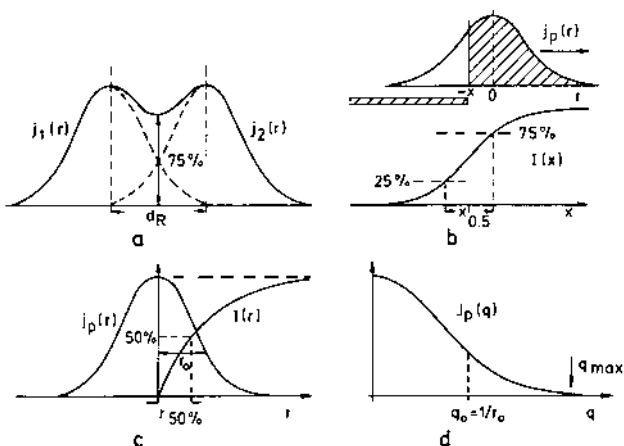


Figure 2.11: Definitions of resolution: a) Rayleigh criterion, b) edge resolution, c) FWHM d) maximum spatial frequency [Reimer 98]

the definition of resolution [Vladar 98]. In order to be able to extract the maximum resolution parameters from an image, two conditions must be fulfilled: the image must be free of astigmatism and it must be in focus. There are methods published to verify the conditions [Postek 98, Vladar 98]. The most common resolution criteria are the full-width half maximum (FWHM) (fig. 2.11c) and the Rayleigh criterion (fig. 2.11a). Both types define a minimum distance d_{min} between two fringes that are said to be resolved. The FWHM criterion is a single event criterion that defines d_{min} as the spread of a Gaussian curve at half the maximum intensity. The Rayleigh

criterion states that two points are resolvable if the maximum intensity of one image is superimposed on the first minimum of the other. This occurs when the combined irradiance of both fringes at the center of the resultant broad fringe is $\frac{1}{8}\pi^2$ times the maximum irradiance. However, the Rayleigh criterion has limited practical value in SEM, because test samples with point-like structures smaller than the electron probe diameter d_e are needed. The edge resolution (fig. 2.11b) is a more practical approach, but requires structures across and along the scanning directions of the SEM. Then, the edge resolution $x_{0.5}$ can be defined as the distance between two values x_{lower} and x_{upper} of the profile. Common values for x_{lower} are 25% and for x_{upper} 75%.

Another way of determining resolution is the use of spatial frequency analysis [Erasmus 80, Vladar 98]. With this method (fig. 2.11d), a diffractogram of the power spectrum of the image is obtained by two-dimensional Fourier transformation. There, the signal intensity is displayed for each frequency. The intensity normally decreases with increasing frequency until it reaches an arbitrary boundary of random noise. The resolution limit can then be determined to be the highest frequency that still is information and not noise. However, the Fourier based analysis only works at high magnifications and the probe size is the resolution-limiting factor. Plus, the analysis is built on the assumption that the specimen carries continuous and uniform distribution of spatial frequencies. Otherwise, the smallest structures on the specimen instead of the probe would determine the resolution limit. Finally, the decision between noise and information is made by the user, and hence, depends on expertise and skills. Recently, [Joy 00] introduced a new method for the determination of resolution, especially for critical dimension metrology SEM (CD-SEM). CD-SEM, as a monitoring system - e.g., for wafer production - must achieve 1 nm resolution. [Joy 00] proposed the use of the cross-correlation analysis as an alternative, because it avoids the problem of distinguishing signal from noise.

Depth of field

What makes the SEM so valuable for micro-range measurements, 3D surface analysis and reconstruction are the topographic details of the scanned images and the large depth of field (DOF). DOF is defined as the focal region T above and beyond the focus point, in other words the minimum probe diameter, which remains in a reasonable focus δ that is smaller than the screen pixel size d divided by the magnification M_{scan} , as along the lines of [2.6]. Hence, the depth of focus is affected by the probe aperture α_p , and T becomes

$$T = \frac{\delta}{\tan \alpha_p} \simeq \frac{d}{\alpha_p \cdot M_{scan}}. \quad (2.19)$$

In contrast, the depth of focus of an optical microscope is [Reimer 98]

$$T = \delta \cdot \sqrt{\frac{\delta^2}{\lambda^2 - 1}}, \quad (2.20)$$

and therefore at least 10 times smaller than the depth of focus of a SEM.

Focal length

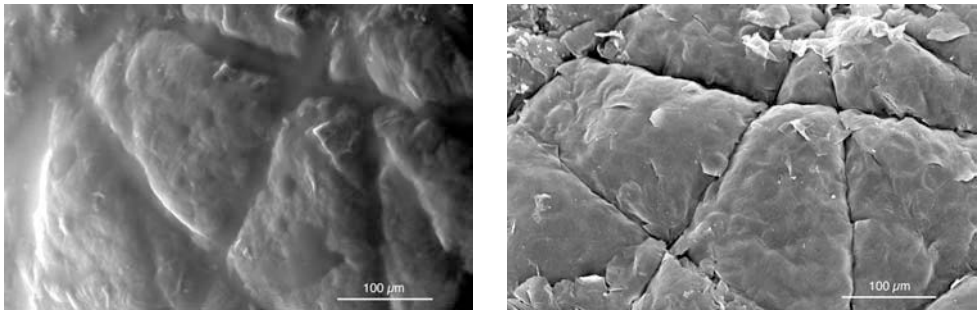
Whereas the focal length f in light optics is determined by the lens curvature, the focal length f_B of a magnetic lens is related to a bell-shaped distribution $B(z)$ of the magnetic field along the optical axis z

$$f_B = w_d + k_z \propto \frac{1}{B(z)}, \quad (2.21)$$

in which w_d denotes the working distance from the the objective lens aperture to the specimen along the optical axis (z), and k_z denotes the distance from the aperture to the virtual projection centre (Z_0). The final objective lens follows a diaphragm (fig. 2.8) of a diameter of 50 to 200 μm . Hence, apertures of 10 - 20 mrad can be produced with $f \simeq 5\text{-}20$ mm. That value corresponds to effective working distances w_d of 5-20 mm (fig. 2.21).

2.3.4 Environmental SEM

There are various inconveniences associated with the specimen preparation for SEM. In particular, the high vacuum requirements and the need for electrically conductive specimen can make SEM analysis expensive and time consuming. To overcome these limitations was the motivation for the development of a special kind of scanning electron microscopy technique that operates at high pressures. It was introduced in 1978 by Danilatos and is called environmental scanning electron microscope (ESEM) [Danilatos 78]. This technique allows imaging hydrated samples and also simplifies the preparation of specimens, because they can be observed, e.g., in a water vapour atmosphere of up to 3000 Pa [Danilatos 93b]. Two technical challenges had to be overcome in eliminating the high vacuum requirement of the specimen chamber. One was to achieve the separation of the environments of the specimen chamber and the electron column. The second was to establish a secondary electron detection system that functions in a non-vacuum surrounding. The first challenge was met by introducing a multiple pressure limiting aperture (PLA) system, the second by introducing the environmental secondary electron detector (ESD) and the gaseous secondary electron detector (GSD). The ESEM is frequently used in material research [Donald 03, Schnarr 97], dental research [Cowan 96, Manero 00] and more and more in the field of life sciences [Collins 93, Tai 01, Sanger 03]. Figure 2.12a shows an area on a human skin sample imaged in the ESEM at 6 mbar water vapor pressure in the specimen chamber and without prior chemical preparation of the skin. Figure 2.12b exemplarily shows the identical area of the same skin specimen imaged at high-vacuum conditions in the SEM, after chemical fixation, dehydration by alcohol with subsequent critical point drying and gold coating. Dramatical topographical changes can be observed due to the chemical preparation, as has been reported by others [Collins 93]. An alternative way to structurally preserve specimens for SEM investigations is the use of cryo-fixation [Hermann 97].



(a) Human skin imaged by ESEM without chemical preparation

(b) Human skin imaged by SEM after critical point drying

Figure 2.12: Identical area on human skin imaged by ESEM and SEM

The multiple pressure limiting aperture system

The vacuum needed in the electron optical column and at the electron source depends on the type of electron gun, but has to be at least 10^{-4} Pa, whereas the minimum partial pressure necessary to keep water in the liquid phase at 4 °C is 811 Pa. A multiple pressure limiting aperture (PLA) system enables the ESEM to work under such conditions by allowing a high water pressure in the specimen chamber without affecting the high vacuum at the top of the microscope column, where the electron source is located.

Two PLA pieces with diaphragms of 50-300 μm are inserted in a single holder also known as the bullet, at the end of the probe-forming lens. The bullet has lateral openings [Danilatos 93b] in order to evacuate the gas from the specimen chamber by an additional rotary pump. Thus, a pressure differential sufficient for a pressure of 811 Pa on the specimen chamber side, and sufficient to reach a vacuum of less than 10^{-4} Pa at the electron column side, can be generated.

Environmental secondary electron imaging

The relatively high pressure present in the specimen chamber causes electron-gas interactions, e.g., electron scattering. The fraction of electrons not scattered, I_0 , can be described by the exponential law

$$I_0 = e^{-\frac{kpd}{T U}} \cdot I_{total}, \quad (2.22)$$

with a specific gas constant k , the energy of the beam electrons U , the distance the electron travels through the gaseous environment (beam gas path length BGPL) d in meters, temperature T and pressure p [PEO 96]. This corresponds to a value of about 40 % of the primary beam electrons scattered at a water vapour pressure of 900 Pa, given an acceleration voltage of 20 kV and a BGPL of 0.002 m.

The fraction of the electrons scattered at the gas present in the specimen chamber form a “skirt” distribution that has a broader radius than the electrons of the primary beam that are not scattered at all. Let $r_{0,5}$ be the radius of a circle that contains

50 % of the scattered electrons. The value for $r_{0.5}$ at typical ESEM conditions ($d = 0.002$ m, $p = 1000$ Pa) is $16 \mu\text{m}$ according to equation [2.23], which has been empirically derived on the basis of experimental data [PEO 96]:

$$r_{0.5} = 0.0039 \cdot d + 1.326 \cdot d \cdot (pd)^{1.38} \quad (2.23)$$

It is obvious that $r_{0.5}$ is much larger than the probe size d_e . As a result, the skirt electrons only form a nearly constant background signal that can be subtracted or discarded. Therefore, it can be stated that resolving power is only limited by the diameter of the probe formed by the unscattered fraction of the electrons [Danilatos 93b]. Electrons of the primary beam interact with the specimen surface as shown in figure 2.9. However, the detectors used in conventional SEM do not work in the ESEM. Two special detectors have been introduced for the detection of the SE signal in ESEM mode: the ESD and the GSE [Danilatos 90] detectors. Both detectors are situated at the the end of the bullet, just at the lowest point of the pole piece. The beam passes through the detectors, and their location directly above the specimen guarantees improved efficiency in collecting the SE signal from the specimen. The detectors carry a positive potential of a few hundred volts that accelerates the SE emitted from the specimen towards the electrode. Thereby, they collide with gas molecules present in the specimen chamber, and the resulting ionization process generates further SE, called environmental SE. As these incidents multiply, a cascade effect is generated that amplifies the original signal considerably until reaching the detector. This cascade effect also implies an amplification gain in an easily ionized gas, as shown by [Fletcher 99]. It is also possible to perform BSE imaging and X-ray analysis in the ESEM mode. An ESEM publication overview has been presented by [Danilatos 93a].

2.4 PHOTOGRAMMETRIC SEM

The 3D reconstruction of real world objects with the SEM can be achieved in various ways, e.g., by photogrammetric methods [Boyde 70] using SE electrons as imaging carriers, or by shape-from-shading [Reimer 87a] using the BSE signal on four detectors. Both methods offer means for non-destructive analysis and 3D modeling, but the derivation of spatial coordinates is done indirectly through the images - in contrast to SPM and CLSM, for example.

The SEM has been an excellent candidate for photogrammetric analysis since early on [Oshima 70, Boyde 70], because it provides high resolution, a large depth of field, and images can be captured over a wide range of magnification, very much in contrast to optical microscopes. Additionally, the good signal to noise ratio makes the combination of SEM imaging and photogrammetric analysis very interesting for 3D evaluation in the fields of materials science, quality control and life science. Because SEM images are now mostly generated and stored as digital data, the photogrammetric method is also a good basis for the automation of 3D reconstruction of SEM data [Koenig 87]. However, not only has the area-based generation of topographic maps been put in the foreground of SEM 3D imaging, but also point measurements [Hemmler 95], and the calibration of the microscopes by photogrammetric means for high precision length and angle measurements [Maune 75].

2.4.1 Photogrammetry

The term photogrammetry is used to describe methods for the determination of spatial measurements of objects by means of images. Given the fact that nothing is known about the object, its 3D structure can only be derived from at least two images that are taken from different perspectives, because a single image alone lacks the depth information. However, if the same object is captured in two or more images, homologous points of the object can be determined in all images involved. Because of the different perspectives, and due to the law of projection applied when generating the images, the 3D object coordinates can then be calculated from the homologous points.

Geometry of projection

The imaged scene in a picture is described by the 2D image coordinate system \mathbf{x}' with the image points $P_i (x'_i, y'_i)$ of the picture, whereas the real world scene is called object space within the object coordinate system \mathbf{X} and the 3D object points $P_i (X_i, Y_i, Z_i)$ (fig. 2.13). In order to capture one object on several images, the sensor

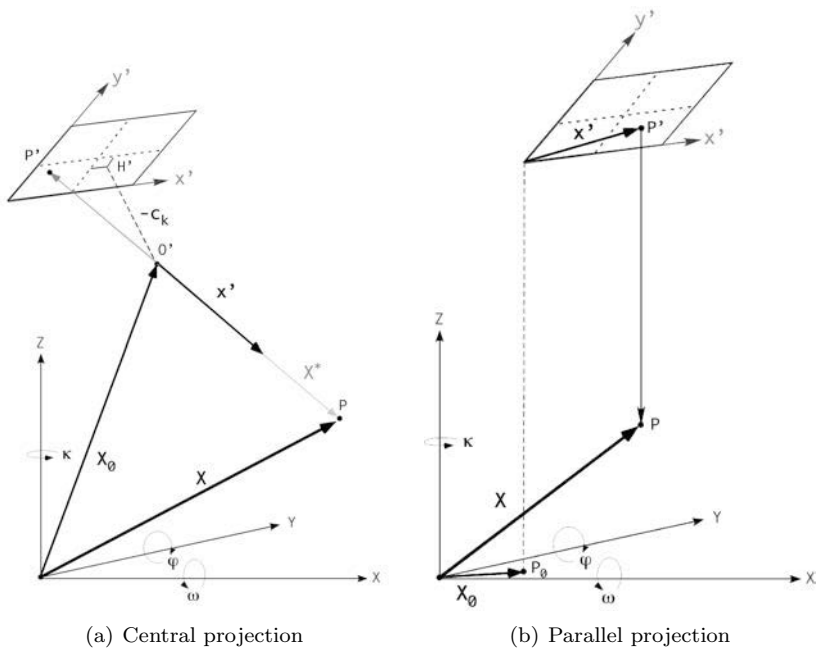


Figure 2.13: Projection geometries

(e.g. the camera) has to be moved in the real world, and with it the orientation of the image plane. The orientation of the image plane with respect to the real world is called *exterior orientation*. The projection of the scenery on the image according to the optical laws applied is called the *interior orientation*. The *exterior orientation* of the image can be described in six transformation parameters, three translations

\mathbf{X}_0 (X_0, Y_0, Z_0) and three rotations \mathbf{R} ($R_\varphi, R_\omega, R_\kappa$) as shown in figure 2.13. The elements of the rotation matrix \mathbf{R} can be summarized as in [2.24]:

$$\mathbf{R} = \begin{pmatrix} r_{11} & r_{12} & r_{13} \\ r_{21} & r_{22} & r_{23} \\ r_{31} & r_{32} & r_{33} \end{pmatrix}. \quad (2.24)$$

The relation between the image coordinates and the object coordinates can be described by the geometrical law of the projection applied (fig. 2.13). The central projection model (fig. 2.13a) is used whenever the imaging rays intersect in a projection centre O' , as when the rays in a regular camera intersect in the focal point. The model of parallel projection (fig. 2.13b) is considered if the distance to the focal point is extremely large so that an infinitely distant location of the camera to the viewplane can be assumed, or if multi-lens systems such as telecentric camera objectives are used.

For the case of central projection, the parameters of the *interior orientation* describe the site in the image coordinate system H' (x'_0, y'_0) normal to the projection centre O' and the perpendicular distance $-c_k$ from the real projection centre O' to the image plane, as well as optical distortion parameters ($\Delta x'$, $\Delta y'$), which describe the deviations from ideal optical projection by distortion.

The photogrammetric analysis is based on the description of a real world object point P with respect to the projection centre O' using the vector \mathbf{X}_0 from the origin of the real world coordinate system to the projection center O' , and the vector \mathbf{X}^* from the image point P' to the real world object point P (fig. 2.13)

$$\mathbf{X} = \mathbf{X}_0 + \mathbf{X}^*. \quad (2.25)$$

Because \mathbf{X}^* can not be directly determined, it is being replaced by the image vector \mathbf{x}' , the vector from O' to P' which has been transformed to object space until it has the same direction as \mathbf{X}^* :

$$\mathbf{X}^* = m \cdot \mathbf{R} \cdot \mathbf{x}', \quad (2.26)$$

in which the transformation \mathbf{X}^* to \mathbf{x}' is expressed by a scale factor m and the rotation matrix \mathbf{R} (fig. 2.13). Mathematically, the rotation of a vector is represented by its multiplication with a rotation matrix \mathbf{R} [2.24] with the elements r_{ij} [Regensburger 90]:

$$r_{11} = \cos \varphi \cdot \cos \kappa + \sin \varphi \cdot \sin \omega \cdot \sin \kappa \quad (2.27)$$

$$r_{12} = -\cos \varphi \cdot \sin \kappa + \sin \varphi \cdot \sin \omega \cdot \cos \kappa \quad (2.28)$$

$$r_{13} = \sin \varphi \cdot \cos \omega \quad (2.29)$$

$$r_{21} = \cos \omega \cdot \sin \kappa \quad (2.30)$$

$$r_{22} = \cos \omega \cdot \cos \kappa \quad (2.31)$$

$$r_{23} = -\sin \omega \quad (2.32)$$

$$r_{31} = -\sin \varphi \cdot \cos \kappa + \cos \varphi \cdot \sin \omega \cdot \sin \kappa \quad (2.33)$$

$$r_{32} = \sin \varphi \cdot \sin \kappa + \cos \varphi \cdot \sin \omega \cdot \cos \kappa \quad (2.34)$$

$$r_{33} = \cos \varphi \cdot \cos \omega \quad (2.35)$$

Summarizing [2.25] and [2.26], the transformation of an image point into object space and *vice versa* is described by the collinearity equations [2.36] and [2.37], which are of utmost importance in the field of photogrammetry:

$$\mathbf{X} = \mathbf{X}_0 + m \cdot \mathbf{R} \cdot \mathbf{x}', \quad (2.36)$$

for the retrieval of the object coordinates from the image coordinates, and, correspondingly, the calculation of the image coordinates from a depicted imaging setup

$$\mathbf{x}' = \frac{1}{m} \cdot \mathbf{R}^{-1} \cdot (\mathbf{X} - \mathbf{X}_0) = m' \cdot \mathbf{R}' \cdot (\mathbf{X} - \mathbf{X}_0). \quad (2.37)$$

The scale factor m is singular for every real-world point P of the object. Hence, only the direction to P can be defined within one image, and not the distance and thereby the spatial position. Determining the spatial position only becomes possible when, for example using a second image - hence the term stereophotogrammetry.

Collinearity equations for central projection

The functional correspondence of image and object coordinates expressed by the collinearity equation [2.37] in the case of central projection becomes

$$\begin{pmatrix} x' \\ y' \\ -c_k \end{pmatrix} = m' \cdot \mathbf{R}' \cdot \left[\begin{pmatrix} X \\ Y \\ Z \end{pmatrix} - \begin{pmatrix} X_0 \\ Y_0 \\ Z_0 \end{pmatrix} \right]. \quad (2.38)$$

Because of the relationship between the image constant c_k and the magnification m' [Regensburger 90]

$$m' = \frac{-c_k}{r_{31} \cdot (X - X_0) + r_{32} \cdot (Y - Y_0) + r_{33} \cdot (Z - Z_0)}, \quad (2.39)$$

the explicit collinearity equations for the case of central projection geometry are [Hemmler 01]:

$$x' = -c_k \cdot \frac{r_{11} \cdot (X - X_0) + r_{12} \cdot (Y - Y_0) + r_{13} \cdot (Z - Z_0)}{r_{31} \cdot (X - X_0) + r_{32} \cdot (Y - Y_0) + r_{33} \cdot (Z - Z_0)} \quad (2.40)$$

$$y' = -c_k \cdot \frac{r_{21} \cdot (X - X_0) + r_{22} \cdot (Y - Y_0) + r_{23} \cdot (Z - Z_0)}{r_{31} \cdot (X - X_0) + r_{32} \cdot (Y - Y_0) + r_{33} \cdot (Z - Z_0)}. \quad (2.41)$$

Collinearity equations for parallel projection

When parallel projection geometry is used as the functional model, the parameters of the collinearity equations are reduced by Z_0 , because parallel rays do not intersect in one central point. The missing projection centre has a broad effect on the geometrical model. First, it is not possible to construct a perpendicular to the image plane, known as the principal point H' . Second, there is no distinct focal length, i.e. the distance

from the principal point to the projection centre. Therefore, instead of the image constant c_k the magnification factor m' has to be used:

$$\begin{pmatrix} x' \\ y' \\ 0 \end{pmatrix} = m' \cdot \mathbf{R}' \cdot \left[\begin{pmatrix} X \\ Y \\ Z \end{pmatrix} - \begin{pmatrix} X_0 \\ Y_0 \\ 0 \end{pmatrix} \right]. \quad (2.42)$$

and, the explicit collinearity equations for the case of parallel projection geometry become:

$$x' = m' \cdot [r_{11} \cdot (X - X_0) + r_{12} \cdot (Y - Y_0) + r_{13} \cdot Z] \quad (2.43)$$

$$y' = m' \cdot [r_{21} \cdot (X - X_0) + r_{22} \cdot (Y - Y_0) + r_{23} \cdot Z]. \quad (2.44)$$

2.4.2 Photogrammetric analysis of SEM data

There are some preconditions to spatial object reconstruction on the basis of SEM images [Maune 75, Elghazali 84, Hemmleb 01]: First, because the sensor cannot be moved in the SEM, the sample has to be moved for the purpose of changing the perspective instead. Second, the imaging properties of the SEM operated at distinct conditions have to be evaluated by a calibration, in order to be able to build a quantitative 3D model on the basis of the image data obtained. Third, the applied law of projection should be changed at magnifications higher than 500x from central projection to parallel projection geometry.

SEM imaging parameters

The SEM magnetic or electrostatic lenses produce a virtual projection centre at a large focal length f [2.21] with the coordinates of Z_0 that equal the central point O' in the central projection case. However, Z_0 is completely dependent on the working distance w_d that is adjusted by the user, whereas the distance from the virtual projection centre to the aperture diaphragm k_z is constant and can be calculated according to [Hemmleb 01]. The correct determination of this principle distance has a large effect on the calculation of the height of an imaged object [Howell 78] in the case of central projection at low magnifications. At magnifications higher than 500x, [Boyde 73] has shown that the parallel projection geometries should be assumed. The parallel projection geometry implies that the central point O' disappears and photogrammetric analysis has to be performed with the magnification factor m' . However, the magnification and orientation parameters of the image planes are only approximately known in SEM images, therefore a calibration process of the system is required (see chapter 3).

Stereo SEM

As previously described, the spatial coordinates of corresponding homologous points can be only reconstructed if the orientation of the image plane in the real-world and if the applied type of projection is known. This step, which reconstitutes the 3D object coordinates of a point from its 2D image coordinates is called *forward section*.

The general model that allows random orientation of the image plane can be reduced to a simple trigonometric formula if two images are formed by only altering the orientation of one axis in order to change the perspective. This simplified *forward section* model is often used for the 3D reconstruction of objects imaged in the SEM, as the necessary change of view (stereo-view) can be achieved in almost any SEM by tilting the specimen stage. However, the accurate 3D reconstruction of SEM data requires exact knowledge of both the change of perspective by tilting and the optical properties of the imaging device. In order to capture one object in two images, for stereophotogrammetric purposes the sample stage is tilted along one axis and the specimen is imaged at both orientations. If the tilt angle is known and homologous points are available, e.g. by area-based matching [Hemmler 01], the reconstruction of the object coordinates from the SEM image data can be achieved by a simple model of the forward section, depending on the law of projection applied. If tilting around φ is assumed, the following formulas for the central projective case at low magnifications

$$X = m \cdot x' \quad (2.45)$$

$$Y = m \cdot y' \quad (2.46)$$

$$Z = (1 - m) \cdot c_k \quad (2.47)$$

$$m = \frac{1 + \frac{x''}{c_k} \cdot \tan \frac{\varphi}{2}}{1 + \frac{x' - x''}{c_k \cdot \tan \varphi} + \frac{x' \cdot x''}{c_k^2}}, \quad (2.48)$$

or for the parallel projective case at high magnifications apply [Burkhardt 81]

$$X = m \cdot x' \quad (2.49)$$

$$Y = m \cdot y' \quad (2.50)$$

$$Z = x' \cdot \tan \frac{\varphi}{2} - \frac{x' - x''}{\sin \varphi}, \quad (2.51)$$

with

- X, Y, Z - object coordinates
- x', y' - image coordinates of left image
- x'', y'' - image coordinates of right image
- m - scale
- c_k - image constant ($c_k = m \cdot Z_0$).

Either magnification or image constant has to be determined by a previous calibration. The simplified forward section was introduced to SEM early on [Boyde 70], and it does have some advantages because it provides a simple mechanism for the 3D reconstruction of SEM images. The accuracy of the method is, however, highly dependent on the accuracy and knowledge of the applied tilt angle difference, and on the surface texture for area-based matching of homologous points [Hemmler 01].

2.5 CONFOCAL LASER SCANNING MICROSCOPY (CLSM)

Confocal microscopy is a 3D light microscopy technique invented by Marvin Minsky [Minsky 61], under the name “two-times focussing raster microscope,” in order to be able to examine thick specimens of brain tissue for neurological studies, which could not be prepared as thin cross-sections. The application of confocal microscopes deeply improved the image resolution compared to conventional microscopes, but the most profound advantage of confocal microscopy is its ability to discriminate wanted information (in focus) from unwanted signal that is out-of-focus [Carlsson 91] for imaging purposes and 3D measurements.

2.5.1 *Confocal principle*

Due to the limited depth of focus of regular light microscopes, thick specimens cannot be captured in focus as a whole. Such samples can be analyzed focus-plane by focus-plane, but the amount of signal not originating from the focus plane is usually too high and impairs the formation of sharp images with a high contrast. Several tricks are necessary to circumvent the detection of rays that are out of the focus plane. All of these tricks combined characterize the confocal principle (fig. 2.14). The first trick is to not illuminate the whole image plane as it is done in conventional light microscopy - in other words, not to use a focus plane at all, but only a focus point that illuminates a distinct spatial coordinate of the specimen. The second trick is to make the reflected rays (the signal) pass through a small aperture (pinhole), allowing almost only the reflected rays from the illuminated spot itself to reach the detector, which is a photo-multiplier registering the incoming photons. Hence, only the information from a defined location of known spatial coordinates is sampled. The resulting signal

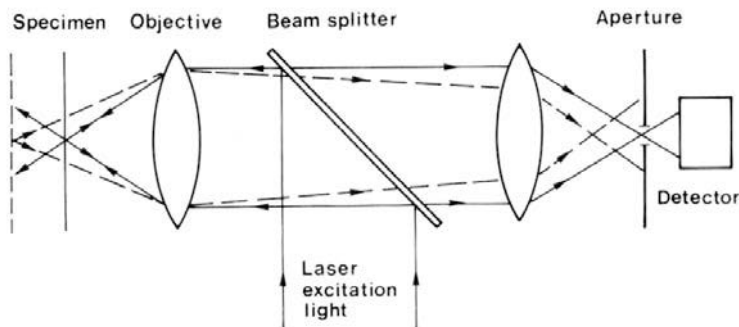


Figure 2.14: Confocal principle [Carlsson 91]

information from every object point then represents a data cube. Finally, in order to be able to analyze not only one single point of a specimen, a raster movement has to be introduced. Again, either the illumination point source is scanned over the specimen (beam scanning), or the stage is moved with respect to a fixed laser beam (stage scanning).

2.5.2 Basic terms of CLSM

CLSM instrument, such as the Leica TCS series (Leica Bensheim, Germany) shown in figure 2.15, are based on conventional microscopes, but the light source is a laser. The laser beam is focused on a sample such that only one object point is illuminated, and again, a detector pinhole discriminates against scattered light that is not emitted from the plane of focus. The TCS series is operated by beam-scanning. The lateral

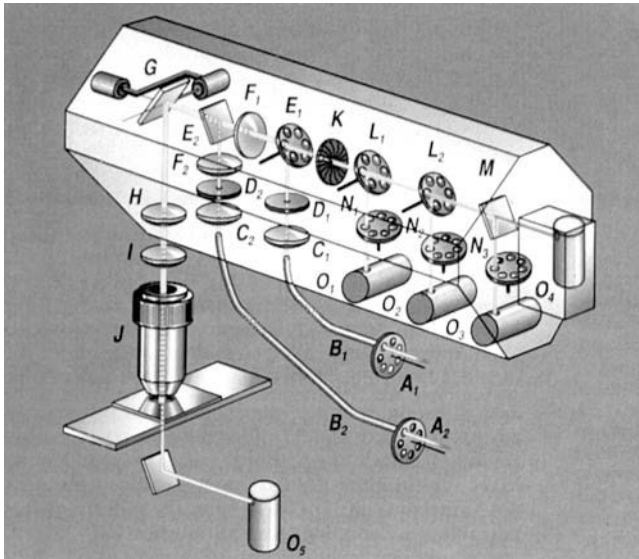


Figure 2.15: Confocal optical ray path and optical components of a Leica TCS scan unit [Winkler 95]

raster movement of the laser beam is achieved by two mirrors that are connected and moved by a galvanometer (fig. 2.15, object G). The spatial illumination of a discrete object point is solved by a scan-lens (fig. 2.15, object H) that is mostly moved by a piezo component, translating the focus point in depth. Other important components of a CSLM scan unit are a rather complex filter and lens system, the laser-beam feed for visible and UV wavelenths (B1 and B2), and the variable pinhole (K). Because the CLSM scans slices of a volume, 3D data points are being generated. Such discrete 3D measurement points are called voxels, analogous to the discrete 2D element of an image, the pixel.

2.5.3 CLSM application

The use of CLSM in life science is well established for a broad range of research activities [Pawley 97], whereas the application in technical and materials science is rather new [Wendt 94, Tiziani 00]. In life-sciences, the CLSM is often used in a so-called transmission mode that is paired with fluorescent staining of the specimen. The laser-beam excites flourochromes sensitive to the given wavelength, and the maximum intensity indicates the spatial position of the fluorescent dye. In materials

science, such staining cannot be applied to most categories of specimen. Rather than the inside, the topography of specimens is examined. This can be done with the CLSM in reflective mode. In this mode, the intensities of the reflected rays are recorded, and the maximum intensity of reflection is calculated from a data column. The voxel with the maximum intensity defines the discrete spatial coordinates of a single measurement point. Often, the determination of the maximum z-coordinates is even improved by applying sub-voxel algorithms to the intensity distribution for better resolution. CLSM data in reflection mode can be acquired from a wide range of samples, if only the minimum requirements concerning reflection are fulfilled. But, because most objects do not behave as perfect mirrors, data from reflection mode have to be carefully interpreted.

LANDMARK-BASED 3D CALIBRATION

Coordinate measurements are usually performed on microscopes without direct linkage to the meter definition. In order to achieve a proper scale definition and to overcome imperfections in the scanning movement, such microscopes have to be calibrated by physical transfer standards for traceability. The development and fabrication of highly accurate dimensional standards has been and still is being pursued by commercial companies and research projects [Koenders 04, Haycocks 05, Dziomba 05]. Here, the foundation of a one-step 3D calibration strategy for the calibration of scanning microscopes is presented as an alternative to existing strategies that are based on separate dimensional calibration by 1D and 2D pitch reference structures (fig. 1.2). However, the focus remains on the linear calibration of scanning distortions.

3.1 COORDINATE MEASUREMENTS

Measurements are performed in order to be able to assign numbers to properties of real-world objects. From this quantification, specifics of the objects' features and behaviour can eventually be deduced, because identical properties of different objects can be compared or correlated to specific influences to which the sample has been exposed. Calibration itself can basically be seen as a refined form of measurement [Eisenhart 63] that is applied to determine systematic errors inherent to the instrument that is or has been used for measuring, or which are induced by other parameters causing a shift in the resulting measured value from the expected or true value.

3.1.1 *General aspects of measuring*

The measured values l_i of an object property have to be derived from experiments, i.e., the measurement process, and the experimentally yielded values can be seen as linked to a physical (e.g., distance), or logical (e.g., flipping a coin) stochastic quantity L representing this property, for example, as the mean or median value with a certain deviation. Here, these values l_i will be referred to as *observations*, and specifically *coordinate observations*, as the emphasis of this thesis is dimensional measurement and calibration.

It is important that for each of the measured values l_i , a probability $P(l_i)$ is assumed in order to guarantee a statistical control mechanism. Of course, the measured values l_i may vary within the probability distribution, but they may also be repeatedly distorted with respect to an expected measurement result, or with respect to measurements of the same property by alternative methods. Therefore, three questions need to be addressed in order to evaluate a measurement process:

- are repeatedly measured values l_i showing specific characteristics under defined conditions?
- is the experimentally derived quantity L close to the true or expected value \tilde{L} ?
- if not, is L shifted from \tilde{L} repeatedly in a characteristic direction or manner?

Precision, accuracy and systematic errors

The first question refers to the *precision* of a measurement. The *precision* describes the closeness of the measured values to each other [Eisenhart 63]. It is usually characterised by the standard deviation σ of the measured values. The second question refers to the *accuracy* of a measurement, i.e., the closeness to the true or expected values. However, it is not possible to use a method, analogous to the determination of the *precision*, in order to describe the *accuracy* of a measurement process. In contrast, the *accuracy* of a measurement can only be described by indicating its *precision* and by knowing the shift of the measurement mean from the expected or true value, that is, the bias in the measurement as referred to in the third question. This shift indicates that something is measured which was not intended, due to a *systematic error* in the measurement process, be it the device, the operator, or another source, and is characterised by yielded values either repeatedly too high or too low.

Calibration

Such *systematic errors* cannot be eliminated by averaging. They have to be minimised by an instrument or standards calibration. The calibration process involves the definition of the measurement model and procedures, including all known systematic influences at certain conditions. It also implies the use of reference structures with values that are known (“true”) or of higher accuracy than the accuracy of the measurement method itself. The calibration process then results in a calibration value and its associated uncertainty which can be used for the correction of the measurement values yielded by the measurement system that shows systematic errors.

3.1.2 Landmark-based calibration

Figure 3.1 schematically represents a hypothetical reference structure with two height steps, indicated by different gray values of the height step areas. On the reference structure there are landmarks applied, also termed control points, which are symbolised by black circles. On the left hand side, the true or statistically narrowed down position of the landmarks is shown, indicated by “true” coordinates $\tilde{\mathbf{L}} = (\tilde{L}_1, \tilde{L}_2, \dots, \tilde{L}_n)^T$. The right hand side depicts the hypothetically measured (e.g., by scanning microscopy) position of the landmarks $\mathbf{L} = (L_1, L_2, \dots, L_n)^T$, obviously retrieved by a measurement device producing distorted coordinate measurement results. The distortions applied in this example are shear to the xy -plane, causing non-orthogonality to the measurement, as well as scaling in z -direction, indicated by a relative shift of the gray values representing the step heights. If such measurement

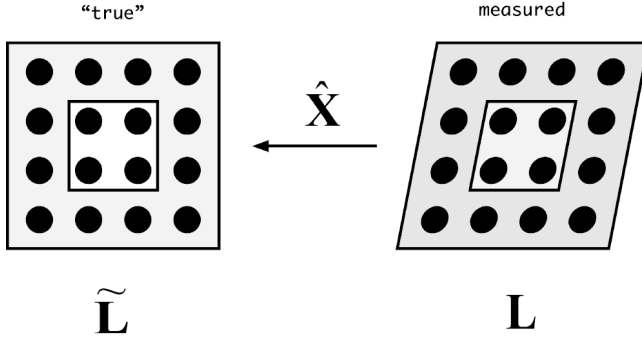


Figure 3.1: Landmark-based calibration principle

behaviour proves to be reproducible, the measuring device shows a *systematic error* and is subject to calibration. Because the 3D coordinates (object coordinates) of the landmarks on the reference structure are known ($\tilde{\mathbf{L}}$), the calibration process involves a geometric transformation of the measured landmark object coordinates to the known landmark object coordinates according to the calibration model, which can be expressed as a function of the parameters $\hat{\mathbf{X}} = (\hat{X}_1, \hat{X}_2, \dots, \hat{X}_u)^T$ or degrees of freedom foreseen in the transformation model that need to be estimated.

3.1.3 Calibration by parameter estimation

The reconstitution of the given coordinates by measurements on a device that has yet to be calibrated, is consistent with the mathematical model of mostly over-determined non-linear equations. Such over-determined systems do not have definite solutions, and the unknown parameters have to be estimated. The least-squares parameter estimation method (LSE) is used to determine the unknown parameters with maximum probability [Niemeier 02]. The functional model of the LSE states very generally that the observations \mathbf{L} plus some small improvements \mathbf{v} (residues) are a function of the estimated unknowns $\hat{\mathbf{X}}$:

$$\mathbf{L} + \mathbf{v} = \varphi(\hat{\mathbf{X}}) \quad (3.1)$$

If approximation values of the unknowns are present (\mathbf{X}_0), then the approximated values of the observations can be calculated (\mathbf{L}_0) and only small values $\hat{\mathbf{x}}$ have to be determined. And if the function φ is linearized by a first-order Taylor series approximation, then the linearized form of [3.1] becomes the functional model

$$\mathbf{l} + \mathbf{v} = \mathbf{A} \cdot \hat{\mathbf{x}} \quad (3.2)$$

where $\mathbf{l} = \mathbf{L} - \mathbf{L}_0$ and $\hat{\mathbf{x}} = \hat{\mathbf{X}} - \mathbf{X}_0$, which is equal to the parameters that are to be estimated. \mathbf{A} is called the design matrix and contains the first links of the Taylor terms

$$\mathbf{A} = \left(\frac{\delta\varphi(\mathbf{X})}{\delta\mathbf{X}} \right)_0. \quad (3.3)$$

With the LSE method, the unknowns are being determined by maximum probability. This is achieved by adding stochastic properties to the functional model: every observation L_i is characterised by its standard deviation and a correlation coefficient between L_i and another observation L_j , formulated in a covariance matrix Σ_{Π} , that can be transformed via the cofactormatrix \mathbf{Q}_{Π} into the weighted matrix \mathbf{P} by

$$\mathbf{P} = \mathbf{Q}_{\Pi}^{-1} = \left(\frac{1}{\sigma_0^2} \cdot \Sigma_{\Pi} \right)^{-1}, \quad (3.4)$$

with σ_0^2 being a variance factor that can be approximated in the first place and will then be determined within the estimation process. In case an infinite number of observations is assumed with Gauss normal distributions, the residues are estimated by LSE with minimum variance:

$$\mathbf{v}^T \cdot \mathbf{P} \cdot \mathbf{v} \rightarrow \min! \quad (3.5)$$

It can be shown [Niemeier 02] that the unknown parameters are estimated within the minimization of the weighted least-squares sum with [3.6]:

$$\hat{\mathbf{x}} = (\mathbf{A}^T \cdot \mathbf{P} \cdot \mathbf{A})^{-1} \cdot \mathbf{A}^T \cdot \mathbf{P} \cdot \mathbf{l} \quad (3.6)$$

As the parameter estimation is constituted not only by a functional, but also by a stochastic model, a variety of statistical information concerning the accuracy of the unknowns and the quality of the model, as well as the quality of the realization in terms of reliability, can be retrieved. The global level of accuracy of the parameter estimation of a given model and observations is expressed by the estimated variance [3.7]

$$\hat{\sigma}_0^2 = \frac{\mathbf{v}^T \cdot \mathbf{P} \cdot \mathbf{v}}{n \cdot u}, \quad (3.7)$$

in which n is the number of observations, and u is the number of the unknown parameters to be estimated. The estimation of $\hat{\sigma}_0^2$ is a possibility to characterize the accuracy of the measurements if, and only if, the functional model (calibration model) and the cofactormatrix [3.4] are correct [Niemeier 02]. The actual accuracy of all of the determined object point coordinates is expressed by the mean point error $\bar{\zeta}_p$ derived from

$$\bar{\zeta}_p = \sqrt{3 \cdot \hat{\sigma}_0^2}. \quad (3.8)$$

3.2 SPM AND CLSM CALIBRATION MODEL

As already pointed out, geometric calibration of scanning microscopes is necessary to achieve accurate dimensional measurements. A great deal of systematic errors introduced into the measurement comes from imperfections of the scanning system. In chapter 2, an overview of the scanning principle is provided in figure 2.1. There, an ideal scanning movement with orthogonality of the scanning axes and constant step sizes in both directions is described. Often, the actual performed scan is only an approximation to that ideal (see fig. 3.1), simply because of limitations of the hardware performing the scan, be it the piezos altering the position of the probe or the stage in SPM or CLSM. An overview of possible distortion factors due to hardware errors, but also due to external factors, such as drift is given in [Henriksen 02].

3.2.1 Two-step SPM calibration parameter retrieval

Currently, the calibration of SPM is performed by separate determination of the correction parameters for lateral non-linearity, and lateral and vertical scale and coupling correction factors [Jorgensen 98]. An additional non-linear parameter of SPM measurement that often has to be corrected is the “scan bow” [West 02]. The effect comes from the curved motion of the SPM scanner over the surface. The motion results in an overlay of a bow to the measured z-values. It can be removed by a leveling procedure of the SPM data, provided the correction function is known.

SPM reference standards

Separate measurement standards exist for the calibration of lateral and vertical scale of SPM instruments. They consist of 1D or 2D pitch standards for the lateral calibration, with a pitch from a few nanometers to several micrometers, or of 1D elevations with a step height up to several micrometers for vertical calibration, as shown in figure 1.2. For example, the National Metrology Institution of Germany (PTB) participated in the development and the calibration of several lateral standards with pitches of 100 nm to 10 μm , and of vertical standards with height steps from 8 nm to 2400 nm [PTB 04]. A special flatness standard for the characterization of SPM scanbows has also been developed [Koenders 04]. However, most calibration standards for SPM are being produced by commercial companies.

Highly analogous to the standard design for SPM, the model of the calibration procedure decouples the estimation of the lateral correction factors from the determination of the vertical correction factors. Also, the characterization of the SPM motion plane is performed in an extra calibration step.

Vertical calibration

The determination of the vertical correction parameter is performed with the help of reference structures of very accurate step height, such as the TGZ03 in figure 1.2b. The height of the step in the measurement is determined either by histogram analysis or by the ISO 5436 method [Dziomba 05]. The histogram analysis uses the maximum and minimum histogram peak difference to characterize the step height. Due to a hard-to-follow, or even unpredictable, behavior of the SPM cantilever at the edges of the step height, only the measured height values on top of the steps and the height values at the bottom of the structure with a certain distance to the height step feature are considered for the determination of the step height by averaging by the ISO 5436 method.

Lateral calibration

The lateral calibration of the SPM, at least, has to consider distortions in the scanning movement by linear correction factors, and eventually by a coupling factor that characterizes shear effects of the xy -plane in the scanning system. Practically, this implies a shift in the start position of the fast scan with every slow scan step. Hence,

for the lateral calibration with 2D gratings, [Jorgensen 98] proposes a transformation model for the description of the correspondence of the observed lattice and the real lattice. The observed coordinates sampled by the SPM measurement are denoted \mathbf{I}' , whereas the known lattice coordinates of the reference structure are denoted \mathbf{I} . In order to reconstitute the lattice coordinates from the observed data, an affine transformation model is chosen [3.9]

$$\mathbf{I} = \mathbf{M} \cdot \mathbf{S} \cdot \mathbf{I}', \quad (3.9)$$

with the matrix \mathbf{M} containing the scaling factors in x- and y- direction, and a shear matrix \mathbf{S} for the description of coupling between x- and y-axis, i.e., the deviation from the perpendicular. Because the model is used for the lateral calibration [3.9], it is denoted for the xy -plane

$$\begin{pmatrix} x \\ y \end{pmatrix} = \begin{pmatrix} c_x & 0 \\ 0 & c_y \end{pmatrix} \cdot \begin{pmatrix} 1 & c_{xy} \\ 0 & 1 \end{pmatrix} \cdot \begin{pmatrix} x' \\ y' \end{pmatrix}. \quad (3.10)$$

The observed coordinates are determined by the formation of a unit cell representing the smallest repetitive part of the grating [Jorgensen 98]. The subsequent parameter estimation is performed by least-squares parameter estimation according to [3.1], with

$$(c_x, c_y, c_{xy}) \in \hat{\mathbf{x}} \quad (3.11)$$

$$(x'_i, y'_i) \in \mathbf{I}'. \quad (3.12)$$

Flatness calibration

Plane correction is a very important aspect in the correction of SPM data. SPM devices do have a non-linear coupling of the lateral coordinates to the z-axis, resulting in a “scanning bow”, as described above. Mathematically, the coupling can be described as a first order plane [3.13], if only a tilting factor has to be estimated

$$z = ax + by + c, \quad (3.13)$$

or as a second order plane [3.14]

$$z = ax^2 + by^2 + cxy + dx + cy + f, \quad (3.14)$$

if to subtract a bow from the measured data. Again, the parameters can be optimally estimated by least-squares estimation according to [3.1].

3.2.2 One-step SPM and CLSM calibration model

There are several advantages in using gratings and in separating the calibration process in a lateral and a vertical subroutine. In the majority of cases, those standards are very accurately made down to very small pitches not feasible by other techniques than by etching methods or lithography. Once a so-called mask - the layout - is established, it can be repeatedly used for the fabrication process. Also, the use of repetitive features usually delivers a sufficient number of dimensional observations for the calibration process. However, such a calibration procedure has various drawbacks:

1. the calibration process involving the separate determination of the correction factors for the lateral and the vertical dimension is rather time-consuming,
2. the reference structures often are of small size, meaning they cannot be produced by optical techniques and, therefore, are fabricated by electron-beam lithography methods at high cost, and
3. most important, it may be hard to detect local correlations of the vertical measurement with respect to the lateral data, when separating the calibration routine into two independent calibration steps.

In other words, by separating the calibration, the determination of the z-correction factor for the calibration measurement is an averaging process not depending on the lateral sampling coordinates, a situation which is not given in actual measurements. In SPM and CLSM, scanning is performed in three coordinate directions, either in response to surface topography changes as in SPM (fig. 3.2a), or through continuously scanned slices of distinct height as in CLSM (fig. 3.2b). By using a reference structure

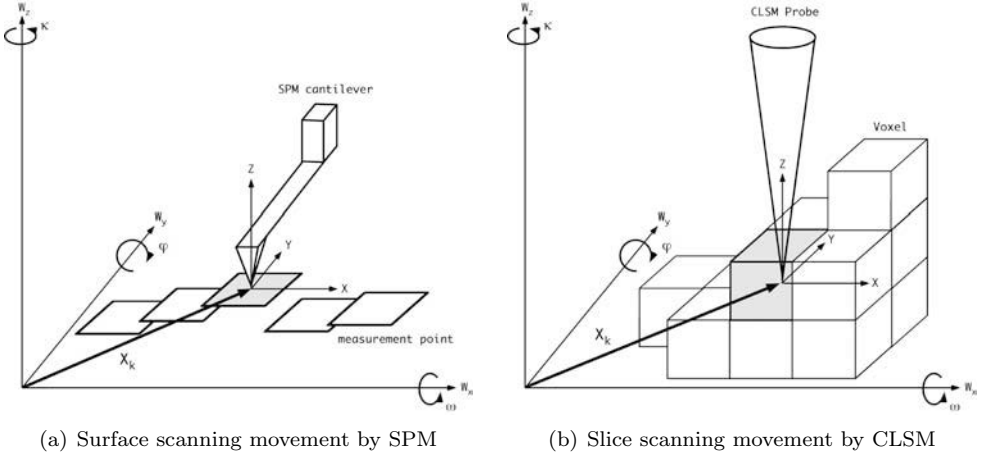


Figure 3.2: 3D microscopy by SPM and CLSM, with static probe (\mathbf{X}) and scanning stage (\mathbf{w})

with known object coordinates, e.g., the landmarks, in contrast to pitch reference structures, the calibration routine need not be separated. An integrated calibration model for 3D calibration in one step is possible, and, as will be shown in chapter 6, models the geometry of the scanning process more accurately.

One-step 3D calibration model based on landmarks

Figure 3.3 demonstrates spatial linear distortion effects on a simple geometric figure (a cube) due to imperfections of the scan generator. On the left side, in figure 3.3a the cube is drawn according to the real world coordinate system \mathbf{X} , whereas on the right side, in figure 3.3b, the original cube is distorted and has become a parallelepiped, due to a distorted measurement coordinate system \mathbf{w} , be it either

linked to the specimen or probe coordinate system \mathbf{u} , or \mathbf{v} , respectively. It can be recognized that the parallelepiped is differently scaled in two directions and also skewed among the xy -plane and the xz -plane. Translated in the physical description of the scanner movement, this means the scan generator applies different step sizes in the x and the y direction. Additionally, it indicates that the slow scan direction and the fast scan direction are not perpendicular to each another, in other words, there are coupling effects between the x and y axes. The obvious skewing in the xz -plane is more difficult to link to physical phenomena. One explanation would be a linearly proportional shift of the scanning position in x -direction depending on the actual z -position of the stage, due to, e.g., piezo misalignment or bending. In order

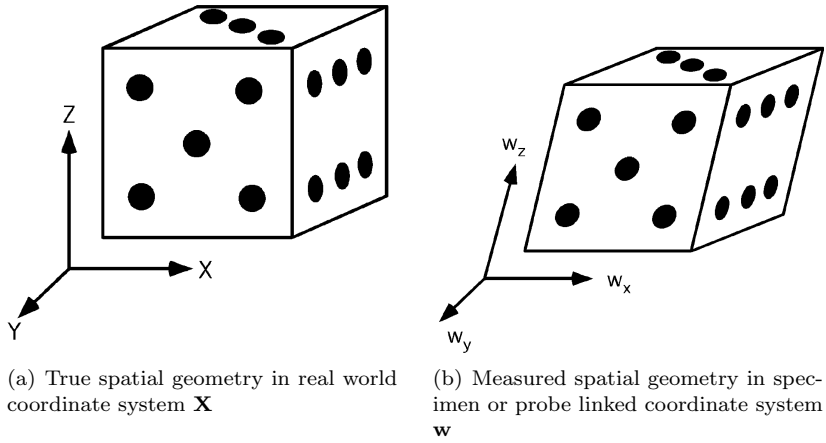


Figure 3.3: Geometric distortions of the of object coordinate measurements by scanning

to restore the original 3D shape of the cube in the measurement, the measurement coordinate system \mathbf{w} has to be transformed to the reference coordinate system \mathbf{x} by including translation, rotation, non-isotropic scaling and shearing, as shown in [3.15]

$$\mathbf{l} = \mathbf{R} \cdot \mathbf{M} \cdot \mathbf{S} \cdot \mathbf{l}' + \mathbf{t}, \quad (3.15)$$

with the rotation elements r_1 to r_9 and the coordinate translation by t_x , t_y and t_z as rigid orientation parameters, and with the scaling factors c_x , c_y and c_z , the shear or coupling factors c_{xy} , c_{xz} and c_{yz} as the actual calibration parameters.

$$\begin{pmatrix} x \\ y \\ z \end{pmatrix} = \begin{pmatrix} r_{11} & r_{12} & r_{13} \\ r_{21} & r_{22} & r_{23} \\ r_{31} & r_{32} & r_{33} \end{pmatrix} \begin{pmatrix} c_x & 0 & 0 \\ 0 & c_y & 0 \\ 0 & 0 & c_z \end{pmatrix} \begin{pmatrix} 1 & c_{xy} & c_{xz} \\ 0 & 1 & c_{yz} \\ 0 & 0 & 1 \end{pmatrix} \begin{pmatrix} w_x \\ w_y \\ w_z \end{pmatrix} + \begin{pmatrix} t_x \\ t_y \\ t_z \end{pmatrix} \quad (3.16)$$

The calibration parameters can then also be estimated according to [3.1], with

$$(c_x, c_y, c_z, c_{xy}, c_{xz}, c_{yz}) \in \hat{\mathbf{x}} \quad (3.17)$$

$$(w_{xi}, w_{yi}, w_{zi}) \in \mathbf{l}'. \quad (3.18)$$

3.3 PHOTOGRAMMETRIC SEM CALIBRATION

There is no method for directly tracing the scanning probe position in SEM, because the signal is received by a stationary detector that samples the amount of electrons at a specific instance. Of course, with respect to the sample stage coordinate system, the scanning position refers to the position of the electron beam. Normally, the positioning is generated by applying a specific current to the deflection coil at the end lens of the microscope, thereby generating an electromagnetic field of a certain magnitude that is proportional to the current, and therefore responsible for the amount of deflection of the electron beam from the central axis. In principle, one could imagine a stationary beam and a moving scanning stage; however, the scanning process in the regular SEM has a dynamic range up to 60 Hz, a frequency too high for mechanical or piezo-steered scanning devices. Still, there are reports of electron optical metrology systems where the scanning position and distortions are calibrated by a vacuum-laserinterferometer traced stage in combination with suitable reference standards [Haessler-Grohne 98]. Such SEM devices designed for critical dimension metrology (CD-SEM) are very important for quality assurance in nanotechnology and in mask analysis in the semiconductor industry. A recent roadmap of the association of semiconductor industry claimed to require 1 nm resolution for the quality analysis of the current production technology [Joy 00].

3.3.1 Calibration standards for SEM

The scanning electron microscope is not a 3D tool in the first place. Therefore, only 2D gratings are available as reference structures for the determination of magnification and distortions. The most common lateral standard is a carbon replica grid with 2160 lines per mm (fig. 1.2a). However, gratings with a smaller pitch and for critical dimension SEM are also commercially available. More variety is offered for the determination of resolution. Usually, evaporated gold on graphite is used. The non-uniform film contains gold islands of the size of a few nanometers that can be analyzed in spatial or frequency domains. Combined standards with a lattice and gold are also available. However, there are several advantages for the calibration of the SEM with a true 3D structure [Sinram 02b]. It is difficult to achieve absolute positioning of a 2D reference standard normal to the central axis of the electron beam column. Such a precondition is needed if, for example, the scale factor of the SEM at certain setting has to be evaluated. Moreover, 2D structures are not suitable because of mathematical ambiguities for the parameter estimation process due to the parallel projection model (fig. 2.13b). Figure 3.4 demonstrates such ambiguities when projecting a 2D reference standard with parallel projection versus central perspective projection. While the central perspective image of the projection is non-ambiguous, the parallel projection yields the same result if tilted in either way, or even if the image being scaled in one direction (fig. 3.4a). However, if using a true 3D object, unambiguous results are delivered for both projections applied (fig. 3.4b).

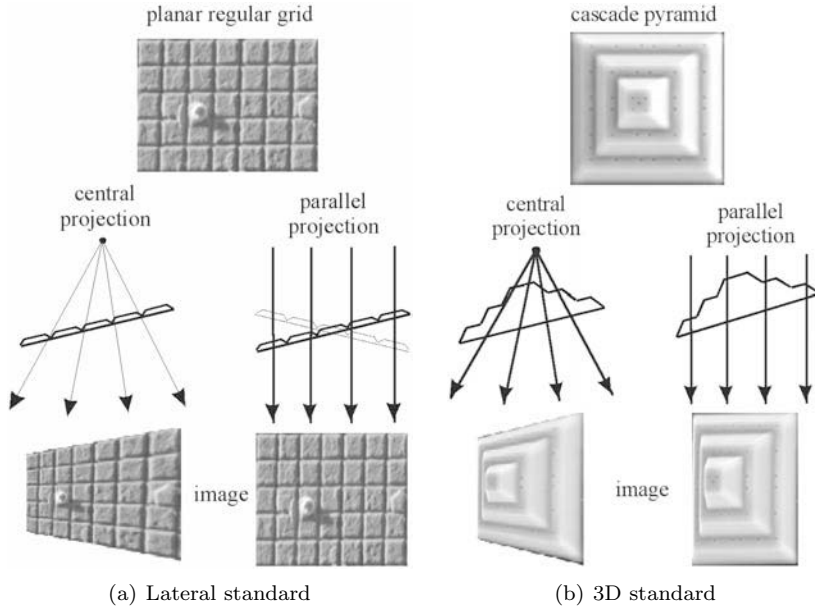


Figure 3.4: SEM projection ambiguities

3.3.2 SEM calibration

For scanning electron microscopes used as a 2D measuring instrument, the calibration procedure has to take into account parameters of the scanning optical system, such as the magnification m or the image constant c_k (fig. 2.13), as well as distortions caused by the imaging process for any adjusted settings of the device. The 3D calibration of an SEM instrument additionally implies the determination of the exterior orientation parameters for any chosen settings. A change in settings may be a change in acceleration voltage, switching the spot size or altering the working distance for imaging. In general it implies an alteration to the scanning parameters of the SEM, and hence a probable change in the interior orientation parameters. In order to mathematically take into account a magnification factor for each scanning direction and the distortions for the calibration of any SEM, the functional model introduced in 2.37 is expanded by the correction terms [Hemmler 01]

$$\mathbf{dx}' = \begin{pmatrix} \Delta x' \\ \Delta y' \\ 0 \end{pmatrix}, \quad (3.19)$$

for the distortion parameters, and by the magnification factor m' . The collinearity equation for the image coordinates then becomes

$$\mathbf{x}' = \mathbf{m}' \cdot \mathbf{R}' \cdot (\mathbf{X} - \mathbf{X}_0) + \mathbf{dx}', \quad (3.20)$$

which again is describing the functional model according to [3.1].

Distortions in SEM images

The distortions in SEM images are caused by the electron optics of the system and are similar to distortions caused by lenses in light optics. In light optics, the radial (symmetric) distortion $\mathbf{dx}'_{\text{rad}}$

$$\Delta x'_{\text{rad}} = r_1 \cdot (x'^3 + x' \cdot y'^2) \quad (3.21)$$

$$\Delta y'_{\text{rad}} = r_2 \cdot (y'^3 + y' \cdot x'^2) \quad (3.22)$$

is mainly responsible for imaging errors. However, errors produced by spiral distortion are of the same magnitude in the SEM [Elghazali 84]. The spiral distortion \mathbf{dx}'_{sp}

$$\Delta x'_{\text{sp}} = t_1 \cdot (y'^3 + y' x'^2) \quad (3.23)$$

$$\Delta y'_{\text{sp}} = t_2 \cdot (x'^3 + x' y'^2) \quad (3.24)$$

is caused by the spiral trajectories of electrons in the electron column. The combination of the distortion $\mathbf{dx}'_{\text{rad}}$ and \mathbf{dx}'_{sp} describes the imaging defects of the electron optical system of any SEM and is summarized as follows:

$$\mathbf{dx}' = \mathbf{dx}'_{\text{rad}} + \mathbf{dx}'_{\text{sp}}, \quad (3.25)$$

with the explicit terms

$$\Delta x' = r_1 \cdot (x'^3 + x' \cdot y'^2) + t_1 \cdot (y'^3 + y' x'^2) \quad (3.26)$$

$$\Delta y' = r_2 \cdot (y'^3 + y' \cdot x'^2) + t_2 \cdot (x'^3 + x' y'^2). \quad (3.27)$$

Determination of the orientation parameters by spatial resection

The reconstitution of object coordinates with SEM instruments requires redundant 2D information, e.g., two or more images of the identical feature at different aspects. Therefore, the SEM 3D calibration process necessitates not only the estimation of the scale factor and the optical distortions of the microscopy, but also the determination of the image orientation, because any accurate subsequent section in space depends on that information. For the calibration process, the least-squares estimation on the basis of the collinearity equations [2.37] (without distortions) or [3.20] (with distortions) is used. In case of a multi-image analysis, this procedure is also called (*bundle block adjustment*), and describes the best possible fit of corresponding (homologous) image rays to their object coordinates. The residues \mathbf{v} of the functional model [3.1] may become a function of all parameters involved, as shown below for the parallel projection case (see fig. 2.13b):

$$v_{x'i} = f(X_{0j}, Y_{0j}, \varphi_j, \omega_j, \kappa_j, m'_{xs}, \Delta x'_s, X_i, Y_i, Z_i) - x'_i \quad (3.28)$$

$$v_{y'i} = f(X_{0j}, Y_{0j}, \varphi_j, \omega_j, \kappa_j, m'_{ys}, \Delta y'_s, X_i, Y_i, Z_i) - y'_i, \quad (3.29)$$

in which i is the index of the homologous points, j is the index of the images and s is the index of the sensors or sensor settings used in the photogrammetric analysis [Sinram 02a].

Self-calibration

When only image coordinates are used within the least-squares estimation using a *bundle block adjustment* for the determination of the desired unknown parameters, the process is called self-calibration [Hemmler 01]. Because there are no natural control points available on SEM samples, the determination of the orientation parameters of a sample imaged with SEM can always be regarded as a self-calibration process and all parameters [3.29] are treated as unknowns $\hat{\mathbf{x}}$:

$$(X_{0j}, Y_{0j}, \varphi_j, \omega_j, \kappa_j, m'_{xs}, m'_{ys}, \Delta x'_s, \Delta y'_s, X_i, Y_i, Z_i) \in \hat{\mathbf{x}} \quad (3.30)$$

$$(x'_i, y'_i) \in \mathbf{l}', \quad (3.31)$$

which are determined by an efficient number of image coordinates representing the observations \mathbf{l}' . The same is true if only scale information is imported, e.g., from a suitable reference structure [Hemmler 01]. The self-calibration offers, as a result, the estimation of all orientation parameters, sensor parameters and the 3D object coordinates.

FIB 3D CALIBRATION OBJECT FABRICATION

Here, the application of focused ion beam devices (FEI Company, Hillsboro, USA) as a production tool of micrometer-sized geometrical structures and reference objects for calibration by metal deposition is established, and added to the instruments' capabilities. Deposition is a common focused ion beam (FIB) technology used by the semiconductor industry for the repair and editing of integrated circuits (ICs), and it is also used in materials research for covering TEM slices during a process called thinning [Giannuzzi 99]. However, FIB metal deposition for building structures for the application of calibration purposes is new. There have been impressive though fancy experiments in building a micro-spaceship [Hoshino 03] and a micro-toilet and wine glass from computer aided design (CAD) models [Kaito 04], but few scientific applications. For the nanofabrication experiments within this work, no CAD models were used, but rather the scripting language *AutoScript* of FEI Company [FEI 00c, FEI 00b], as well as the capability of FEI software to interpret bitmap images that are color coded as deposition patterns [FEI 00d]. The FIB system in combination with *AutoScript* software was also used to apply nanometer-sized nanomarkers onto the deposited structures for landmark-based calibration purposes.

4.1 THE FOCUSED ION BEAM INSTRUMENT

The FIB system is a relatively new tool. It works similarly to a scanning electron microscope, but its capabilities go far beyond imaging [Stevie 04a]. The fundamental difference between FIB and SEM is the use of an ion beam instead of an electron beam. Because ions are much larger and heavier than electrons, other characteristics of sample interaction and imaging apply. In particular, interactions between probe and specimen are far more dramatic than, for example, in SEM. In fact, the high momentum of the ions is transferred to the sample atoms within a short distance. The resulting speed and energy of the sample atoms are eventually high enough to remove them from the surrounding matrix. This process is called *milling* (fig. 4.3a) and can be deliberately applied for the fabrication of micro- and nanostructures [Clampitt 90]. Alternatively, in the controlled presence of a special - e.g., organometallic - gas within the specimen chamber, the ions of the beam interact with the gas adsorbed on the sample surface. The gas is decomposed by the interaction with the ion beam into a volatile organic component, and a solid metallic component attaches to the substrate surface. Continuous decomposition and attachment can be used for a deliberate buildup of micro- and nanostructures. This process is called *deposition* (fig. 4.3b), or, more accurately chemical vapor deposition (CVD) [Overwijk 93]. Both micro- and nanofabrication processes are referred to as *patterning* (fig. 4.3). A short overview and comparison between FIB and SEM parameters is given in table 4.1.

Table 4.1: Comparison between FIB and SEM. Adapted from [FEI 04]

		FIB	SEM
Particle	type	Ga ⁺	e ⁻
	size	0.2 nm	0.00001 nm
	mass	$1.2 \cdot 10^{-25}$ kg	$9.1 \cdot 10^{-31}$ kg
	velocity [30 kV]	$2.8 \cdot 10^5$ m/s	$1.0 \cdot 10^8$ m/s
	momentum [30 kV]	$3.4 \cdot 10^{-20}$ kgm/s	$9.1 \cdot 10^{-23}$ kgm/s
	velocity [2 kV]	$7.3 \cdot 10^4$ m/s	$2.6 \cdot 10^7$ m/s
	momentum [2 kV]	$8.8 \cdot 10^{-21}$ kgm/s	$2.4 \cdot 10^{-23}$ kgm/s
Beam	spot size	nm range	nm range
	energy	up to 30 kV	up to 30 kV
	current	pA to nA range	pA to μ A range
R_p	polymer [30 kV]	60 nm	12000 nm
	iron [30 kV]	20 nm	1800 nm
	polymer [2 kV]	12 nm	100 nm
	iron [2 kV]	4 nm	25 nm

4.1.1 Principles of FIB

Like any other charged particle probe microscope, the FIB instrument consists of a vacuum system, a source, an optical column, stage and detectors. FIB instruments are available as stand-alone single beam devices. However, most recent systems incorporate an additional electron beam column and therefore are called DualBeam (FEI Company, Hillsboro, USA) or CrossBeam (LEO Elektronenmikroskopie GmbH, Bensheim, Germany) Systems. In these FIB/SEM devices, the electron optical column is usually mounted vertically, whereas the ion column is attached to the specimen chamber at some angle with respect to the electron column (fig. 4.1). A big advantage of these combined FIB/SEM systems is the combination of micro-fabrication by the FIB with the possibility of non-destructive imaging in SEM mode. Although single FIB instruments can be used for imaging, there is always some damage to the sample involved, even when using the lowest currents possible for the ion beam.

4.1.2 Application of FIB

Due to its significant capabilities beyond, the FIB technique has been applied in a variety of scientific and technological fields, as well as in industrial tasks, e.g., failure analysis, design modification and process control. First and foremost, the semiconductor industry uses FIB for IC control and modification, as well as sometimes for mask repair [Prewett 84]. Other industrial applications frequently carried out using FIB instruments are thin film head manufacturing and lithography. In life science and

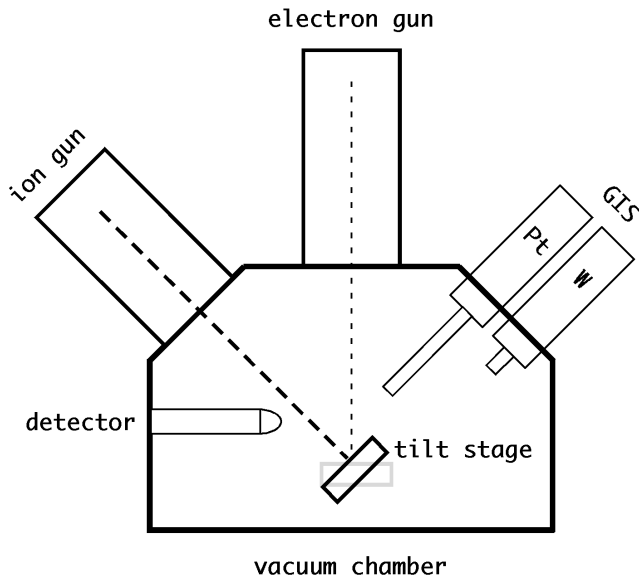


Figure 4.1: Basic components of FIB dual beam systems

materials research, the FIB is used to prepare cross-sections [Vieu 94] thin enough to be analyzed by transmission electron microscopy (TEM). A complete review of FIB applications can be found in [Orloff 03, Stevie 04a].

4.1.3 *The liquid metal ion source*

Field emission was applied to produce a focused ion beam for the first time by Levi-Setti in 1974 [Levi-Setti 74] using a gas field ionization source. Gas sources were soon replaced by liquid metal ion sources (LMIS), because they provide better angular intensity for single component sources such as gallium (Ga) LMIS. Modern FIB systems using a Ga source attain beam currents between 1 pA and 30 nA. The emission of ions from LMIS is a two step process: first building an electric field, and subsequently inducing field evaporation. Field evaporation is the phenomenon in which atoms are ionized in the presence of an extremely high electric field, on the order of a few V/nm. Such high electric field can only be achieved by applying high voltage to a sharp, needle like specimen. There is a trade off between beam current and beam size: with a 5 pA current, an imaging resolution of 5 nm has been attained. In comparison, at a current of 30 nA, the beam size is roughly 1 μm . because the probe size determines resolution, the large beam size has to be kept in mind as a limiting factor for patterning and imaging with FIB.

A LMIS in a modern FIB instrument, e.g., the DualBeam system, consists of a tungsten (W) needle with an end radius of approximately 2.5 μm . The needle is surrounded by a metal reservoir, typically gallium (Ga). The reservoir can be heated by a coiled heater in order to liquify the metal, which then forms a thin film around the needle that stays viscous due to the super-cooling properties of Ga

[Stevie 04a]. Ga is used because it has almost perfect properties as a metal ion source [FEI 04, Orloff 03]:

- Ga has a low melting point of 29.8 °C, which minimizes reaction between the liquid Ga and the W needle
- Ga has a low volatility at the melting point, which promotes a long source life
- Ga has good emission characteristics, in particular, a small energy spread at low emission, and a high brightness
- Ga is nicely positioned in the center of the periodic table and its momentum transfer capability is optimal for a variety of materials.

A high positive voltage on the order of 10 kV is applied to the source with respect to a subjacent extraction electrode, resulting in an electric field of roughly 10^8 V/cm. The liquid metal film is drawn into a conical shape (Taylor cone) in order to balance the electrostatic field and the surface tension forces. The apex of the Taylor cone is reported to be 5 nm [Swanson 83], small enough to extract Ga and to form Ga^+ ions by field evaporation [Orloff 03] with a current density of $\sim 1 \cdot 10^8$ A cm⁻² [Stevie 04a].

The emission of a LMIS is not linear with the voltage applied. Emission only starts if a threshold voltage V_c is reached. V_c depends on the emitter geometry and can vary from 10 kV to a few volts [Orloff 03]. After V_c has been reached, an almost linear ion current increase of 15 - 20 $\mu\text{A}/\text{kV}$ can be observed. However, the source is preferably operated at low emission currents smaller than 3 μA in order to minimize the energy spread that dramatically rises from 5 eV FWHM at 1 μA to 15 eV at 10 μA FWHM [Bell 88]. Additionally, the beam consists of mostly Ga^+ ions and Ga atoms at low emission current, whereas at higher emission current, the probability of Ga dimer, trimer and charged cluster or droplet formation increases [Stevie 04a].

4.1.4 *Beam-solid interactions*

Ion-solid interactions are different from electron-solid interactions (see table 4.1). Due to their substantially higher mass, the range of ions entering into the solid is limited. However, in ion-solid interactions, two basic processes can also be distinguished: elastic and inelastic interactions. Elastic processes cause the displacement of lattice atoms, surface sputtering or defects. The most powerful attribute of elastic processes is sputtering. Inelastic processes produce other forms of energy, such as secondary electrons (SE), X rays and photons (fig. 4.2). The most used feature of inelastic ion-solid processes is the detection of SE for imaging or deposition purposes. Therefore, ions impinging onto the solid can have various destinies:

- Sputtering occurs if the incident ion transfers sufficient momentum to free surface atoms. This feature can be used to fabricate structures or change the existing shape of an object. The momentum transfer can cause surface dislocations and rearrangement of atoms, leading to amorphization in crystals.

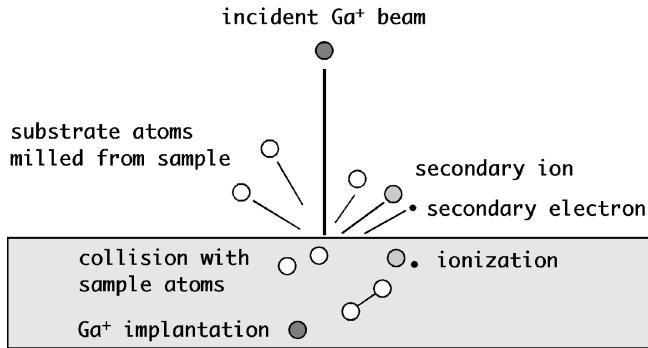


Figure 4.2: Schematic drawing of ion-solid interactions in FIB [FEI 04]

- Ions can be deflected by target material atoms. This process can be used for the analysis of the grain size of multicrystalline materials, because it produces a “channeling” contrast with various intensities depending on the crystalline nature of the grain.
- Implantation of ions of the probe into the target occurs, a feature often used for substrate modification in semiconductor industries [Prewett 93].
- Some of the sputtered atoms are ionized and form secondary ions (SI), the counterpart of SE. They can be used alternatively to SE for imaging, or they can be collected and mass separated for secondary ion mass spectroscopy (SIMS).

4.1.5 Imaging Detectors

Two different types of detectors are used in FIB imaging, a multi-channel plate mounted directly above the specimen, or an electron multiplier (photomultiplier) mounted at an angle at the side of the vertical column, as in SEM devices. The multiplier can be used to detect secondary electrons SE (positive bias) or secondary ions SI (negative bias) [Stevie 04a]. Secondary ion emission occurs when surface atoms are ionized and sufficiently energized to be emitted from the surface. Secondary electrons occur mostly from ion bombardment of metallic surfaces. Both SE and SI carry information about the sample and are used for imaging. The yield of secondary electrons is about 1 per ion and is $\sim 10^2$ times higher than SI yield.

4.2 PATTERNING MODES

As already mentioned, FIB instruments are not used mainly for imaging, but for executing patterning processes in order to fabricate new structures or alter existing ones on the micrometer scale. Two main patterning modes are discerned: milling and deposition (fig. 4.3). Milling creates structures in the sample by removing parts of it (fig. 4.3a), whereas deposition creates structures on the sample with the help of chemical compounds such as organometallic gases (fig. 4.3b). The resolution of

patterning depends strongly on the target material and on the beam current applied, which mainly determines the probe size. As mentioned previously, theoretically, probe sizes as small as 5 nm can be achieved at low beam currents. The patterned

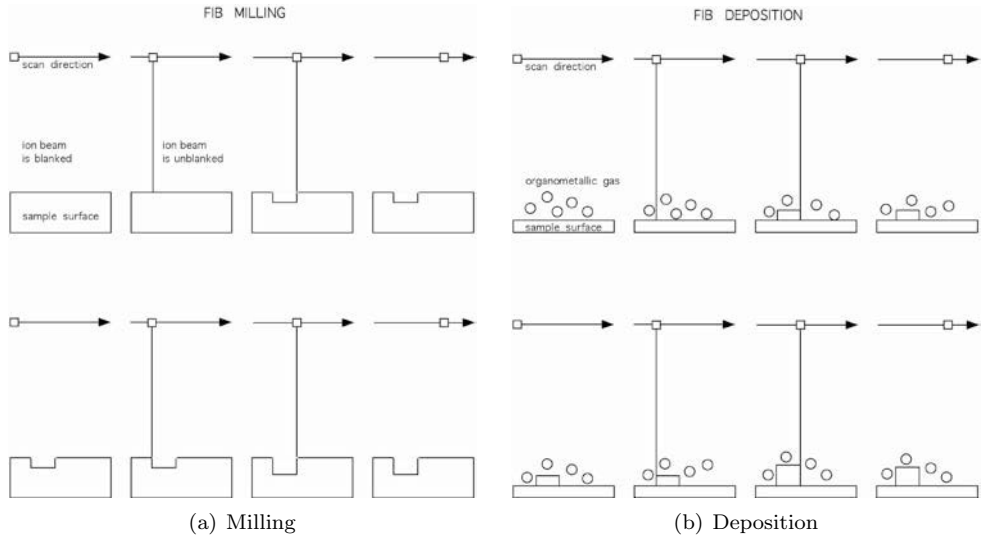


Figure 4.3: Schematic drawing of FIB patterning modes: milling and deposition

structures are smaller than a predefined ROI that is imaged. Therefore, they are digitally addressed only by a fraction n_s of the N_s maximum patterning points available [2.4] for the ROI, e.g., a fraction of the 10^6 points the Nova DualBeam can handle within a selected ROI. If n_s is very small, then the loop time for the structure pattern $t_l = t_d \cdot n_s$ [2.4] becomes very small, which can cause problems in the patterning process, because t_l is too short for the recovery of the organometallic gas [4.6, 4.7]. Hence, a refresh time t_r is introduced. The refresh time t_r is the time that must elapse after the beam has visited a point before it may be addressed again. The refresh time is integrated in the instruments electronic circuit as an adjustable parameter. In mathematical terms this means that if the time t_l is shorter than t_r , a delay $\Delta t'$ is applied before the beam starts scanning the next scan pass of all pattern points n_s . Hence, [2.4] is altered to [4.1]:

$$t'_l = t_l + \Delta t' = t_r = (t_d \cdot n_s) + \Delta t'. \quad (4.1)$$

4.2.1 Milling

The total sputter yield Y for ion energies E_0 is defined as sputtered target atoms per primary ion and can be calculated according to the Sigmund linear cascade (LCC) theory [Orloff 03]:

$$Y(E_0) = \frac{4.2 \cdot 10^{14} \cdot \alpha \cdot S_n}{U_s}, \quad (4.2)$$

in which S_n is the nuclear stopping cross-section, U_s is the surface potential, and α is a dimensionless factor dependent on the atomic mass of the interaction particles involved. There have been other models established for the calculation of the sputter yield Y besides the most common LCC theory. The various models are summed up in [Orloff 03], and complete tables for the factors involved in the Sigmund model [4.2] are provided there as well. The milling or sputtering rate, which is expressed as depth per time normal to the surface, can then be calculated according to [Davies 96] as in [4.3]

$$\frac{dz}{dt} = \frac{Y \cdot M \cdot m_p \cdot I}{A_{sp} \cdot \rho \cdot e}, \quad (4.3)$$

in which M is the atomic mass of target atoms, m_p is the proton mass, I is the incident ion current, A_{sp} is the surface exposed to the ion beam, ρ is the density of the target material, and e is the electron charge.

These theoretical models describe sputter yields achieved in distinct experimental setups. Various effects, e.g., redeposition, influence the sputtering process and result in deviate effective sputter yields (Y_{sp}) and effective sputter rates (Y_r) as shown in table 4.2.1.

Table 4.2: Measured sputter yields [sputtered atoms/primary ion] and sputter rates [$\mu\text{m}^3/\text{nC}$] of a 30 kV Ga beam on various target materials [Orloff 03]

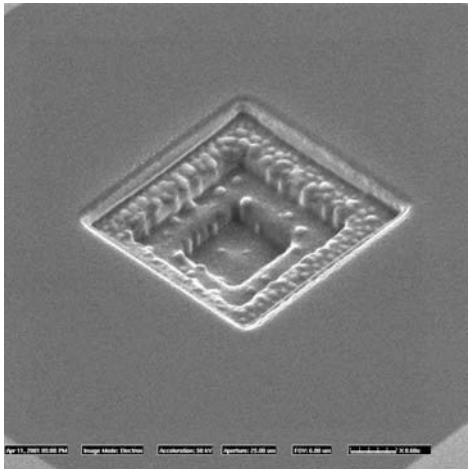
target	ρ [g/cm ³]	Y_{sp} [atoms/ions]	Y_r [$\mu\text{m}^3/\text{nC}$]
C	3.57	2.7	0.18
Al	2.7	2.9	0.3
Si	2.33	2.1	0.26
Ti	4.5	3.4	0.37
Cr	7.19	1.2	0.09
Mo	10.2	1.3	0.12
Ag	10.5	1	0.42
W	19.25	1.2	0.12
Pt	21.47	2.4	0.23

A major drawback of the milling mode for the fabrication of geometric structures is the effect of redeposition. Redeposition occurs when material that has been sputtered away attaches again to the region of the specimen that is actually being milled. The most important factors to consider for redeposition effects are [Giannuzzi 04]:

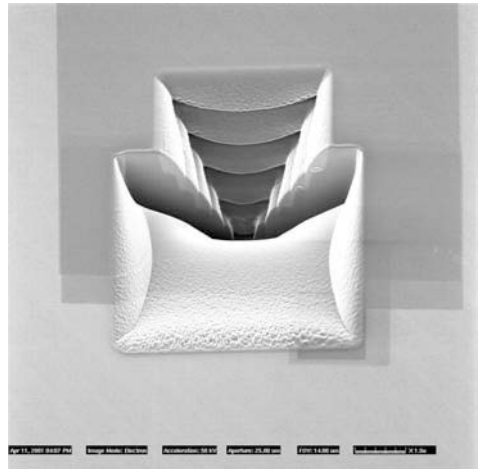
- Kinetic energy of sputtered atoms
- Sticking coefficient of target material g_s
- Geometry of the milled structure

- Sputtering yield of the target material Y_{sp}
- Scan speed

The two variables in the list during a milling process are the geometry of the milled pattern and the scan speed. [Yamaguchi 85] showed that the sputter yield is also a function of scan speed and remains constant if the scan speed is in the range of 0.05-1 cm/s, whereas redeposition increases with high aspect ratios (depth/width) of the milled pattern. At an aspect ratio > 1 , more than half of the sputtered atoms redeposit [Orloff 03]. Figure 4.4 shows the effect of redeposition when milling



(a) Redeposition artifacts on a Si milled structure with low aspect ratio



(b) Redeposition at sidewalls on a Si milled structure with high aspect ratio

Figure 4.4: Effect of Si redeposition during milling

a structure with high and low aspect ratio. Little redeposition occurs at a low aspect ratio, e.g., large width to small depth, as shown in figure 4.4a. If the structure has a high aspect ratio, redeposited material covers a large fraction of the sidewalls, as visualized by FIB cross-section in figure 4.4b. Hence, the idea of creating calibration structures by milling was not followed further. Instead, deposition was used for the fabrication process.

4.2.2 Deposition

The first application of metal deposition was published by [Gamo 84], in which he investigated 50 kV irradiation of a trimethyl aluminum atmosphere by Ar^+ ions or focused Au^+ ions for thin film production. Currently, several such gas precursors are commercially available (table 4.2.2), and compound research is still going on. The time to deposit a film of required geometry using a beam current I is expressed by the deposition yield Y_D [Poretz 92] as deposited volume per unit charge [4.4]. The deposited volume V_d is defined by the selected width w_A times the length l_A times

Table 4.3: Common gases used for metal and carbon deposition [Stevie 04b, Orloff 03]

gas	deposit ratio	resistivity [$\mu\Omega\text{cm}$]
W(CO ₆)	W(75):C(10):Ga(10):O(5)	150
(CH ₃) ₃ (CH ₃ C ₅ H ₄)Pt	Pt(45):C(24):Ga(28):O(3)	70
(CH ₃) ₃ AlH ₃	Al(37):O(27):Ga(26):C(10)	NA
C ₇ H ₇ F ₆ O ₂ Au	Au(80):C(10):Ga(10)	3
Phenanthrene	C	100

the deposition height z , according to (fig. 2.1)

$$Y_D = \frac{w_A \cdot l_A \cdot z}{I \cdot t}. \quad (4.4)$$

The deposition process can be described by a change in density of adsorbed precursor gas molecules. This change is defined by the rate of adsorption of the precursor gas to the substrate, minus the thermal decomposition rate of the precursor gas during a pattern scan loop t_l' [4.1] minus the rate of precursor decomposition by the ion beam during dwell time t_d , minus sputtering of the newly formed film by the ion beam [Orloff 03]. This complex process can be described by [4.5], involving the parameters listed in table 4.4

$$\frac{dn}{dt} = gF(1 - \Theta) - \frac{JN_0\Theta}{e} - \frac{JY(1 - \Theta)}{e}. \quad (4.5)$$

Table 4.4: Parameters for calculation metal deposition

g	sticking coefficient
F	gas flux
N ₀	precursor monolayer density
J	primary ion current density
σ	decomposition cross-section
Θ	precursor monolayer coverage
k _d	thermal desorption rate constant
Y	film sputter yield
e	electronic charge

The necessary condition to convert the precursor gas completely to metal was brought in relation to the instrument parameters that can be controlled by the user, which are the pattern scan loop time t_l' , the dwell time t_d , the gas flux F and the current density J [4.6]

$$\frac{t_l' \cdot F}{t_d \cdot J} = \frac{N_0 \cdot \sigma}{g \cdot e}, \quad (4.6)$$

as shown by [Puretz 92]. As a typical value of the deposition yield, the group found $0.5 \mu\text{m}^3/\text{nC}$ at a loop time t_l' of 2 ms, a current density J of 2 A/cm² and a dwell

time t_d of 100 ns. They estimated the gas flow F of 7.3×10^{16} atoms/cm²s for these calculations. When the left term of equation [4.6] is smaller than the right term, excess precursor gas is present and may influence the metal film characteristics, but only net deposition occurs. If however, the left term is larger than the right term, then - after all the precursor gas has been converted into metal - milling starts to remove metal from the freshly built film, decreasing the amount of deposition. Hence, for deposition, the gas delivery rate to the surface and the ratio of the pattern loop time and the pixel dwell time have to be considered and well chosen. When assuming a monolayer $N_0 = 1 \cdot 10^{-15}$ atoms/cm², a decomposition cross section $\sigma = 1 \cdot 10^{-15}$ cm² and a sticking coefficient $g = 0.1$, a theoretical deposition rate of 10 atoms/ion is obtained.

In a more simple model, [Fu 01] describes net deposition as positive if

$$\frac{t_d}{t'_l} \leq \frac{F \cdot g}{J \cdot Y_D}. \quad (4.7)$$

Equation [4.7] states that an increase in dwell time also increases the chance of net milling. This group found the maximum acceptable dwell time t_d for tungsten to be 1 μ s. In the manual for the FIB instrument user software [FEI 00d], FEI relates [2.4] and [4.6] for platinum deposition in order to be able to determine the aperture, and hence, the most suitable beam current I for a desired area A [μ m²] of the structure to be deposited [4.8]

$$\frac{2pA}{\mu m^2} \cdot A \leq I \leq \frac{6pA}{\mu m^2} \cdot A. \quad (4.8)$$

4.3 FIB FABRICATION OF 3D CALIBRATION STRUCTURES

The development and design of the micro-calibration object were determined by the various demands of the particular measurement methods involved (SEM, AFM, CLSM) and by the FIB patterning parameters available (see previous sections). The

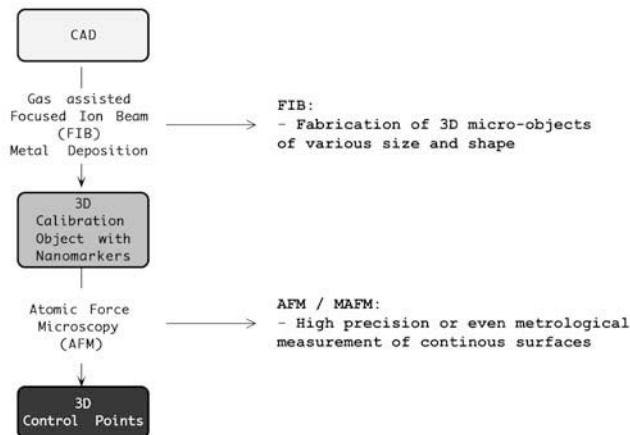


Figure 4.5: FIB: a flexible tool for the fabrication of calibration objects

aim of the present work was to be able to produce versatile 3D structures with FIB metal patterning technology. Because milling experiments resulted in irregularly shaped objects, due both to the substrate silicon crystal structure and to redeposition (fig. 4.4), FIB metal deposition was considered (fig. 4.3b). FIB deposition is a suitable technique for the fabrication of 3D micro-structures, but it does have limitations in the precision that can be achieved [Ritter 05]. One obvious limitation in lateral precision is the ion beam size [Davies 96, Orloff 03, Gierak 05] and another is the line width broadening due to a Gaussian distribution of the beam intensity [Fu 00]. The limitations in vertical precision can be explained by flaws in the theoretical models used for determination of the deposition yield and the deposition rate.

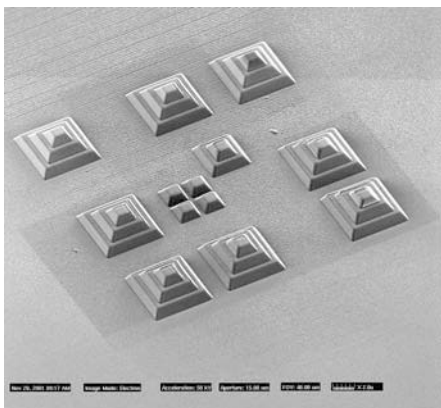
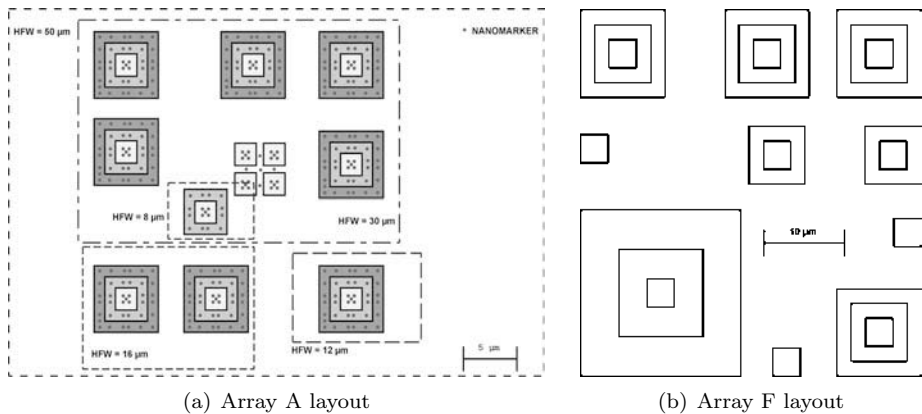
Therefore, the concept of creating versatile, deposited 3D reference structures equipped with milled nanomarkers as landmarks (control points), and in particular the subsequent measurement of the object coordinates of the control points, was developed (fig. 4.5).

4.3.1 Design guidelines

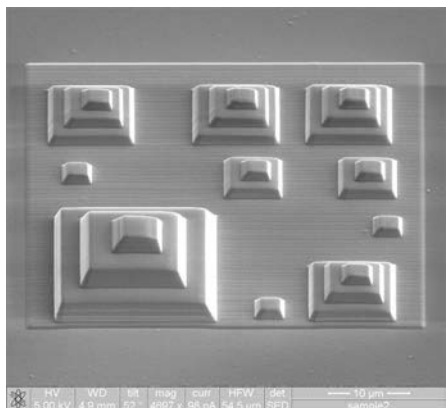
The peculiarities of the calibration process itself had to be taken into consideration when planning the construction of the 3D micro calibration object. In general, it is an advantage in 3D measurement methods if the calibration object covers the measurement volume. This is especially important in 3D measurements with SEM, because the positioning of the calibration object is restricted by the properties of the sample and by the tilting stage. It was planned to create an object for the calibration of SEM instruments at a maximum range of magnifications (fig. 4.6a,b). Therefore, the nominal measures represent objects that are still completely within the range of the depth of focus [2.19], while filling up the field width of an SEM image. A width to height (depth of focus) ratio of 1/10 is roughly valid for SEM [Reimer 98] with an electron probe aperture α_p of 10 mrad. Figure 4.6 shows the design of micrometer-sized calibration objects that are organized in an array. The various objects of the array (fig. 4.6e,f) can be selected and used for calibration according to the horizontal field width (HFW) (fig. 4.6a).

Another limitation comes from the SPM scanner systems, which are limited in lateral and vertical movements. Most SPM scanners can handle a scan area up to $100 \times 100 \mu\text{m}^2$ with a maximum structure elevation of about 8 - 12 μm , but a width to height ratio of 1/8 for large HFW and 1/5 for small HFW is reasonably followed for experiments. Therefore, the height of each single structure was designed to be within these limits (fig. 4.3.1). Additionally, the angle of the pyramidal cascade step slopes with respect to the surface plane was designed to be smaller than the aperture angle of a regular AFM tip, in order to allow exact AFM measurements with as little influence of tip geometry as possible. The aperture angle of an AFM tip usually equals roughly 20° , hence a slope angle Ω of less than 70° should be introduced to the protruding structure (fig. 4.6e).

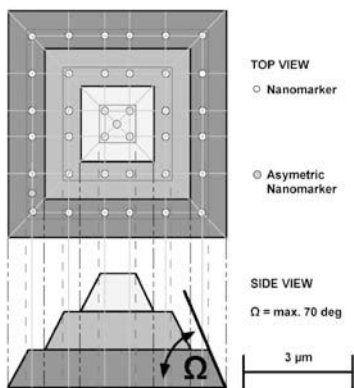
The cascade pyramidal shape of the calibration object (fig. 4.6c,d) is not only suited for AFM measurements, but also allows its use at a broad range of magnification in SEM: due to the sloping edges, the nanomarker control points on a lower



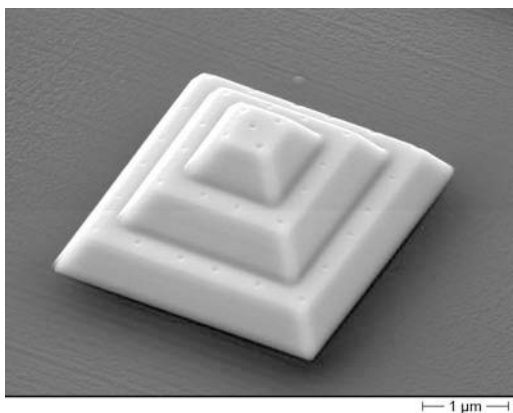
(c) Array A, made with FIB tungsten deposition



(d) Array F, made with FIB platinum deposition



(e) Single pyramid design



(f) Single pyramid of Array A with nanomarkers

Figure 4.6: Array of calibration structures for use at a broad range of magnifications

level are still visible, even if tilted in the SEM for the photogrammetric calibration process. Additionally, a size had to be chosen that could also be detected in confocal laser scanning microscopy (CLSM) instruments for correlative measurement experiments. The calibration structures were applied in an array configuration onto an area of about $50 \mu\text{m}^2$, in order to be able to cope with HFWs of approximately $60 \mu\text{m}$ down to $8 \mu\text{m}$, covering magnifications from roughly 5000x to 40000x on a CRT or LCD screen providing 0.32 m horizontal edge length as shown in table 4.5.

Table 4.5: Magnification and maximum measurable z-difference, due to DOF limitations

0.32 m horizontal screen length	SEM	AFM	CLSM
HFW 100 [μm] magnification max. z [μm]	3200 > 10	3200 < 12	3200 > 10
HFW 64 [μm] magnification max. z [μm]	5000 > 10	5000 < 8	- -
HFW 16 [μm] magnification max. z [μm]	20000 ~ 3	20000 ~ 3	- -

Figure 4.6 shows the schematic design (a,b) and the FIB fabricated arrays (c,d) of pyramidal shaped calibration objects. Arrays of type A were the first to be constructed, and were fabricated by FIB tungsten deposition. Because the single pyramids were too small for CLSM measurements, a redesign of the calibration object led to the type F-arrays, which were fabricated by FIB platinum deposition. Both A- and F-arrays consist of pyramidal objects of various sizes and heights, in order to allow calibration measurements for SEM at various magnifications within the range of an optimum depth of focus. An additional large pyramidal substructure in the F-arrays was included for correlative measurements involving instruments based on light sources, thus allowing calibration of CLSM. The nominal design measures of both arrays, including the pyramidal calibration micro-structures, can be taken from table 4.3.1.

4.3.2 Nanomarker design

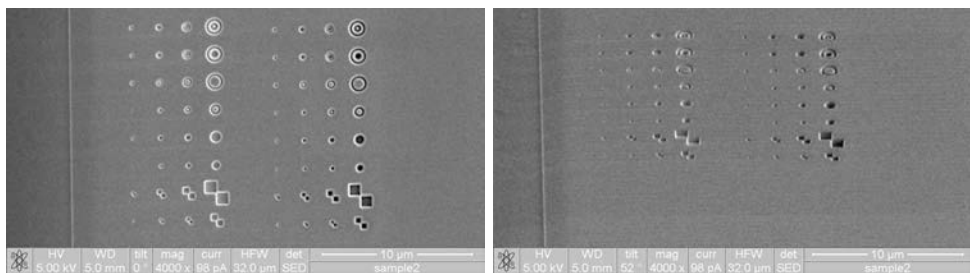
An important task for the landmark-based calibration of scanning microscopes is the choice of suitable nanomarkers as landmarks. This includes the shape of the nanomarkers, their complexity, dimension and depth as design parameters. They must be easy to detect as discrete features in the SEM, the SPM and the CLSM. All of these factors have an influence on the accuracy and reliability of the image coordinate measurement and, therefore, on the calibration accuracy. In the A-arrays, point

Table 4.6: Nominal measures of arrays A and F

	Arrays A	Arrays F
built arrays structures	A2, A12	F03, F04
total area [μm^2]	13 ~ 900	10 ~ 2500
edge length x height big [μm]	-	20 x 4.29
medium [μm]	6 x 3	10.5 x 2.64
small [μm]	4 x 2	7 x 1.76
tiny [μm]	2 x 1	3.5 x 0.88
slope ascent [deg]	63	54

shaped nanomarkers of approximately 80 nm in diameter were tested, whereas in the F-arrays, point shaped (F04) nanomarkers of approximately 120 nm in diameter and ring shaped nanomarkers (F03) of approximately 530 nm in diameter were applied for correlative measurements with CLSM. The distribution of the nanomarkers on the lower level of the calibration objects is non-symmetrical, so that the user is always informed of the pyramids' orientation.

Nanomarkers should fulfill optimal conditions for automatic image measurement and for interactive measurement as well (see chapter 5). The easiest design for subsequent image measurements is a circle or a similar feature. For the A-arrays, nanomarkers were made by FIB milling of simple, filled circles. They were designed to cover an area of roughly 9 pixels in a 1000 x 800 pixel image at a HFW of 32 μm (fig. 4.6 d). For the F-arrays, a field of variously shaped nanomarkers was created by FIB milling, in order to test the optimum control point geometry. The patterned field was used to simulate and test various nanomarker diameters, each suitable in size for selected magnifications (fig. 4.7) in accordance to the HFW as shown in table 4.3.2. The patternfield was made up by 4 different milling areas. Rows 1-2 of



(a) Nanomarker testfield at 0° tilt

(b) Nanomarker testfield at 52° tilt

Figure 4.7: Nanomarker variations at horizontal field width of 32 μm

each area show a nanomarker design based on two rings; rows 3-4 show a nanomarker design based on one ring; rows 5-6 show a point nanomarker design. However, a close range photogrammetry design, shown in rows 7-8, was also tested for automatic image measurement operations. The patternfield also provided different milling depths, in order to be able to determine the most accurate and suitable milling parameters. Milling was done with a beam current of 30 pA. Higher currents were tested in other experiments, but resulted in structures drawn rough and blurry. The milling depth chosen was 150 nm for the upper left field, 75 nm for the upper right, 150 nm for the lower left, and 300 nm for the lower right nanomarker design. The control points were then analyzed *via* semi-automated image processing methods as described in chapter 5. Two nanomarker designs were chosen for the two F-arrays built: the circle

Table 4.7: Milled nanomarker test area

(a) Nanomarker diameter. Upper and lower test area, beam current = 30 pA, milling depth top left = 150 nm, top right = 75 nm, bottom left = 150 nm, bottom right = 300 nm

HFW [μm]		16	32	50	100
nominal [nm]	row 1-3	172	344	537	1074
	row 4-5	109	219	342	684
	row 6	78	156	244	488
	row 7	250	500	782	1562
	row 8	125	250	391	781
HFW [μm]		16	32	50	100
measured [nm]	row 1-3	245	414	646	1146
	row 4-5	208	313	437	741
	row 6	187	266	344	562
	row 7	300	508	772	1502
	row 8	250	276	409	762

(b) Number of pixels with which the nanomarker area was imaged at HFW = 32 μm

		nominal	measured (mean)
pixel	row 1-3	11	13.2
	row 4-5	7	10
	row 6	5	8.5
	row 7	16	16.2
	row 8	8	8.8

design of 109 nm diameter, and the one ring design of 537 nm diameter.

4.4 FIB-FABRICATION OF REFERENCE STRUCTURES

The A-arrays have been designed by the author and subsequently fabricated on commission at the German FEI Application Lab (Feldkirchen, Germany) by tungsten deposition on a Micrion FIB System. Changes in the nanomarker and pyramidal shape design in order to be able to cope with correlative measurements led to the author's production of the F-arrays using a FEI Nova DualBeam used for platinum deposition and imaging at FEI European Headquarters (Eindhoven, the Netherlands).

4.4.1 Sample preparation for FIB

Special care was taken when preparing the holder carrying the wafer piece used as deposition area. The holder consists of a thin ($200\ \mu\text{m}$) aluminum platelet with a diameter of 3 mm. It can be carried and placed with tweezers in SEM sample stages, and it also fits into 3mm TEM specimen holders. The wafer is a single crystal silicon wafer with $\langle 100 \rangle$ orientation manufactured by Virginia Semiconductors (VSI, Fredericksburg, Virginia, USA. Wafer ID 46S036219B). It was chosen for its minimal thickness combined with a negligible resistivity, in order to prevent charging during the calibration measurements in the SEM. It is a p-type wafer with Boron dopant, $200 \pm 25\ \mu\text{m}$ thick and a maximum resistivity of $0.1\ \Omega\ \text{cm}$. For the same reasons, an electrical conductive glue (elecolit 3012, Panacol-Elosol GmbH, Oberusel, Germany) was chosen to mount the wafer onto the aluminum platelet. The elecolit 3012 has a resistivity of $0.0013\ \Omega\ \text{cm}$. The resistivity of the wafer and the glue are still high compared to the resistivity of W and Pt (table 4.2.2), but the lowest available specifications have been selected. After putting the wafer on the platelet, the glue of the holder was baked out overnight at 130 degrees celsius in order to be able to use the mounted wafer in vacuum for FIB as well as for SEM purposes.

Orientation guide on the micro level

The specifications of the AFM scanner used for control point measurements remain in the lateral scan limits of $100\ \mu\text{m}$ and in the vertical limits of $12\ \mu\text{m}$. The $900\ \mu\text{m}^2$ area of the A-arrays was very hard to locate with all microscopes used for calibration experiments. Therefore, an area of $2500\ \mu\text{m}^2$ was chosen as the building site for the microstructures in the F-arrays.

In order to make it even easier to find these small arrays with SEM, and especially with AFM and CLSM, the area of interest was surrounded by a finder frame that was designed according to finder mechanisms of reference structures used for AFM at the Physikalisch-Technische Bundesanstalt (PTB), Braunschweig [Koenders 04]. The finder frame consists of an outer square with an edge length $500\ \mu\text{m}$, a $300\ \mu\text{m}$ inner frame and a 50 to $100\ \mu\text{m}$ area in the middle, covered with 50 - $100\ \text{nm}$ of deposited platinum (fig. 4.8).

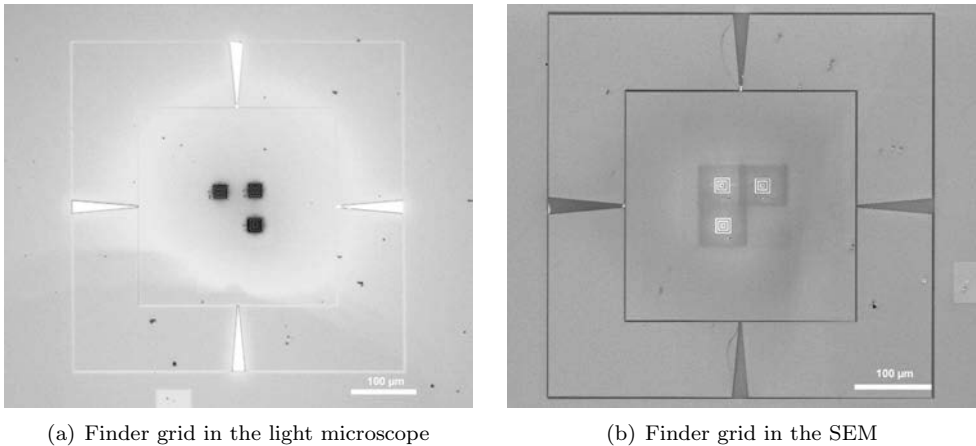


Figure 4.8: Finder grid for easy orientation

4.4.2 Parameters of the deposition process

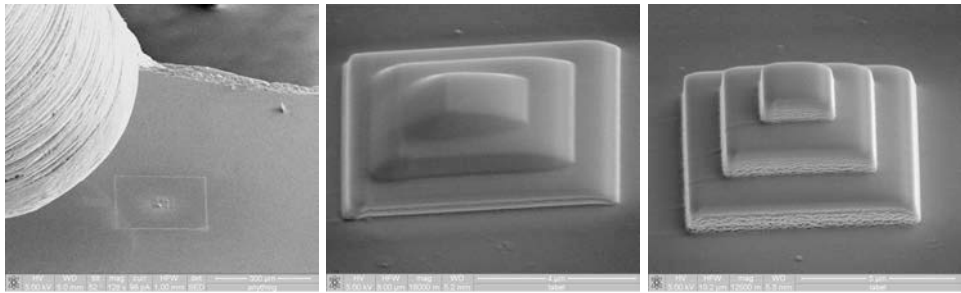
Tables 4.4 and 4.6 list the parameters for the deposition process. A number of experiments have been undertaken in order to determine the influence of the deposition parameters. Parameters that have been analyzed are gas flux F by altering the distance between substrate and needle; the needle orientation; the nominal deposition depth; dwell time t_d ; and the scan mode used for deposition.

Needle distance

The standard setting for the distance of the needle with respect to the deposition ground in many FIB systems is 0.1 mm. The SEM image (fig. 4.9a) shows the gas injection system (GIS) insertion needle for platinum precursor gas at the standard 0.1 mm. However, standard needle distance did not produce objects of sufficient quality (fig. 4.9 b) with the Nova system. Only when the distance was adjusted to at least 0.3 mm to 0.8 mm, could regular structures be created (fig. 4.9c). If the needle was set to a larger range, milling instead of deposition occurred with smaller structures.

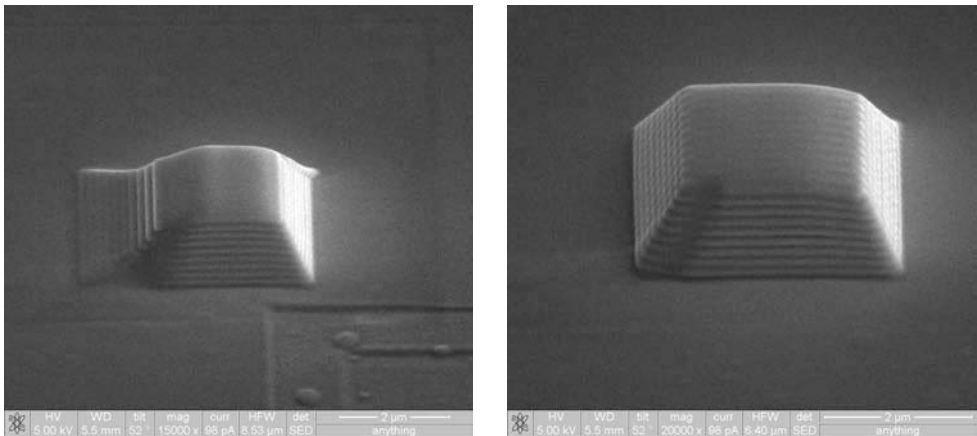
Deposition scan mode

The Nova DualBeam FIB offers two scan modes for patterning: raster and serpentine (fig. 2.1). In raster mode, patterning always starts at the outer left coordinate of a scanning line (fig. 4.10a). In serpentine mode, patterning occurs from left to right in one line, and then from right to left in the next line. Serpentine mode results are of much better quality (fig. 4.10b). The effect (fig. 4.10a) cannot be fully explained, but may arise from certain strategies in the beam blanking [FEI, internal communication]. The term beam blanking refers to the process of deflecting a charged particle beam until the scan coils are set for a new position, or until refresh time t_r has passed.



(a) GIS needle (white tube to the left) with respect to specifications, 100 pA, needle distance 0.1 mm
 (b) 3 step pyramid defined by 3 rectangles, 100 pA, needle distance 0.1 mm
 (c) 3 step pyramid defined by 3 rectangles, 100 pA, needle distance 0.8 mm

Figure 4.9: Pt deposition and needle distance



(a) Raster scan mode

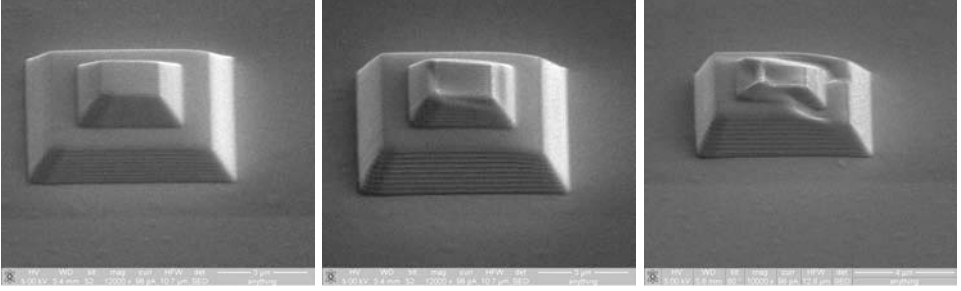
(b) Serpentine scan mode

Figure 4.10: Pt deposition and raster mode (see fig. 2.1 b)

Deposition depth

Another parameter that needed to be considered is the adjusted amount (depth) of deposition. In experiments using a non-standard needle distance of 0.6 mm, several depth parameter settings were analyzed by fabricating a single pyramid. Each slope step of the pyramid consisted of 10 rectangular layers. At each of the layers, the selected depth parameter applies (fig 4.11). Figure 4.11a shows a slope step pyramid made with 20 layers at a current of 0.3 nA. Deposition depth was set to 100 nm. The pyramid has perfect slope shape. Figure 4.11b was made with the same geometry, however deposition depth was set to 150 nm. The bottom part is slightly rounded on the left side. At the top step of the structure, fabrication did not succeed, either due to milling or to an unknown effect. Fig. 4.11c, again built with the same geometry, but at a deposition depth of 200 nm, shows even greater artifacts.

The largest layer at the bottom of the pyramidal structure (fig. 4.11) fills an area



(a) Slope step pyramid made with 100 nm deposition depth per layer (b) Slope step pyramid made with 150 nm deposition depth per layer (c) Slope step pyramid made with 200 nm deposition depth per layer

Figure 4.11: Pt deposition and deposition depth

of $49 \mu\text{m}^2$, corresponding to an edge length 1/3 of the HFW of $21.3 \mu\text{m}$ used as the ROI in which it was fabricated. The smallest layer at the top of the pyramid has an area of $6.25 \mu\text{m}^2$, with an edge length 1/10 of the HFW. The Nova system was set up for a patterning step size n_s [2.2] of 82.5 nm . Therefore, the pyramid roughly consists of $n_s = 7200$ pattern points for the largest and $n_s = 918$ pattern points for the smallest layer [4.9]

$$\left(\frac{7000\text{nm}}{82.5\text{nm}}\right)^2 \leq n_s \leq \left(\frac{2500\text{nm}}{82.5\text{nm}}\right)^2. \quad (4.9)$$

With an adjusted dwell time t_d of 200 ns and a refresh time t_r of 0 ms , t_l' [4.1] varies from 1.5 ms to 0.1 ms . 1.5 ms seem to be long enough for the Pt gas to adsorb, because the very large layers at the bottom of the lower step of the pyramid are of regular shape. However, t_l' calculated for the top rectangle of the lower step of the pyramid is 0.7 ms , and damage can already be observed in figure 4.11b and c. The damage is caused by net milling due to the short loop times for the small rectangles. If all of the adsorbed gas has been used up in the deposition process, no gas is left and the beam starts milling. If the milling yield is greater than the deposition yield for the same fraction of the dwell time, net milling occurs. However, t_l' cannot fully explain the results of this experiment, because a refresh time that is too short should not affect the deposition depth parameter. In fact, all of the three structures shown in fig. 4.11 should show damage. An explanation for why the effect does not occur at small deposition depth might be that there is sufficient gas present at the very beginning for a number of loops t_l' . The total number of loops of course increases if the deposition depth is increased, with the effect that the gas is used up and milling occurs. From a closer look at the structures, one can conclude that milling only occurs at the far side of the GIS needle. This effect might be explained simply by variances in the gas concentration due to the shape of the deposited object itself. The relatively high geometry might hinder the gas from reaching the leeward side. For the structure geometries described in table 4.3.1, an optimum deposition depth of 110 nm for the settings listed in table 4.4.2 has been found.

Needle orientation

Another deposition parameter that was varied was the needle-specimen alignment. However, changing the relative orientation of the specimen with respect to the needle, by tilting plus and minus 10 degrees from the standard position normal to the ion beam, did not produce any differences in the result.

Refresh time

Several refresh times have been examined in order to produce more stable results when fabricating the structures with deposition. A setting of $4 \text{ ms} \geq t_r \geq 2 \text{ ms}$ has been chosen as an appropriate value. Refresh rates smaller than 1.5 ms produced damage on the deposited objects (depending on the whole experimental deposition setup). Refresh rates longer than 4 ms did not show any improvements compared to settings of 2 - 4 ms, and are only more time consuming.

Optimum F-array parameters

In order to establish reliable parameters for the gas-assisted platinum deposition with the Nova DualBeam, experiments shown in previous sections have been performed according to theoretical calculation and published data. An astonishing result was the deviation of the observed parameters from the standard settings that were used. In addition, reproducibility was not always a given. It seems that the most whimsical parameter is the gas flux F , because it depends upon the needle distance and the GIS temperature, and is influenced by the geometry of the fabricated structure, as well.

Results from the various tests for platinum deposition, as well as the results of nanomarker fabrication tests (fig. 4.7) by milling shown previously are summarized in table 4.4.2. Milling is listed at the patterning working distance (PWD), which is at $w_d = 5 \text{ mm}$. The standard PWD value corresponds to an eucentric positioning of the stage with respect to the electron beam [2.21].

4.4.3 Automating the FIB production process

Working with geometric structures such as rectangles and circles, produced good initial results when patterning simple shapes by manual input at the Nova GUI. Because a manual input of a whole calibration array was unthinkable, two automation processes were tested: data input *via* bitmap images and data input *via* script code.

Patterning by color coded bitmaps

The FEI DualBeam software allows any 24 bit bitmap to be used in order to define pattern points. The pattern is generated by the interpretation of blue, green and black components of the bitmap [FEI 00d]. A point is patterned for a certain time if the blue component is non-zero. The blue component defines the pattern point dwell time t_d on a logarithmic scale, with the minimum value 100 ns for blue = 1, up to 4.6 ms at maximum for blue = 255. Again, if dwell time becomes too large,

Table 4.8: Optimum parameters evaluated for F-array fabrication

Parameter	Arrays F	nanomarker F03	nanomarker F04
gas type	Pt	-	-
GIS needle [mm]	0.35	-	-
PWD [mm]	5	5	5
HFV [μm]	51.2	-	-
beam current [pA]	300	30	30
shape	rectangles	circle	ring
size [nm]	≤ 20000	537 nm	100
depth [nm/layer]	110	150	150
t_d [s]	$200 \cdot 10^{-9}$	$1 \cdot 10^{-6}$	$1 \cdot 10^{-6}$
t_r [s]	$2 \cdot 10^{-3}$	0	0
d_o [%]	0	50	50

milling occurs instead of deposition, especially with small structures, such as the top of the pyramids shown in figure 4.11c. The green component in the bitmap defines the beam blank flag. If green = 0, the beam is blanked and no patterning occurs. The black component (red = 0, green = 0, blue = 0) defines the points that are not addressed as pattern points at all. In fig. 4.12a these points are shown in white, for better visibility.

In practice, only short dwell times (100 - 200 ns) were suitable for platinum deposition, leaving only few discrete settings for varying the dwell time on the logarithmic scale. For the experiment shown in figure 4.12b, the height of the geometric structures was defined by the beam blank flag and the dwell time t_d (green = 1, blue = 1 to 20), e.g., small values of blue for less prominent structures, and higher values of blue for the more elevated structures.

The loop time t_l' for a 10^6 pixel bitmap as used in the experiments shown in figures 4.12b,c is at least 100 ms at the minimum dwell time of 100 ns, and if only one fourth of the pixels of the bitmap consists of defined pattern points. These 100 ms loop time is sufficiently longer than the 4 ms found as an optimum value (table 4.4.2). Hence, no net milling resulted in the experiment of patterning an array of the size of $50 \times 50 \mu\text{m}^2$ as shown in figure 4.12b.

However, the use of various color coded dwell times in order to define the deposition depth did not produce geometrically defined objects. The structures are not well proportioned, and they become smaller with increasing lateral distance to the GIS needle. As the whole array is subject to patterning with every loop t_l' , irregularities multiply with each single scan loop. In addition, drift becomes an important factor that influences the result, due to the large time span and the parallel fabrication of all the elements of the array.

The effects of drift could also be observed when using layers of bitmaps with consistent dwell time, instead of just one bitmap. For this experiment, 10 bitmaps, each with $t_d = 200$ ns, were patterned in series (one after another), as shown in figure 4.12c. The structures of the resulting array are quite well defined, but not at all symmetrical, and not nearly congruent to the nominal design parameters.

The biggest obstacle in the experiments shown in figures 4.12b,c is the large pattern area that addresses all pattern points in a parallel way. Even with the modified setup of using bitmap layers (fig. 4.12c), and with each scan point patterned only with a short t_d of 100 - 200 ns, it still took an extremely long time in the range of hours for a single structure to be built. Within that timespan, drift and other parameter variations affect the result, and only blurry or irregular patterns are obtained. Therefore, the idea of using bitmaps as a relatively simple parallel automation tool was dropped in favor of a serial production of all of the elements within the array (fig. 4.12d).

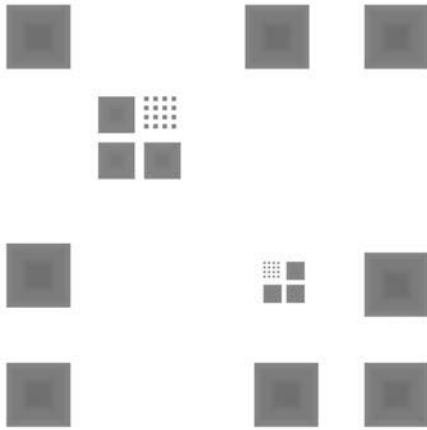
Patterning by AutoScript

As shown previously, parallel processing of the pattern area by interpretation of 24 bit input via bitmaps did not produce the expected results. Therefore, the serial automation method *AutoScript* [FEI 00a] was tested for input of pattern data. Figure 4.12d shows the resulting array, fabricated by programmed *AutoScript* files. For that purpose, the coordinates of the array features were extracted from bitmaps and manually converted into single geometrical objects that could be defined using the *AutoScript* script language. An automation routine, as well as basic possibilities for the redesign of each pyramidal element were implemented in the code. The patterning parameters used for this experiment were slightly different from the optimum parameters. A beam current of 100 pA was applied for a nominal deposition depth of 600 nm for each geometric element of the array. The larger pyramids, for example, consist of 10 rectangles per slope step, totalling 20 rectangles for the entire object. The smaller cubes consist of only 2 to 10 rectangles.

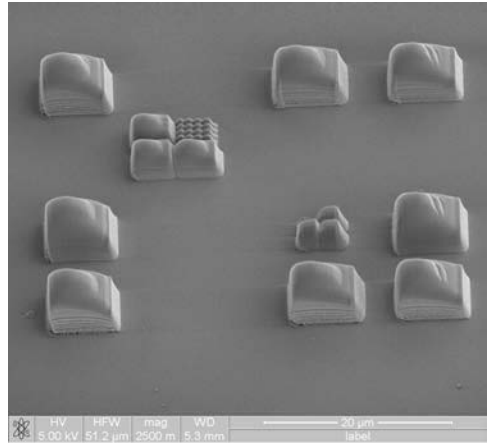
The limiting factors using *AutoScript* were the code interpreter and the GUI. A regular script for an array in which each structure is built with 10 rectangular elements per step contains roughly 100 or more geometrical elements in total. The empirical limit of the Nova DualBeam software at that time was approximately 400 geometrical figures.

4.4.4 Results

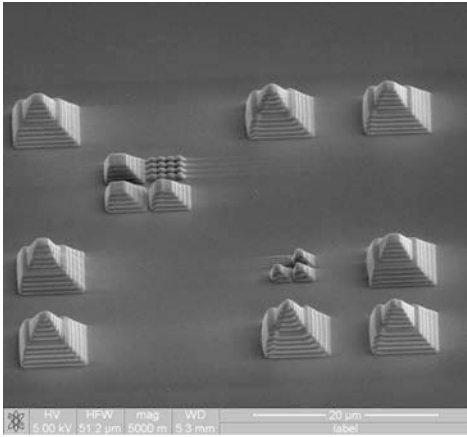
Figure 4.13 shows SEM images of the FIB fabricated F-arrays F03 and F04. Although both arrays were patterned with the same script and parameters, they show slightly different geometries. Array F04 carries an artifact on the top level of the largest pyramid, whereas no patterning errors occurred in array F03. On array F03, ring nanomarkers of 537 nm radius and a depth of 150 nm were milled, whereas array F04 was equipped with circular nanomarkers of 100 nm radius and 150 nm in depth.



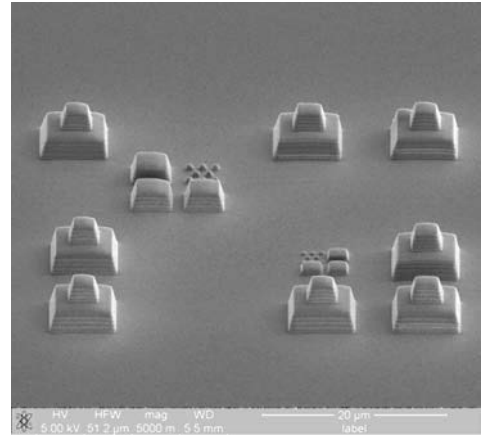
(a) Color coded Bitmap of Test Array



(b) Test array, Pt deposition with 1 color coded bitmap of 4 megapixels



(c) Test array, Pt deposition with 10 color coded bitmaps of 4 megapixels each in series

(d) Test array, Pt deposition with *AutoScript***Figure 4.12:** Automated Pt deposition by color coded bitmaps and *AutoScript* [FEI 00b]

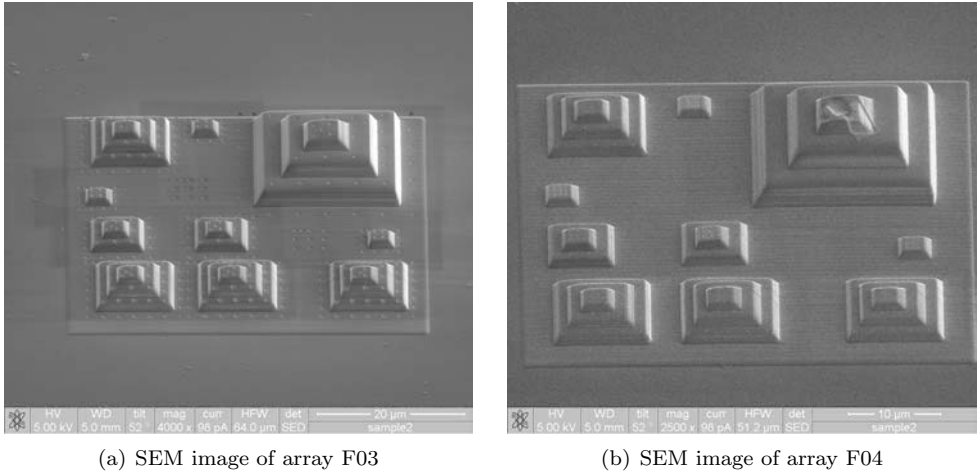


Figure 4.13: Results of the nanofabrication of calibration arrays F03 and F04 by FIB patterning

4.5 SPM MEASUREMENT OF ARRAYS A AND F

For the SPM measurements of the FIB fabricated arrays, a modified SIS NANOSTation II (Surface Imaging Systems, S. I. S. GmbH, Herzogenrath, Germany) based on a Axiotech 100 H (Zeiss, Oberkochen, Germany) at the Physikalisch-Technische Bundesanstalt (PTB, Braunschweig, Germany) was used. The NANOSTation II offers the combination of a light microscope and a non-contact AFM, with the AFM-head plugged into the turret, like the optical objectives. The system can thus be switched between the optical and AFM mode by simply turning the turret and changing from an optical objective to the AFM-head. Large samples up to 200 mm can be investigated with a maximum lateral AFM scan range of $109 \mu\text{m}^2$ and a maximum range of $20 \mu\text{m}$ in z direction. While the instrument does not belong to the highest accuracy class of metrologically optimized AFM instruments, members of which are usually equipped with laser-interferometric position control, the SIS AFM accuracy is based on a closed-loop, capacitive controlled xy -piezo scanner and a piezotube with strain gauges for z -measurements. The apparatus is housed in an acoustic chamber in the PTB cleanroom center, where it is operated under very stable ambient conditions.

4.5.1 SPM measurement setup

For the calibration of the SPM, special care was taken to ensure that stable conditions had been established before starting the actual measurement, such that the system had reached its (e.g., thermal) equilibrium. For the measurements performed, an idle time of 5 hours was required to reach an air temperature stability within the chamber of better than 0.1 K. However, due the dynamic behaviour of the piezo-stage and possibly of the mass of the object to be moved by it, non-negligible distortions of the recorded images and a wrong scaling of the scan range do occur. The magnitude of these influences strongly depends upon the scan-speed. Distortions of ± 100

nm in the fast scan direction were measured within the scan range of $109\ \mu\text{m}$ at a scan-rate of 0.1 lines/s (a scan speed of $10\ \mu\text{m/s}$), whereas no detectable distortions were observed in the slow scan direction. Similarly, the strain gauge to determine the elongation of the z -piezo showed nonlinearities up to 1 % for heights in the range from a few tens of nanometers to a micron. The digital equipment currently allows a maximum of 1 megapixel on each of the 8 channels (16bit). In its present configuration, the closed-loop xy -scanner of the SIS AFM has a positioning accuracy of 10^{-5} , i.e. approx. 1 nm. The correction factors were delivered by the PTB. In order to make sure that uncertainties could be further minimized, all measurements were performed with 90 degrees rotated samples.

The SiS NANOSTation II allows the sampling of data in 7 different channels. For the measurements of the A-arrays A2 and A12 and the F-arrays F03 and F04, 5 to 7 channels were used for data sampling. Channel 0 sampled topographic data corresponding to the voltage applied to the z -piezo. However, channel 0 z -data were not used for measurements, because channels 1 and 2 were recording topographic information from the strain gauge setup. Channel 1 sampled forward scan direction data, whereas channel 2 was used for the reverse direction. Accuracy of z -direction data measured using strain gauges is within expected uncertainties of 1 % in both the reverse and forward scan directions and, hence, much better than what can be expected from channel 0 data. Additional phase shift between the oscillation voltage that is applied to the piezo for non-contact measurement and the mechanical frequency of the cantilever was measured using channels 3 and 4. The phase shift is measured by an optical interferometer; channel 3 recorded the forward scan direction and channel 4 recorded the reverse scan direction. Channels 5 and 6 measured the error signal of the nominal oscillation amplitude and the actual oscillation amplitude of the cantilever during forward and reverse scan.

The raw data obtained were stored in the proprietary SIS format, but data from every channel and all measurements were converted into 16 bit BCR format, which is commonly used for SPM data and supported, e.g., by “Scanning Probe Image Processing” (SPIP, ImageMetrology, Denmark) software. For the channel 1 measurements, levelling was applied by subtracting a plane of first order. The plane was calculated from areas in which no deposited objects were present. Additionally, relevant topographic channel 1 data were filtered by a gradient kernel, in order to make the nanomarkers clearly visible. All channel 1 data were also exported as ASCII data for further processing, e.g., semi-automatic nanomarker search routines (see chapter 5). For the amplitude error data from channels 5 and 6, Gauss-filtering was applied to eliminate outliers.

4.5.2 AFM measurement results

Channel 1 data were used for calculating the lateral and topographic results of all measurements. Gradient images, 2D color coded topographic images, and 3D plots were derived from processing the channel 1 data with dedicated software. The applications used for data interpretation and analysis were ImageSXM (v. 1.75, modification of NIH Image by Steve Barrett, University of Liverpool, United Kingdom) and SPIP (v. 1.85, Image Metrology, Denmark).

Array measures

The shape of the pyramidal array did not cause any problems for measurement with the SIS AFM. Moreover, all nanomarker designs (A2, A12, F03 and F04) were detectable in the AFM, although A2 measurements did not succeed as well as the other arrays, because a lot of dirt was found on the specimen (fig. 4.14a). On array A12, damage at the top of two pyramids on the right side (fig. 4.14c) can be seen, which happened during sample preparation for SEM calibration measurements. However, due to the large number of control points on the array, only a small percentage of them was actually destroyed and enough nanomarkers were left for calibration measurements.

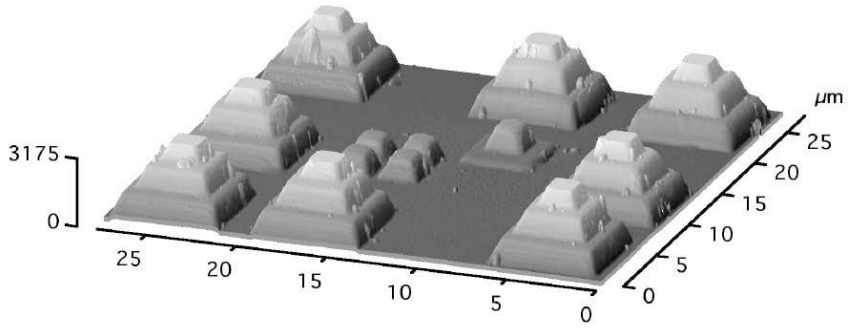
Elements in the arrays F03 and F04 do show rounded plateaus (fig. 4.14b,d). Comparing left and right side on each pyramid, the plateaus are of different widths. Again, the effect is most likely caused by the GIS needle-specimen geometry for platinum deposition. For the same reason, array elements show nonidentical gradients at the left and the right side of the pyramidal slopes.

Arrays F03 and F04 were planned substantially larger and higher than arrays A2 and A12. Height and gradient distributions of the AFM measurements of A2 and A12 are presented in figure 4.15, while those of arrays F03 and F04 at 0° and 90° are shown in figure 4.16. The maximum elevation of both of the F-arrays is $7 \mu\text{m}$, if the base plane is subtracted (fig. 4.16a), whereas the maximum elevation for the A-arrays is $2.2 \mu\text{m}$ (fig. 4.15). The extremes of both arrays were well below the maximum for AFM measurements within a reasonable z-range.

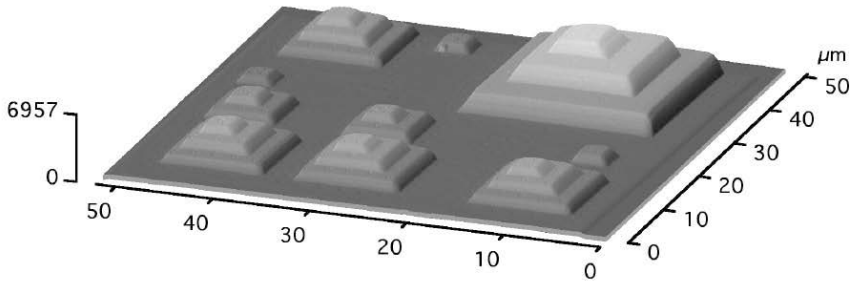
Moreover, the slope gradient of both arrays remained in the range of the maximum nominal values. AFM measurements of arrays F03 and F04 showed gradient peaks at a maximum of 60° (fig. 4.16b). The gradient distribution diagram of both arrays shows double peaks at or below 60° . This effect can also be seen on A2 array (fig. 4.15) and originates from different gradients in the slopes of the pyramidal structures. The peak is more prominent in the 0° than in the 90° measurements, because of the needle-specimen setup during FIB deposition. A summary of the array measurement results is given in table 4.5.2.

Table 4.9: Dimensions for A-arrays and F-arrays measured by AFM

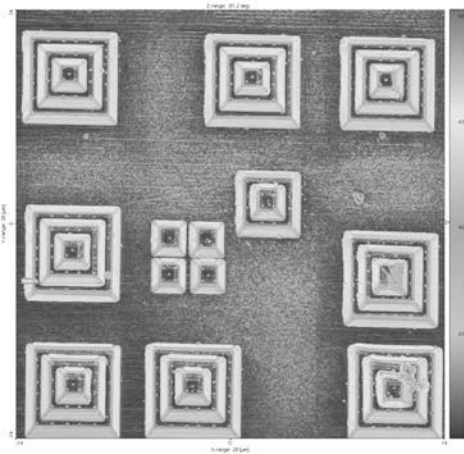
Array	A2	A12	F03	F04
max. measured height [nm]	2500	2600	7000	7000
max. measured ascent [deg.]	70	63	70	70
mean nanomarker radius [nm]	40	90	537	100
mean nanomarker depth [nm]	30	33	60	45



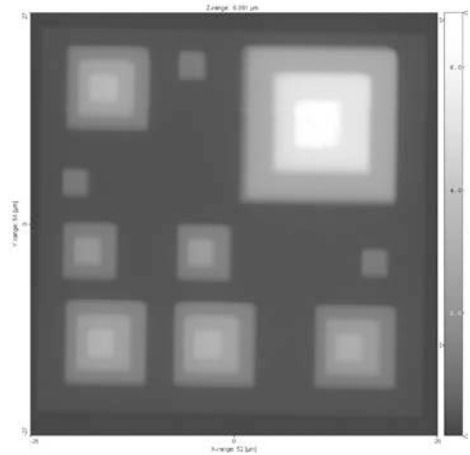
(a) 3D representation of A2 topography



(b) 3D representation of F03 topography



(c) Color coded representation of A12 gradient



(d) Color coded representation of F04 topography

Figure 4.14: SIS AFM measurements of A-arrays and F-arrays

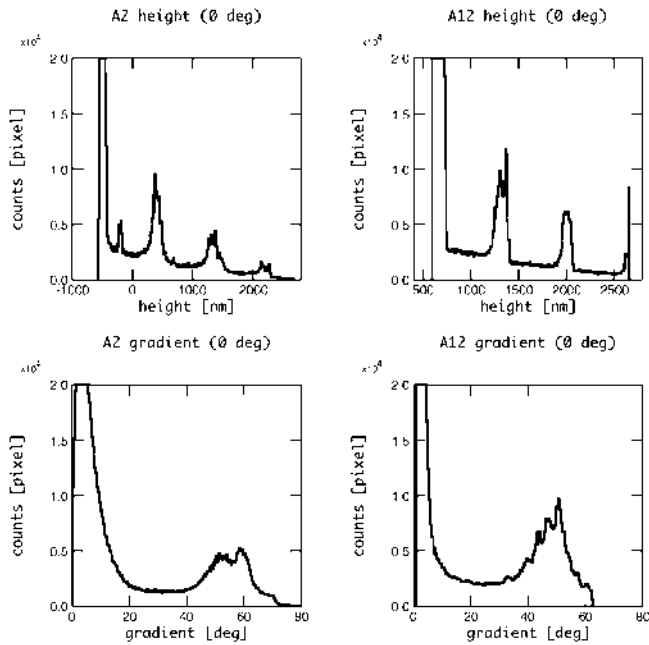
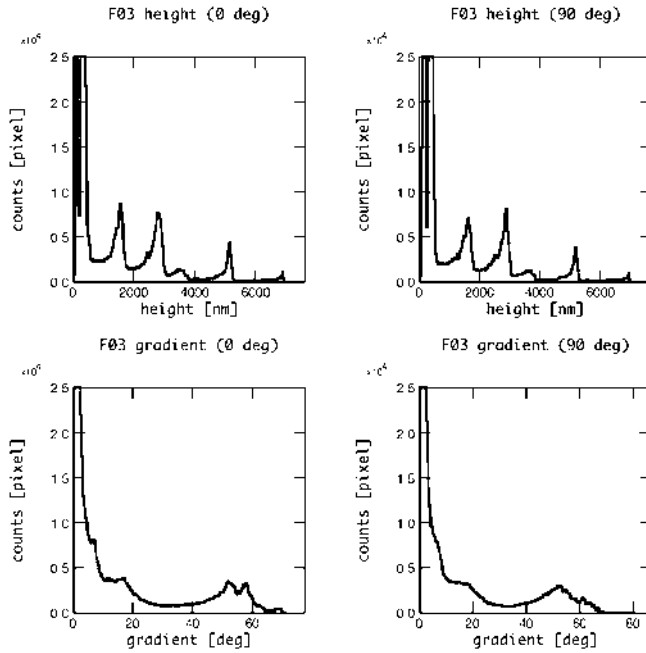


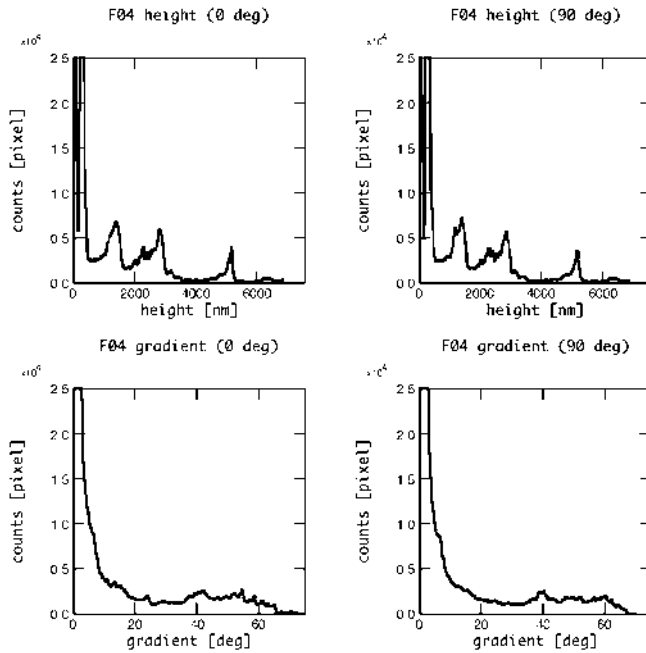
Figure 4.15: Height and gradient distribution in SIS AFM measurements of A-arrays

4.6 ACCURACY OF FIB DEPOSITION

One of the important points to analyze was the accuracy of deposition, i.e., how do the measured values compare to the nominal values calculated for this procedure. Lateral measurement data could be taken directly from the SEM images of array F04, because the SEM scale was obtained from photogrammetric calibration. Height data were obtained from the SPM measurements of arrays F03 and F04. For the fabrication of F03 and F04, a deposition depth of 110 nm per rectangle (layer) was set. Figure 4.17 shows the nominal height settings of the pyramidal substructures below the x -axis. The number within the columns indicates the actual height of the deposited platinum, derived by the measurement of the nanomarkers at corresponding step size. The number of measured nanomarkers can be indicated by the number at the small black points. Deviation of the actual from the nominal height yields error factors of up to a remarkable 1.5 for the largest substructures (actual 6370 nm vs. nominal 4290 nm). As no obvious relation between the actual height of the structures and the nominal height was detectable, the error factor was brought into linear relation to the lateral area (fig. 4.18). From figure 4.18, it can be concluded that the actual deposition height is linearly dependent upon the deposition area and increases proportionally to the selected area size.



(a) F03 histogram analysis of height and gradient



(b) F04 histogram analysis of height and gradient

Figure 4.16: Height and gradient distribution in SIS AFM measurements of F-arrays

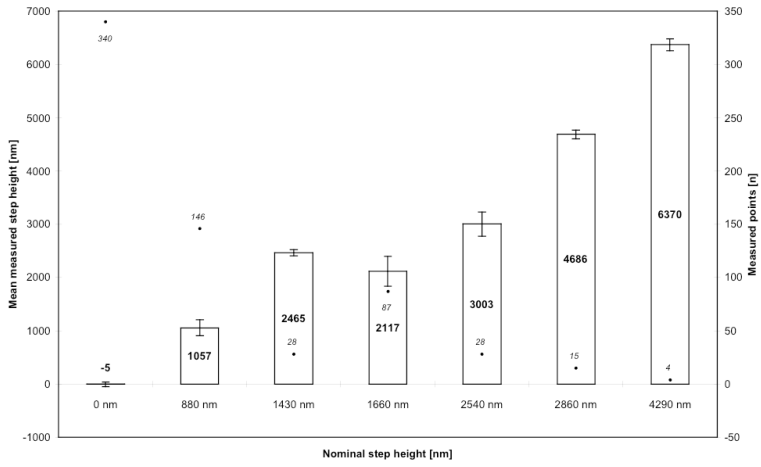


Figure 4.17: Mean deposition deviation from nominal settings

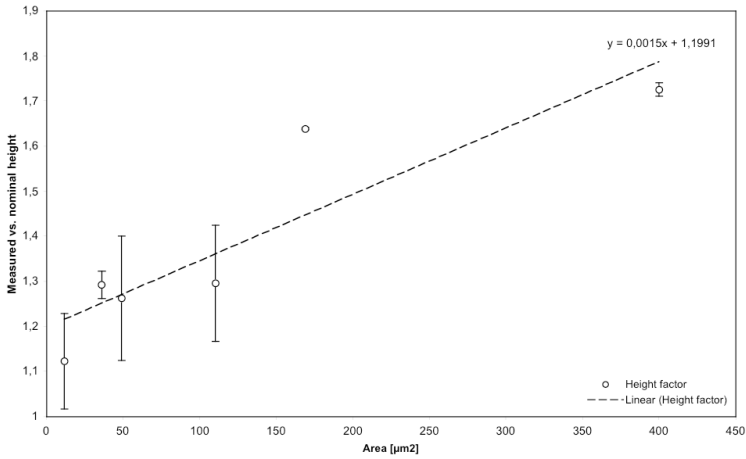


Figure 4.18: Height factor vs. lateral deposition area

CONTROL POINT DETERMINATION

The calibration strategy for micro-range measurement methods presented here is based on landmarks, which are also called control points or fiducial marks, and in this work are referred to as nanomarkers, due to their small size. Landmarks in general are unambiguous, easily recognizable, geometrical features on real objects that define object point coordinates in 3D measurement data. Because landmarks define discrete positions on a real object, they are widely used for coordinate measurements and calibration purposes in close-range applications [van den Heuvel 92]. The use of landmarks for micro-range measurements and below is not yet established, although a few applications have been reported, such as for quality control of SPM cantilevers [Hemmler 95], and for medical applications, e.g., for the registration of computer tomography images of the head in order to allow microsurgery [Maurer 98]. Several

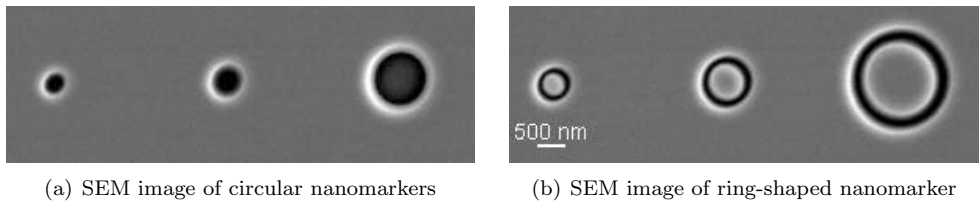


Figure 5.1: Landmarks in micro-range measurement data

geometries of such features exist and have been tested (fig. 4.7). Among the most common geometries is the circle (fig. 5.1a), in which the perimeter depicts the chosen geometrical feature of the landmark, and the center maps the control point in 3D object coordinates or 2D image coordinates. Figure 5.1a shows SEM images of point shaped circular nanomarkers, figure 5.1b shows ring shaped variants. Both types were fabricated by FIB milling (see chapter 4) with several selected radii, ranging from 100 nm to 500 nm (table 4.5.2).

5.1 COORDINATE DETERMINATION STRATEGY

The accuracy of a landmark or control point based calibration strategy depends largely on the accuracy of the determination of the coordinates of the landmarks from the measurement data. In order to prevent errors introduced by a manual selection of the object point or image coordinates, a strategy using digital image processing routines for the determination of the control point coordinates has been established and utilized. Figure 5.2 illustrates the strategy used for the determination of the object point and image coordinates applied to the calibration structures created by

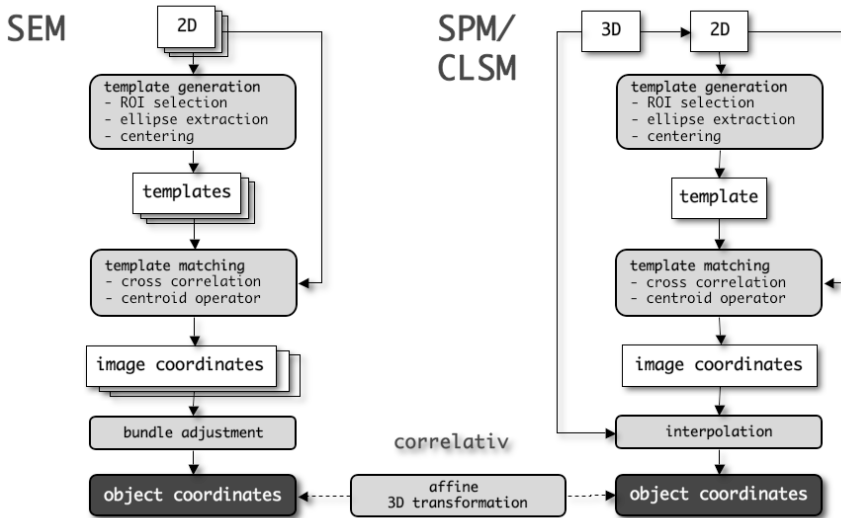


Figure 5.2: Strategy scheme for the determination of object point and image coordinates

FIB gas-induced metal deposition (fig. 4.3b).

Micro-range measurement data, obtained by either 2D or 3D microscopic methods, are mainly presented as images or can be transformed into images. A common representation of 3D data in images uses color or gray scale coding for the measured heights. Therefore, image processing methods can be applied to most measurement data, as, for example, correlation techniques based on template matching, a method that has been used preferentially here for the determination of the control point coordinates, if the marker in the image was represented by a minimum number of pixels. In certain cases, if 3D measurement data were available, and if the number of pixels representing the landmark in the image of the 3D data set was small or insufficient for accurate template matching, a simple and fast method based on the determination of the centroid of the selected nanomarker in the image was applied.

In order to be able to analyze the measurement data for calibration purposes, software using a graphical interface (GUI) has been developed. The processing of the microscopic images for coordinate determination with this software is done interactively, and can be performed in a semi-automatic or manual manner. The manual option allows the visual determination of the approximate location of single nanomarkers, which is often necessary, when a lot of noise or dirt is an issue in the recorded measurement data.

5.2 TEMPLATE MATCHING BY CORRELATION

An advantage to using a landmark-based strategy for calibration of micro-range measurement methods comes from the fact that the landmarks used are artificially generated, geometrical features that are well distributed on the calibration structure.

Moreover, they are also abundant and prominent, and, therefore, easily distinguishable from non-landmark areas in any measurement data or images.

5.2.1 Cross-correlation

Because all of the markers applied on the calibration structure have the same geometrical design, they will show similarities in the measurement or pixel values making up the feature in the image or measurement data. Such similarities can be statistically expressed as an amount of correlation between the characteristics X and Y of two entities A and B, e.g. the pixel values X of the landmark A and the pixel values Y of the landmark B. If there exists a linear coherency between X and Y , the similarity can be quantified by the use of the covariance σ_{XY} , a quantity defining the amount of dependency between the properties X and Y of A and B. Normalizing the covariance by the standard deviations σ_X and σ_Y of X and Y leads to the normalized correlation coefficient ρ [5.1]

$$\rho = \frac{\sigma_{XY}}{\sigma_X \cdot \sigma_Y}. \quad (5.1)$$

The correlation coefficient ρ results in a value between -1 to +1, in which 0 denotes no correlation, or stochastic independency. Values for ρ of 0.7 and higher usually define good correlation between A and B, in other words, a good similarity between the properties X and Y of the entities A and B.

Template matching uses the correlation method to detect similarities between a small template image $f(x, y)$ and an excerpt of the same size depicted from the target image $g(x, y)$ at a specific location. The similarity of two images is expressed by the normalized cross-correlation coefficient [5.1], written in discrete form [5.2]

$$\rho_c = \frac{\sum_{i=1}^n (f_i - \bar{f})(g_i - \bar{g})}{\sqrt{\sum_{i=1}^n (f_i - \bar{f})^2} \sqrt{\sum_{i=1}^n (g_i - \bar{g})^2}}, \quad (5.2)$$

in which g_i denotes the value of the pixel i of the target image excerpt, and f_i the value of the pixel i of the template image. \bar{f} and \bar{g} represent the mean of the pixel values of the template and the target image excerpt, respectively. In order to be able to detect a group of features in an image, the template image containing a copy of a feature from the target image or even a synthetically created feature, is moved pixel by pixel over the whole target image. At every pixel of the target image, an image excerpt with the same size as the template image is taken from the whole target image (fig. 5.3a), and the correlation coefficient ρ_c [5.2] is calculated. A map of the correlation factors results (fig. 5.3b). In the example given in figure 5.3, bright pixels indicate a high similarity between the template image and the target image excerpt, and, hence, a good approximation for the control point coordinates, provided that the landmark is in the center of the template, or its shift from the template center is known.

5.2.2 Subpixel coordinate determination

Cross correlation is a robust method independent of pixel contrast. The geometry of the feature to be searched is arbitrary. However, rotations, scale differences and

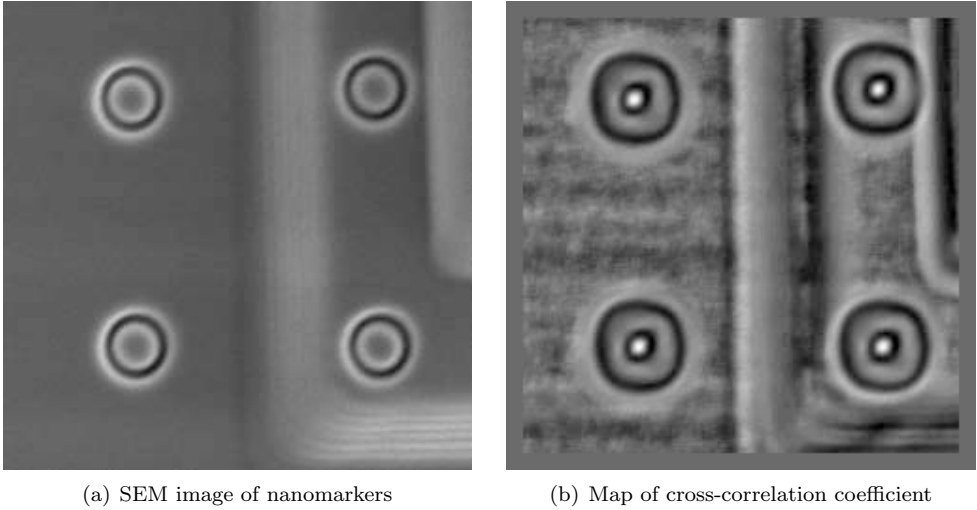


Figure 5.3: Cross-correlation method

distortions between the features in the template image and the target image excerpt are not considered and lead to a diminished correlation value. In addition, because discrete pixel positions are correlated by [5.2], the resulting correlation factor is only representative for one pixel of the target image. And, the center of the landmark in the template has to be congruent with the center pixel of the template or, alternatively, the shift from the center has to be known for accurate determination of the coordinates of the peaks in the image map of the cross-correlation factors (fig. 5.3b).

For many applications, coordinate determination of the center of the landmark with an accuracy of one pixel is not sufficient for calibration procedures. Also, for micro-range calibration purposes, sub-pixel accuracy is necessary for the calibration of microscopes. Various methods to achieve accurate sub-pixel accuracy are described in literature, as least-squares matching routines [Gruen 96] or structural methods for geometrical features, such as circle and ellipse fitting [Zhou 86]. These methods allow the determination of the center coordinate of a depicted feature with very high accuracy of up to 0.005 pixel under ideal conditions.

$$x_c = \frac{\sum_{i=1}^n (x_i \cdot \rho_c(x_i))}{\rho_c(x_i)}, \quad y_c = \frac{\sum_{i=1}^n (y_i \cdot \rho_c(y_i))}{\rho_c(y_i)} \quad (5.3)$$

In the presented work, the centroid method [5.3] has been chosen for sub-pixel control point coordinate determination. The centroid coordinates x_c and y_c represent the lateral coordinates of the center of gravity, calculated by the sum of the value of the correlation coefficient ρ_c [5.2] at the lateral pixel positions x_i and y_i of the target image, respectively. The method is easy-to-implement and sufficiently accurate, because the templates are chosen from within the target image itself and, therefore, no rotation and scale differences are to be expected. In addition, due to the circular geometry of the nanomarkers, the template matching results in a symmetrical distribution of the correlation coefficients after the matching process (fig. 5.3b). Hence, the center

coordinates of the symmetrically distributed local coefficients can be determined by calculating the centroid at each maximum of the correlation coefficient distribution of a distinct nanomarker. The theoretical accuracy of the centroid operator can be estimated according to [5.4] [Maas 92]

$$\begin{aligned}\sigma_{x_c} &= \frac{1}{\sum \rho_c(x_i)} \sqrt{\sum (x_i - x_c)^2} \cdot \sigma_{\rho_c} \\ \sigma_{y_c} &= \frac{1}{\sum \rho_c(y_i)} \sqrt{\sum (y_i - y_c)^2} \cdot \sigma_{\rho_c},\end{aligned}\quad (5.4)$$

in which σ_{ρ_c} represents the standard deviation of the correlation factors used for determining the centroid.

In practice, an accuracy of 0.03 to 0.05 pixel can be achieved [Luhmann 00], which corresponds to a uncertainty of 0.75 nm, supposing a 25 nm pixel size in a microscopic image.

5.2.3 Template centering and adjustment

One way of determining the center of a feature of circular shape involves the application of structural methods for geometrical features, such as circle and ellipse fitting [Zhou 86]. Usually, fitting is applied to each detected nanomarker. Here, a different strategy is followed, in order to be able to manually survey the template selection and the adjustment of the selected marker to the template center. Due to the use of homogeneous control points, an equal shape of the single landmark features is assumed for each measurement setup, be it a SEM image or a SPM measurement, for example. Hence, for every image or set of measurement data, one control point of the target image is selected interactively as the template image and used for the correlation process. All other control points detected by the measurement can be expected to be similarly recorded with respect to the chosen template, and therefore yield a high correlation factor. Template matching by cross-correlation of figure 5.3a, for example, results in correlation coefficients ranging from 0.917 to 1. In this example, the control point chosen for the template was the nanomarker on the lower left in this example.

Ellipse fitting

When using such an approach, however, it is important either to consider the position of the center of the chosen feature in the template image during the matching process, or to translate the coordinate center of the chosen template feature to the very center of the template image, as already mentioned, and illustrated in figure 5.4. In other words, the center pixel of the template and the coordinate center of the chosen feature must coincide. As the landmark features for the calibration process described here are represented by circular nanomarkers, a method for fitting circles could have been applied. However, the fact that the calibration object must be tilted for 3D SEM measurements has to be taken into consideration. Tilting, especially at high angles, transforms a circular feature into an ellipse, due to the projection in SEM imaging. Geometrically, central projection even causes the center of the circle to

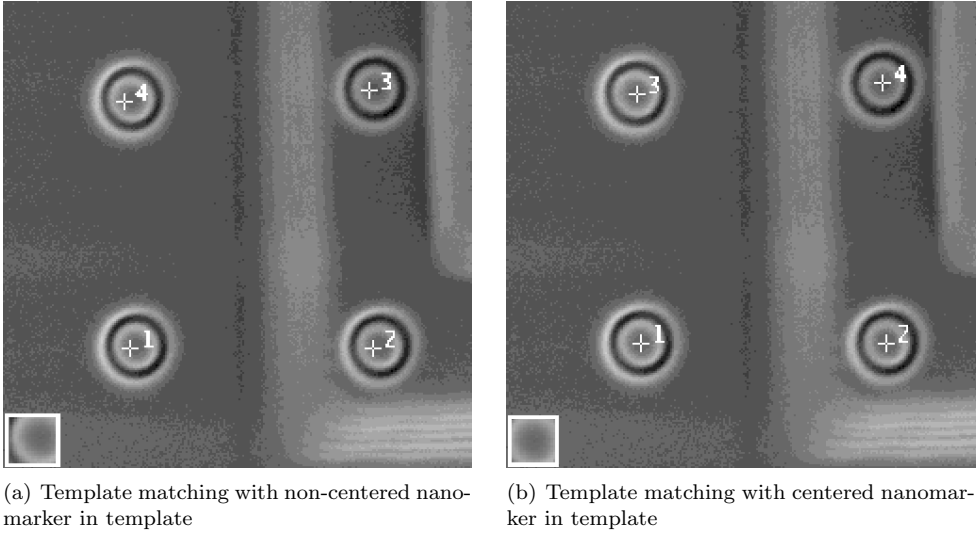


Figure 5.4: Template adjustment for accurate template matching

be non-identical to the center of the projected ellipse. Hence, for the determination of the coordinate center of the landmark, which is necessary to translate it to the template image center, a numerically stable direct least-squares fitting of ellipses [Halir 98] has been used. During the last few years, a number of methods have been proposed for ellipse fitting, among them Hough transforming [Yuen 89], Kalman filtering [Porrill 90], and others. One group of direct least-squares fitting methods was introduced by [Fitzgibbon 95]. It works with segmented data, so it is assumed that all data points belong to one ellipse. [Halir 98] improved the latter method to make it more robust for scattered and noisy data.

In general, an ellipse is a special case of a general conic section, which can be described as an implicit second order polynomial [5.5]

$$Q = ax^2 + bxy + cy^2 + dx + ey + f = 0. \quad (5.5)$$

The polynomial function Q is called the *algebraic distance* of a point (x, y) to the given general conic section, with the ellipse coefficients a to e as the parameters \mathbf{a} to be estimated, and the coordinates (x, y) of the ellipse as the observations \mathbf{x} , respectively [5.6]

$$Q_{\mathbf{a}}(\mathbf{x}) = \mathbf{x} \cdot \mathbf{a}. \quad (5.6)$$

The least-squares fitting of a general conic may therefore be solved by minimizing the sum of squared algebraic distances of the points to the conic represented by \mathbf{a} . But then, the result of the fitting remains a general conic section, which is not necessarily an ellipse. Therefore, an ellipse-specific equality constraint [5.9] is introduced [Fitzgibbon 96], so that the fitting problem can be formulated as [5.7]

$$\min_{\mathbf{a}} \|\mathbf{D}\mathbf{a}\| \quad (5.7)$$

in which the constraint [5.8]

$$\mathbf{a}^T \mathbf{C} \mathbf{a} = 1, \quad (5.8)$$

where \mathbf{D} is the design matrix carrying the observations, and \mathbf{C} is the constraint matrix carrying the ellipse specific equality constraint [5.9]

$$4ac - b^2 = 1. \quad (5.9)$$

Once the ellipse specific parameters of the conic section are known, the center of the ellipse (x_m, y_m) can be calculated from [5.10]

$$x_m : \frac{d}{2} + ax + \frac{b}{2}y = 0, \quad y_m : \frac{e}{2} + \frac{b}{2}x + cy = 0. \quad (5.10)$$

Edge detection

Another obstacle on the way to adjust the center of the template with the center of the control point that has been selected from the target image is the determination of the ellipse coordinates \mathbf{x} . For that purpose, the ellipse must be identified within the template image and its outline extracted.

Supposing that any geometrical feature in an ideal image is formed by pixel values of pixels representing that feature, and which are distinguishable from the neighboring pixel values of pixels not representing that feature, then the extraction of geometrical features in digital image processing equals the analysis of neighboring pixels. Such an analysis of neighboring pixels can be performed, e.g., by quantifying the gradient between neighboring pixels with the help of distinct filters or operators. In general, such procedures are known as feature extraction or edge detection. Edges in images can be characterized by gray values that change significantly perpendicular to the direction of the edge. Edges can also be characterized by direction and magnitude. They are formed by small features in the image, in other words, the area of significant changes in the pixel values must be within certain limits, and therefore, edges can be pronounced by high-pass filters [Luhmann 00].

Two approaches are commonly used to quantify the gradient of a function: either the first order, or the second order derivative of a function $f(x)$. The discrete form of the first and second derivatives of a 1D function is as follows [5.11]:

$$\begin{aligned} f'(x) &= f(x+1) - f(x) \\ f''(x) &= f(x+1) - 2f(x) + f(x-1), \end{aligned} \quad (5.11)$$

By calculating the first order derivative to the function $f(x)$, the position of edges is identified by local maxima of the derivative, whereas by calculating the second derivative, its point of inflection at zero crossings characterizes edge positions.

As an analogy, the gray values of an image can be regarded as a 2D function $f(x, y)$, the image function of the pixel coordinates. Filtering an image function with

a local, quadratic filter operator $g(x, y)$ of the size $(n \times n)$ is called *convolution* and is mathematically described in [5.12]

$$f(x, y) * g(x, y) = \sum_{i=-n}^n \sum_{j=-n}^n f(x-i, y-j) \cdot g(i, j). \quad (5.12)$$

By choosing appropriate local operators $g(x, y)$ for both image coordinate directions, the derivatives of the image function at given positions can be approximated. Local filters, such as the classical Sobel operator [5.13], use the discrete differentiation in order to approximate the first derivative of the image function

$$g_x = \begin{bmatrix} 1 & 2 & 1 \\ 0 & 0 & 0 \\ -1 & -2 & -1 \end{bmatrix} \quad g_y = \begin{bmatrix} 1 & 0 & -1 \\ 2 & 0 & -2 \\ 1 & 0 & -1 \end{bmatrix}, \quad (5.13)$$

whereas the Laplace [5.14] operator uses the second order derivative

$$g(x, y) = \begin{bmatrix} 0 & 1 & 0 \\ 1 & -4 & 1 \\ 0 & 1 & 0 \end{bmatrix}. \quad (5.14)$$

A more comprehensive and in-depth description of local filter operators and convolution is given in [Jähne 02].

Canny operator

Because local filter operators are highly sensitive to noise, small gradients can be mistakenly interpreted as edges. The more sophisticated Canny operator [Canny 86] first smooths the image by the first derivative of the normalized Gauss function in both directions

$$\begin{aligned} G_x(x, y) &= \frac{\delta G(x, y)}{\delta x} \\ G_y(x, y) &= \frac{\delta G(x, y)}{\delta y}, \end{aligned} \quad (5.15)$$

with the Gaussian function $G(x, y)$ being [5.16]

$$G(x, y) = \frac{1}{\sqrt{2\pi\sigma}} \cdot e^{-\frac{x^2+y^2}{2\sigma^2}}. \quad (5.16)$$

Then, the image can convoluted with the Gaussian derivatives in both directions [5.17]

$$\begin{aligned} f_x(x, y) &= \frac{\delta(f(x, y) * G(x, y))}{\delta x} = f(x, y) * G_x(x, y) \\ f_y(x, y) &= \frac{\delta(f(x, y) * G(x, y))}{\delta y} = f(x, y) * G_y(x, y). \end{aligned} \quad (5.17)$$

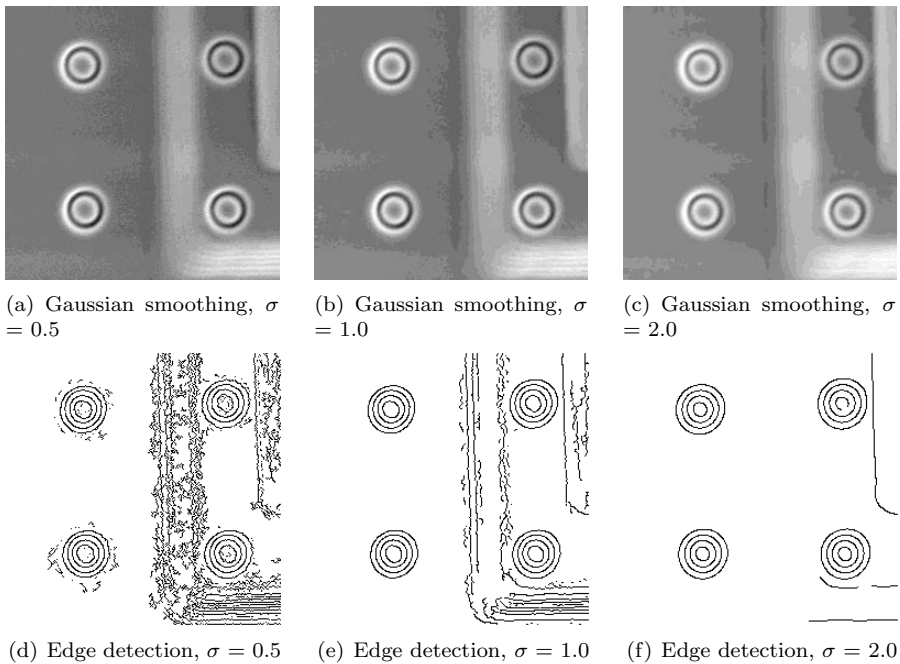
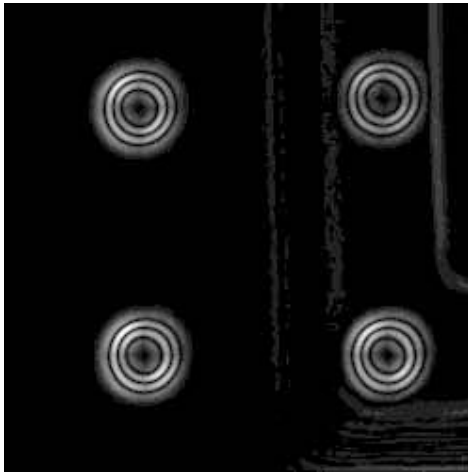


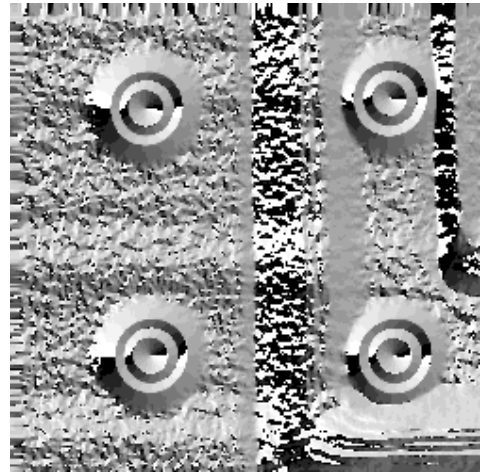
Figure 5.5: Gaussian smoothing influence on edge detection

The magnitude of smoothing can be adjusted, depending upon the noise in the image, by altering the standard deviation σ of the operator. A common range is $0.5 \leq \sigma \leq 3$ for filter sizes between 11 and 13 (figure 5.5). After the actual task of the Canny operator, the Canny algorithm involves several further steps in order to obtain a binary image of black edge pixels and white non-edge pixels. First, the pixels that represent an edge but at the same time lack maximum gradient magnitude, need to be identified by a search for local maxima. Each neighboring pixel of an initial pixel is analyzed for the magnitude of its gradient relative to the target pixel. If the magnitude of the gradient is greater than the magnitude of the initial pixel, and if the direction of the gradient is not equal to the direction of the initial pixel relative to the neighboring pixel with the higher gradient, then the algorithm defines the initial pixel as non-edge pixel. This routine is called non-maximum suppression (figure 5.6c) and involves knowledge of the gradient magnitudes (figure 5.6a) and the gradient direction (figure 5.6b). Second, the minimum value of the magnitude has to be determined that will characterize a pixel as an edge-pixel. Therefore, the histogram of the magnitude image is established and then used to compute hysteresis thresholds. In order to prevent the discontinuation of an edge due to fluctuations in the magnitude of the gradient, two hysteresis thresholds are used. All pixels carrying a gradient higher than the upper threshold will be instantly recognized as edge-pixels, and all pixels carrying a gradient lower than the lower threshold are judged as non-edge pixels. A pixel with intermediate gradient magnitude will only be defined as an edge-pixel, if at least one of its neighboring pixels is an edge-pixel, and if the direction

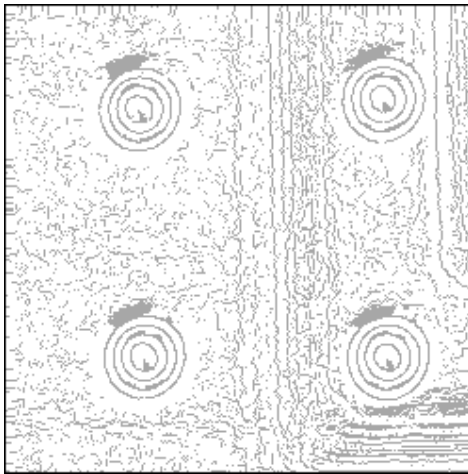
of the gradient of that edge-pixel has the same direction as the relative position of the two pixels to each other (fig. 5.6d).



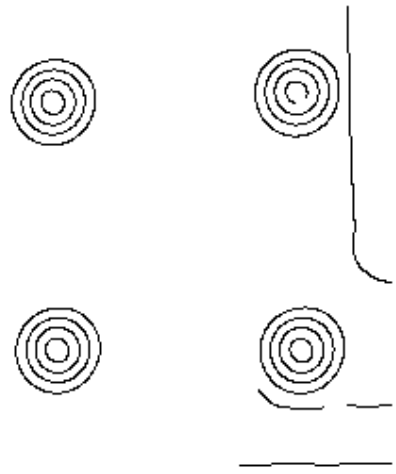
(a) Edge detection sub-routine: gradient magnitude



(b) Edge detection sub-routine: gradient direction



(c) Edge detection sub-routine, non-maxima suppression



(d) Edge detection sub-routine, line thinning

Figure 5.6: Canny algorithm sub-routines

The Canny algorithm offers stability against noise, high sensitivity of true edges, and accuracy of edge position determination [Luhmann 00]. The superiority of the Canny algorithm for edge detection has been mentioned [Dougherty 98], and its application to SEM images has been tested and characterized [Hemmler 01]. Therefore, the Canny algorithm was used for extraction of the outline of the ellipse in the template images for the determination of the needed ellipse coordinate observations. As mentioned, these observations can then be fitted by least-squares estimation [5.7] for

the calculation of the ellipse center [5.10] according to [Halir 98]. The algorithm has been implemented in a software package. An example of ellipse extraction and center coordinate detection for template adjustment is shown in figure 5.7.

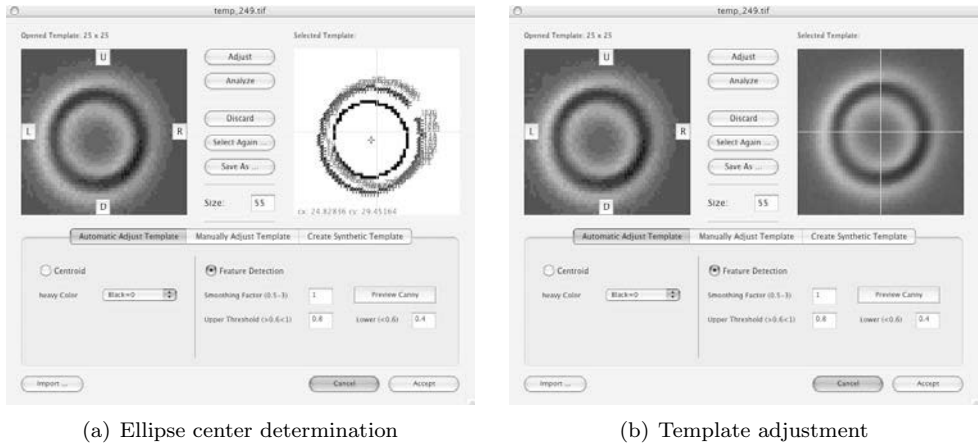


Figure 5.7: Template adjustment by ellipse fitting

5.3 COORDINATE ACCURACY IN SYNTHETIC DATA

Tests on synthetic images were performed in order to judge the accuracy of the control point coordinate determination methods described above. The most obvious obstacle to be expected in control point coordinate determination by template matching is random noise in the images or in the measurement, as well as physical dirt on the sample. Other difficulties arise from shifting measurement conditions during data sampling, as, for example, changes of image contrast and transformations of the geometrical shape of recorded structures in SEM images due to sample tilting. In the tests with synthetic images analyzed in this section, noise has been simulated by randomly applying pixel gray values with various Gaussian distributions to the target image in order to be able to characterize the influence of noise on the detection of the ellipse center for template adjustment, and to determine the mean point error $\bar{\zeta}_p$ of the control point coordinate determination with respect to the amount of noise applied to the test images.

5.3.1 Ellipse fitting accuracy

The ellipse fitting method by [Halir 98] applied here is used for centering the template image. This centering is achieved by laterally translating the mathematical center of the ellipse to the center of the template image. Because the positioning of the template feature to the center of the template is a translation by a discrete integer represented by a pixel, the method is virtually immune to noise, as can be recognized in figure 5.8. Even a deviation of the pixel gray values within 50 gray values ($\sigma_{noise}=50$) allows the appropriate ellipse center detection for template centering.

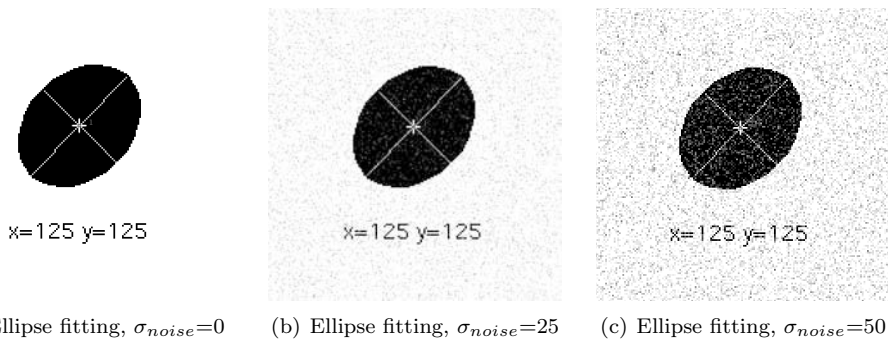


Figure 5.8: Ellipse fitting accuracy [Halir 98] in images with noise

Table 5.1: Mean point error $\bar{\zeta}_p$ of ellipse fitting in template images with noise

noise	x	y	$\bar{\zeta}_p$ [pixel]
$\sigma_{noise}=0$	124.928	124.944	0.091
$\sigma_{noise}=25$	124.958	124.886	0.122
$\sigma_{noise}=50$	124.795	124.828	0.268

5.3.2 Template matching accuracy

The template matching method of applying a normalized cross-correlation, and the subsequent subpixel determination of accuracy of the control point coordinates by calculating the centroid [5.3] of the feature in the image, is expected to be influenced by randomly distributed noise as well. Test images, again with various distribution of noise, have been created for both, the circle nanomarker and the ring nanomarker type of landmark, in order to estimate the accuracy of the template matching and control point determination procedure. The synthetic circle type nanomarker chosen for this test has a diameter of 5 pixels, the ring nanomarker type has a diameter of 11 pixels. Figure 5.9 shows an image example of each type of marker with $\sigma_{noise} = 10$ applied to the image. Two different methods have been applied, in order to determine the control point coordinates with subpixel accuracy by centroiding:

1. centroid determination of the gray values representing the marker in the target image (fig. 5.3a)
2. centroid determination of correlation coefficients maxima in the map of correlation coefficients ρ_c (fig. 5.3b)

Figure 5.10 shows the resulting mean point error of the determined control point coordinates introduced by various settings for noise (σ_{noise}) and by the two different centroid methods applied. Dashed-dotted lines and square symbols in figure 5.10

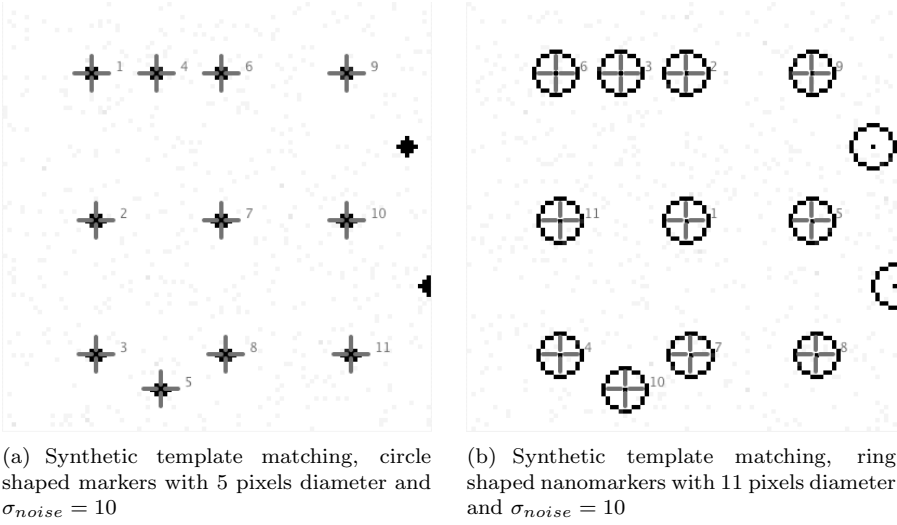


Figure 5.9: Synthetic images with circle and ring shaped markers

represent the results of the image centroid coordinates, and the dashed lines and round symbols represent the results of the correlation map centroid coordinates. Because the control point coordinates in the synthetic images are known (\tilde{x}, \tilde{y}) , the mean point error has been calculated according to [5.18]

$$\bar{\zeta}_p = \frac{1}{n} \sum_{i=1}^n \sqrt{(\tilde{x} - x_i)^2 + (\tilde{y} - y_i)^2}. \quad (5.18)$$

As can be seen in figure 5.10, and derived from the linear regression of the synthetic results in table 5.3.2, the determination of the control point coordinates by centroiding the correlation coefficients map is more accurate for the determination of the control point coordinates from the image gray values.

Table 5.2: Mean point error $\bar{\zeta}_p$ of centroid determination in image and correlation map

synthetic marker / centroid	image	correlation map
circle	$\bar{\zeta}_p = 0.0012 \cdot \sigma_{noise}$	$\bar{\zeta}_p = 0.0007 \cdot \sigma_{noise}$
ring	$\bar{\zeta}_p = 0.0011 \cdot \sigma_{noise}$	$\bar{\zeta}_p = 0.0009 \cdot \sigma_{noise}$

Due to their smaller size, the control point coordinates of the synthetic circle markers can be detected more accurately than the ring markers in very noisy data. However, in the experimental setup just described and at low noise $\sigma_{noise} \leq 10$, both centroid methods produce almost equally accurate results. At noise levels $\sigma_{noise} \gg 10$, the correlation centroid method is more resistant to noise than the image centroid

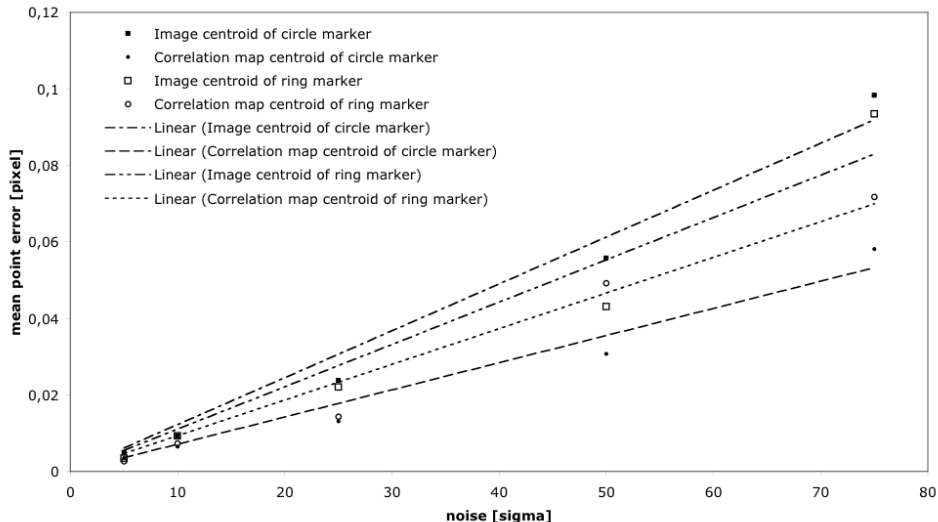


Figure 5.10: Accuracy of centroid determination of circle- and ring-shaped synthetic marker in image and in correlation map

method. In fact, the regression results of the image centroid method tend to lose their linear character at high noise and may be better described by a polynomial fitting.

It has already been mentioned that, for the control point determination routine used here, a template from every image or measurement is selected. In such an approach lies a certain risk, because the equal distribution and standard deviation of the noise applied in the target image can also be found in the template. In order to be able to predict the uncertainty of the control point coordinate determination of ring markers by noisy templates, a test has been performed using a synthetic target image with either, a synthetic 1 bit template containing no noise (dashed line), or a noisy template image excerpt (dotted line) of the target image (fig. 5.11). At low noise, the accuracy of both template strategies is almost equal; at high noise levels $\sigma_{noise} \gg 10$, the resulting mean point error when using a synthetic 1 bit template is significantly lower than the mean point error when using an extracted template.

5.4 COORDINATE ACCURACY IN REAL DATA

The mean point error $\bar{\zeta}_p$ of the coordinate determination in synthetic images at low noise ($\sigma_{noise} < 10$) is in the range of 0.01 pixel (figs. 5.10 and 5.11). This uncertainty equals 0.585 nm and 0.3125 nm in the example images with pixel sizes of 58.5 nm (fig. 5.12a) and 31.25 nm (fig. 5.12b), respectively. However, real measurement data strongly differ from the synthetic images. Therefore, several experiments on the measurements shown in figure 5.12 have been performed in order to be able to obtain the uncertainty of the template matching method in real images and measurements. Figure 5.12a shows an SEM image of a FIB fabricated calibration structure with ring nanomarkers. Figure 5.12b shows a SPM measurement of the same structure

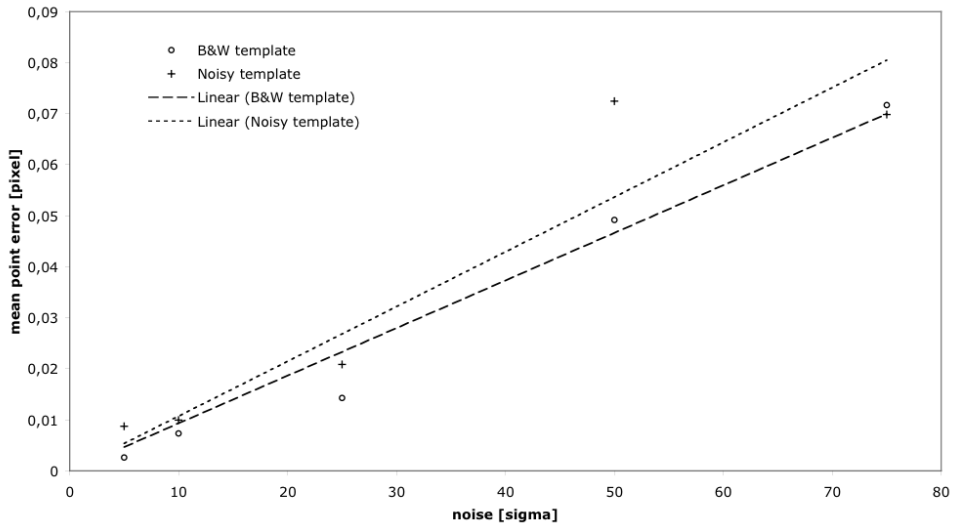


Figure 5.11: Centroid determination of ring shaped nanomarkers in correlation. Comparison of using an artificial 1 bit template to target image excerpt (noisy template)

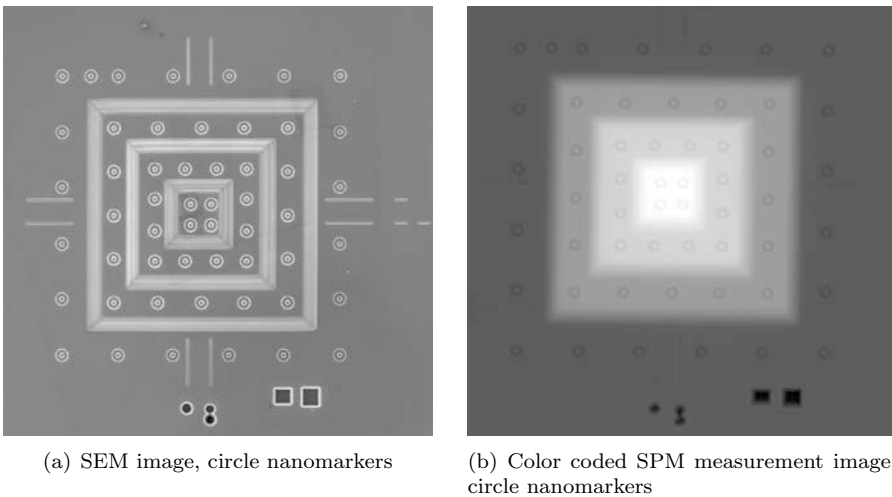


Figure 5.12: SEM image and SPM measurement of ring nanomarker calibration structure

representing 3D object coordinates, with the measured heights being color-coded by a LUT (look-up table) with 256 gray values. While in the SPM measurement highly similar ring shaped nanomarkers can be recognized, the nanomarkers in the SEM image appear to be more heterogeneous.

Several contrast-forming parameters influence image generation in the SEM. In particular, the relative orientation of the secondary electron detector to the specimen plane in general and when tilting the sample stage, as well as a secondary electron

generation varying with the chemical properties of the specimen, leads to variations in the recorded signal, and hence in the images. The latter effect can be observed in

Table 5.3: Mean correlation coefficient $\bar{\rho}_c$ in SEM and SPM data (fig. 5.12)

	SPM	SEM
$\bar{\rho}_c$	0.9784	0.8686
$\sigma_{\bar{\rho}_c}$	0.0084	0.0714

figure 5.12a: the marker at the very bottom around the structure are milled in silicon, whereas the substrate of the structure itself consists mostly of platinum. However, due to the properties of the cross-correlation algorithm applied, such a linear shift in the intensity of the gray values does not affect the matching process. But, if the specimen is tilted for 3D reconstruction or calibration purposes, the contrast and the local intensity distribution of the gray values representing the nanomarkers in the image with respect to each other change, as shown in figure 5.13 through a series of images of the above mentioned calibration structure (fig. 5.12a) at various sample tilts.

Because of the different measurement methods involved, the characterization of the uncertainty in landmark-based control point coordinate determination has been divided into two sections: the first section deals with the determination of the lateral uncertainty of the control point coordinates (image coordinates), and the second section deals with the determination of the uncertainty of the 3D control point coordinates (object coordinates) in 3D measurements.

5.4.1 Image coordinate determination

To evaluate the uncertainty of the control point coordinates represented by the virtual center of the markers, the template matching process has been analyzed using real measurement data. First, in order to characterize the influence of template selection in images at various sample tilts, as necessary for SEM photogrammetric calibration and SEM 3D reconstruction of sample surfaces, the relative mean point error of the image coordinate determination in tilted SEM images of the calibration structure shown in figure 5.12 has been estimated. Second, the relative mean point error of image coordinate determination by matching a variety of template excerpts to the target image from which they have been copied has been evaluated, in order to obtain the measurement uncertainty of the template matching method applied here.

Tilted SEM images

Figure 5.13 shows the experimental setup of a reference structure with ring-shaped nanomarkers, four times tilted in steps of four degrees. In one analysis, the image coordinates of the nanomarkers have been determined using a synthetically created,

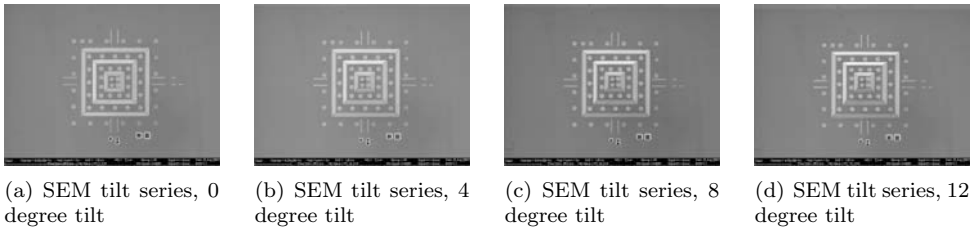


Figure 5.13: Tilt series of SEM images of ring nanomarker calibration structure

ring shaped template for all images even at various sample tilts (dashed line). In a second analysis, the image coordinates of the nanomarkers have been determined using a template excerpt from the image tilted to 0 degrees for all images, even at various sample tilts (dotted line). In a third analysis, the image coordinates have been determined using a template excerpt from each tilted image (straight line). Then, the

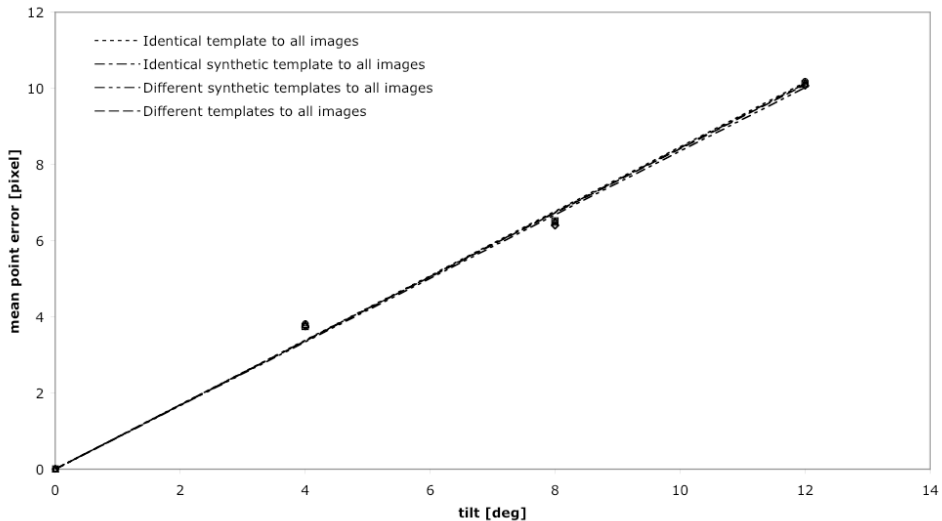


Figure 5.14: Relative mean point error of image coordinate determination in SEM images at various sample tilts

relative mean dislocation of the determined coordinates of each tilted image to the 0 degrees tilted image has been calculated, as shown in figure 5.14. For that purpose and in order to guarantee a correct analysis, the non-zero degrees tilted control point coordinates have been registered to the zero-degrees tilted control point coordinates, using a least-squares approximation with rigid transformation parameters. The results obtained are shown in figure 5.14, and reveal only a slight mean dislocation proportional to the tilt angle applied.

Varying templates

In contrast to the synthetic center coordinates, the true values of the measured nanomarker center coordinates are not known. Therefore, another approach was tested for calculating the mean point error of the experimentally determined coordinates in comparison to the use of synthetic data: $k = 11$ different templates out of the $n = 53$ landmarks were chosen in order to determine the control point coordinates of one image or measurement (fig. 5.12), respectively. First, the mean value of the control point coordinates i of every template matching process k was determined [5.19]

$$\bar{x}_i = \frac{1}{k} \sum_{j=1}^k x_{ij}, \quad \bar{y}_i = \frac{1}{k} \sum_{j=1}^k y_{ij}, \quad (5.19)$$

and selected as reference value to calculate the mean point error ζ_{pj}^- of each template j [5.20]

$$\zeta_{pj}^- = \frac{1}{n} \sum_{i=1}^n \sqrt{(\bar{x}_i - x_{ij})^2 + (\bar{y}_i - y_{ij})^2}. \quad (5.20)$$

The relative mean point error was then obtained by calculating the mean of ζ_{pj}^- as in [5.24]

$$\zeta_{rp}^- = \frac{1}{k} \sum_{j=1}^k \zeta_{pj}^-. \quad (5.21)$$

This exact procedure was repeated for several template sizes, in order to be able to characterize the effect of template size on the accuracy of control point determination. The results are summarized in figure 5.15 for SEM data, and in figure 5.16 for the lateral control point coordinate determination in the SPM data. The relative mean point error of the determined image coordinates in the SEM image is approximately 0.25 pixel (fig. 5.15), while the relative mean point error for the SPM lateral coordinates of the control points is approximately 0.20 pixel (fig. 5.16). This equals 18.28 nm for the SEM image coordinates and 6.24 nm for the SPM control point coordinates, respectively. As mentioned previously, the nanomarkers imaged by SEM appear more heterogeneous than the markers measured by SPM - hence, the better results in the correlation procedure. It can be seen that if using template matching for the control point coordinate determination in SEM images (fig. 5.15), the accuracy of the method is not dependent upon the size of the template, although there is a limit in diminishing the template size, which is, in this case, below 9 pixel (not shown). When the limit is exceeded, the pixel information making up the template is not sufficient and produces ambiguous results, and the method for adjusting the center of the nanomarker to the center of the template no longer works stably. In that case, a relative mean point error larger than 0.5 pixel can occur (not shown).

5.4.2 Object coordinate determination

From the SPM measurement data, the 3D object coordinates of the control points can be retrieved. After the lateral nanomarker coordinates (\bar{x}_i, \bar{y}_i) have been determined

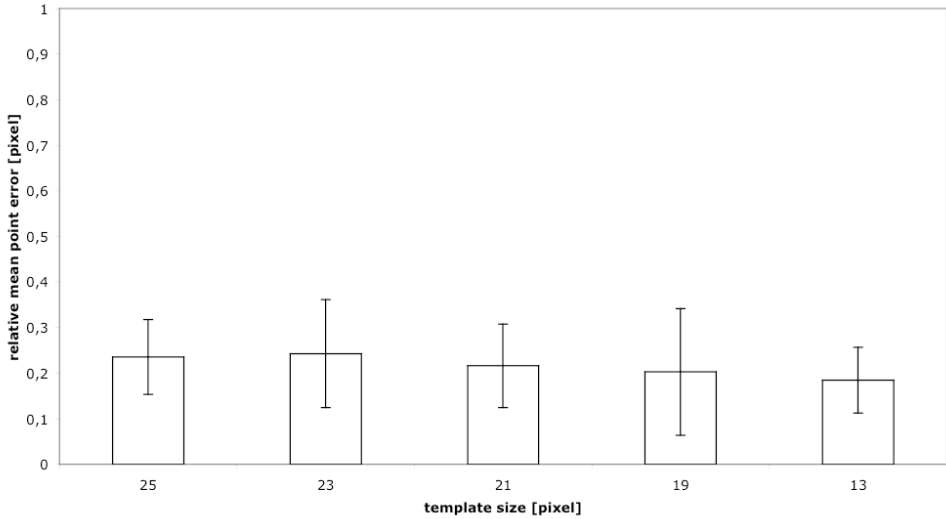


Figure 5.15: Relative mean point error of image coordinate determination with different templates in the same SEM image

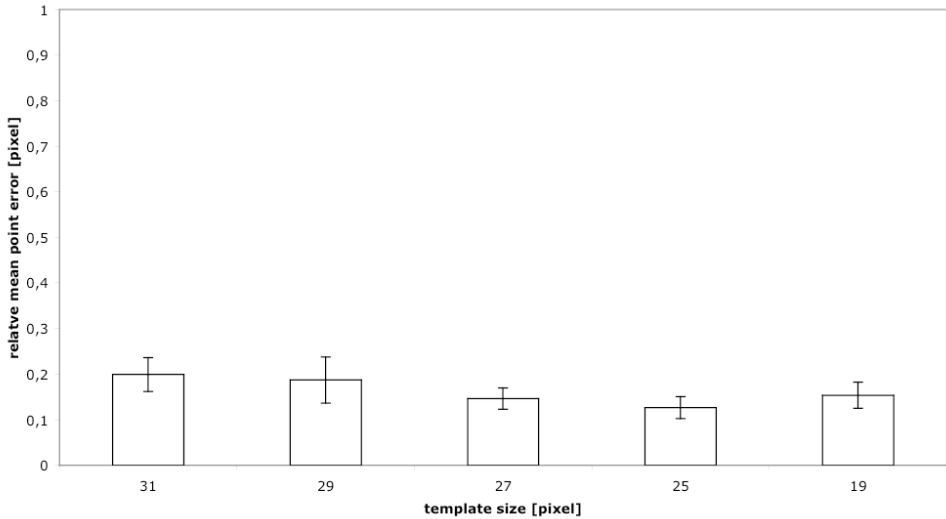


Figure 5.16: Relative mean point error of image coordinate determination with different templates in the same SPM measurement

by template matching in the color-coded image of the SPM measurement, the height \bar{z}_i corresponding to the coordinates is extracted from the measurement data. During the extraction, the pixel values are converted into metric units. In order to obtain an estimate of the accuracy of the height determination, and to consider noise and

structural irregularities, \bar{z}_i is averaged by the neighbor data points of (\bar{x}_i, \bar{y}_i)

$$\bar{z}_i = \frac{1}{9} \sum_{\bar{x}_i-1}^{\bar{x}_i+1} \sum_{\bar{y}_i-1}^{\bar{y}_i+1} z(\bar{x}_i, \bar{y}_i). \quad (5.22)$$

The standard deviation $\sigma_{\bar{z}_i}$ of the averaged value of \bar{z}_i is then used as an estimate of the accuracy of the determination of the height of the control point with the index i . The relative mean point error of the determined metric object coordinates can then be calculated, analogous to [5.20], for each template with the index j

$$\zeta_{pj}^- = \frac{1}{n} \sum_{i=1}^n \sqrt{(\bar{x}_i - x_{ij})^2 + (\bar{y}_i - y_{ij})^2 + \sigma_{\bar{z}_i}^2}. \quad (5.23)$$

The relative mean point error was again obtained by calculating the mean of ζ_{pj}^- as in [5.24]

$$\zeta_{rp}^- = \frac{1}{k} \sum_{j=1}^k \zeta_{pj}^-. \quad (5.24)$$

The relative mean point error in determining the object coordinates of the nanomarkers by SPM in the measurement shown in figure 5.12b is approximately 5 nm to 6 nm.

METROLOGY AND INDUSTRY APPLICATION

The ongoing miniaturization of tools and technology in life sciences and materials research, as well as in product development and quality assurance, requires measurement methods that can provide the accuracy demanded by this process and its applications. Within this chapter, several engineering and research applications of the landmark-based micro-range calibration method will be presented. First, relevant parameters of a prototype nano-positioning system and of a commercially available, highly sophisticated positioning stage have been characterized with SEM using photogrammetric self-calibration. Second, as an example for the future metrological application of the method in industrial and research measurement facilities, an XL30 FEG (FEI Company, USA) prototype SEM instrument has been calibrated, also using photogrammetric self-calibration and by applying the just mentioned prototype nano-positioning stage in combination with the 3D reference structure with landmarks. By the same method, an ESEM (FEI Company, USA) has been calibrated by photogrammetric means, for the first time, too. Third, the one-step calibration procedure pointed out in chapter 3 has been applied to SPM (Veeco, USA) using the 3D landmark-based reference structure, and compared to the classic calibration method using lateral and height pitch standards, as well as to CLSM. A Leica CLSM (Leica, Germany) has been calibrated by the same method using landmarks large enough to be resolved by the CLSM optics. Fourth, the various 3D micro-range measurement methods have been compared using correlative measurements, in other words, by various 3D microscopy methods that have been calibrated by the reference structure introduced in this work.

6.1 PHOTOGAMMETRIC CALIBRATION OF SEM

The aim of photogrammetric calibration of SEM instruments is the determination of SEM magnification (imaging scale) and the orientation data of the tilting stage. Because of the high demand for accuracy, the parameters of the image distortion and their effect on the measured coordinates should be determined, too. The estimated calibration parameters are the basis for all further photogrammetric coordinate measurements. In the case of using landmark-based reference structures, e.g., the pyramidal substructures as applied here, it is possible to process and evaluate calibration parameters and object coordinates in one step. This procedure, called photogrammetric self-calibration (see chapter 3), yields a high accuracy and allows an easy handling of specimen and positioning.

In order to avoid a given rank defect in the mathematical processing of the parameter estimation, when applying self-calibration, at a minimum the scale should be

set as a known parameter and have been obtained already by other measurements or measurement methods. That means that the scale is calculated directly from the scale bar in SEM images. Then, in the self-calibration process, only the orientation data and the object coordinates of the landmarks are estimated by the photogrammetric self-calibration. This is often not the desired solution, because it is the correction factor of the nominal SEM scale itself that usually must be determined. Yet, another approach to successfully perform the self-calibration is possible if at least two object point coordinates and the height information of a third coordinate, e.g., the landmarks, are known - for example, from a SPM measurement. The distance between the nanomarker coordinates is then automatically taken as reference scale when analyzing SEM data for self-calibration. For this reason, the reference structures and the object coordinates of the nanomarkers used within this thesis were all measured by SPM at the Physikalisch-Technische Bundesanstalt in Braunschweig.

Both cases - calibration and self-calibration - are implemented in the software packages Photo3D [Hemmler 01] and Pares3D [Sinram 02b] that were used in this work. As already mentioned in chapter 3, photogrammetric processing of the orientation parameters for the tilting stage is generally based on the calculation of six parameters for each image: three rotations and three translations. Because of parallel projection at magnifications higher than 500x, the number of degrees of freedom is reduced to five, due to the lack of the camera-constant parameter. However, additional parameters for estimating the magnification and image distortion are included in the software packages. It should be noted that at the present development state of the calibration software, approximate values for estimation parameters are necessary.

An obvious challenge in 3D scanning electron microscopy comes from the fact that the sensor cannot be moved and, hence, the object of interest has to be placed in various positions with respect to the sensor, in order to derive orientation parameters and 3D object coordinates by photogrammetric analysis. Obviously, the vacuum chamber is a limiting factor for the size of a positioning stage, as well as for the sample size. In order to be able to calibrate scanning electron microscopes, a positioning stage of appropriate size and yet with a highly reproducible tilting accuracy is required. Although almost all scanning electron microscopes are equipped with a built-in eucentric tilting stage, tests of a XL30 (FEI Company, Hillsboro, USA) 50 mm standard positioning stage revealed that tilting could not be performed in a reproducible manner, and that the tilting accuracy is worse than 1 degree (table 6.1). Furthermore, at higher magnifications, out-of-balance effects become evident during the tilting progress and do not allow the specimen to remain in the selected ROI, or within or close to the vector describing the tilt axis. Hence, the urgent need for a positioning stage of high accuracy, especially for tilt step repetition with only very small variances in the actual tilt angles of the single steps, in order to make possible the photogrammetric calibration of SEM over a broad range of magnifications by means of a landmark-based reference structure.

6.1.1 Characterization of positioning and tilting stages

The need to simulate different points of view in order to derive 3D coordinates and orientation parameters has already been mentioned. To fulfill this requirement, the sample has to be tilted along at least one rotation axis in order to allow views from different positions. However, rotating the specimen or the positioning stage, respectively, may result in a translation motion, if the area of interest is not positioned within the eucentric axis, as shown in figure 6.1. One negative effect of non-eucentric rotation is the specimen leaving the depth of field (DOF) or the ROI, as shown in figure 6.1a and b, respectively. By rotating along the eucentric axis (fig. 6.1c) such translational movements are minimized, and an identical scale factor can be assumed for all images involved, as the distance of the sample to the virtual center of projection remains constant. Because the built-in stages could not be used for

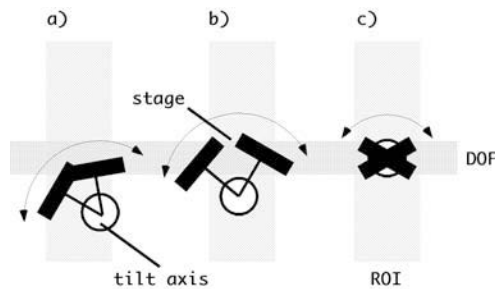
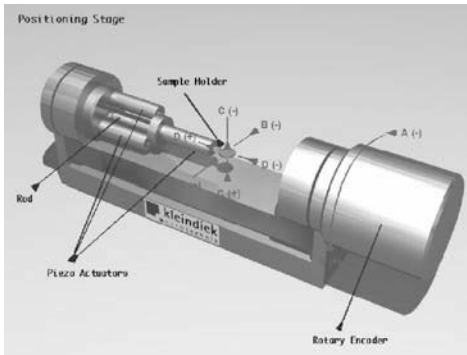


Figure 6.1: Importance of eucentric tilting in photogrammetric 3D SEM

a comprehensive calibration of several SEM instruments, a way had to be found to very accurately move the sample and to tilt it around the eucentric axis. Therefore, a special positioning tilting table was designed to reliably move the sample into the desired position, as depicted in figure 6.1c, even at magnifications higher than 10000x. Together with Kleindiek Nanotechnik (Reutlingen, Germany) a prototype stage has been developed: a nano-positioning tool with high accuracy and tilt step repeatability (fig. 6.2a). The prototype has been built by Kleindiek Nanotechnik and is depicted in figure 6.2b, together with a 10 euro cent coin for scale. The Kleindiek positioning tool consists of three patented piezo linear actuators (“Nanomotoren”) responsible for the translation movements (B, C, D) of the specimen, and an incremental rotary encoder with 3600 software steps (A) that are interpolated results of 2000 hardware tilt steps. The specimen holder consists of a TEM grid holder, so all standard TEM grids (3.05 mm) can be mounted. It was the volume of the microscope’s vacuum chamber that limited the design of the tilting table. Also, special care had to be taken with the components in order to prevent unwanted influence from the electron-optical imaging system of the SEM, and to maintain vacuum-stability and operability of the nano-positioning stage. For development and realization of the positioning tool, the vacuum chamber of the XL30 ESEM instrument available was measured, and the data were sampled and modeled in a CAD system (Strata, St. George UT, USA). Using the 3D CAD simulation, the main parameters determining the design of the



(a) CAD model of nanopositioning stage



(b) Nanopositioning stage on SEM stage

Figure 6.2: Kleindiek nanopositioning stage

stage could be made out and integrated in the prototype development. Due to the careful design, the Kleindiek nano-positioning tool can be attached to a variety of scanning electron microscopes; however, its design is optimized for the FEI XL30 and Quanta series (FEI Company, Hillsboro, USA) regular specimen chambers. With the help of the nano-positioning stage, any operator of the microscope is able to move the area of interest interactively to the desired position. However, despite the accuracy and reliability of the positioning table, the eucentric positioning remains an iterative process requiring some effort and practice.

Accuracy of the Kleindiek nano-positioning stage

Accurate 3D surface reconstruction of SEM data by means of stereo photogrammetry requires accurate knowledge of the relative tilt positions of the specimen with respect to the sensor. Hence, the key parameter of any positioning stage that needed

Table 6.1: Relative tilt accuracy of Kleindiek nanopositioning-tool by photogrammetric self-calibration

relative nominal tilt angle [deg]	5	10	20	30
measurements (n)	33	12	14	14
mean measured tilt angle [deg]	4.958	9.862	19.843	29.755
mean deviation in tilt angle [deg]	0.330	0.268	0.233	0.416
tilt angle correction factor	0.992	0.986	0.992	0.992
correction factor uncertainty	± 0.066	± 0.027	± 0.011	± 0.014

to be characterized is the accuracy of repeatability of the relative tilting, rather than observation of the deviation from absolute positioning. The Kleindiek nano-positioning tool described above cannot be moved to absolute positions, but it has

been designed to allow relative tilting with accurate repeatability. In order to characterize the remaining uncertainty of tilting at various tilt steps sizes, the method of photogrammetric self-calibration with a known reference structure has been utilized. For that purpose, the Kleindiek stage was introduced to an XL30 field emission gun (FEG) SEM, and the array A2 (fig. 4.6), made by FIB gas-induced metal deposition, was attached to a TEM grid and mounted on the sample holder of the stage. A variety of calibration measurements have been performed in order to characterize the repeatability and mean accuracy of tilt steps of different size produced by the positioning tool. In order to operate within the limits of tenable expenditure, four frequently used tilt-step magnitudes were chosen and repeatedly addressed, at which point the reference structure was imaged every time. From the data, the image control points (nanomarkers) have been determined and analyzed by photogrammetric self-calibration, as shown in table 6.1. Although the 0.1 degrees mean deviation in the repeated tilt steps the tool was designed for could not be verified, the mean tilt error remains well below 0.5 degrees, which is a significant improvement over the built-in sample stage as already described. The incremental rotation motor seems to work best at nominal tilt steps of 10 and 20 degrees, when the mean deviation is lowest, but still approximately 0.23 degrees. However, only with this specially de-

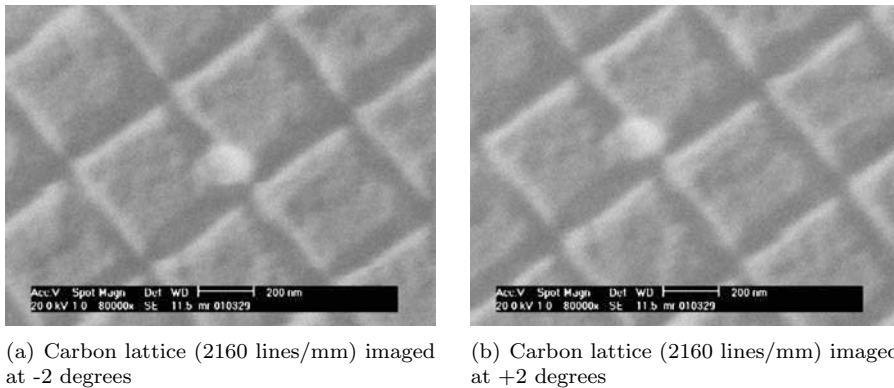


Figure 6.3: Nanostage stability at high magnifications (scale bar = 200 nm)

signed hardware could the calibration of SEM at magnifications greater than 6000x be accomplished. This calibration could be realized for two reasons. First, because of the accuracy of the positioning tool. Second, the stage design bears a stable and accurate positioning mechanism that allows effective eucentric tilting without large sample translation: a necessary prerequisite that allows imaging for the purpose of calibration and for 3D reconstruction at high magnifications.

An example of the stability of the stage is given in figure 6.3, where, for demonstration purposes, a carbon lattice has been imaged by an XL30 SEM instrument equipped with LaB₆ cathode at a magnification of approximately 80000x. The tilt axis in this example corresponds to the y-axis of the image. The relative tilting of 4 degrees shown in figure 6.3 causes a horizontal lateral translation of the ROI of 200 nm and a vertical lateral translation of 80 nm. These measured distances correspond to approximately 0.10 of the horizontal field of view and 0.07 of the vertical field

of view, respectively. Hence, two thirds of the imaged area of the two tilted images is identical and could be used for photogrammetric analysis. Although eucentric adjustment at high magnifications as used here is tricky, the positioning stage was routinely applied to photogrammetric calibration of SEM performed at magnifications of 20000x and above, and is therefore also suitable for the photogrammetric 3D reconstruction of very small structural details.

Accuracy of the Nova DualBeam stage

At a more evolved stage of this project and due to a cooperation with FEI Company (FEI European Headquarter, Eindhoven, the Netherlands) it was possible to work with the sample stage of a Nova DualBeam NanoLab prototype. As noted (see chapter 4), the DualBeam is a combination of SEM and FIB, offering both imaging by electron beam and nano-fabrication by ion-beam application. The DualBeam devices are serially equipped with rather sophisticated tilt stages, because of the relative orientation of the electron column to the ion column, which is 52 degrees. This specific Nova DualBeam, however, was equipped with an up-to-date sample stage capable of eucentric rotating and tilting for high precision sample positioning. The stage could be controlled directly from the graphical user interface (GUI) of

Table 6.2: Repetition accuracy of DualBeam by photogrammetric self-calibration

position	nom. tilt [deg]	nom. rotation [deg]	tilt [deg]	rotation [deg]
1	-10	0	9.247 ± 0.042	1.628 ± 0.010
2	-5	0	4.398 ± 0.016	1.598 ± 0.018
3	0	0	-0.522 ± 0.060	1.572 ± 0.018
4	5	0	-5.365 ± 0.028	1.558 ± 0.016
5	10	0	-10.279 ± 0.020	1.536 ± 0.008
6	15	0	-15.245 ± 0.004	1.507 ± 0.006
7	-10	90	10.311 ± 0.000	91.691 ± 0.006
8	-5	90	5.395 ± 0.035	91.630 ± 0.001
9	0	90	0.393 ± 0.000	91.594 ± 0.005
10	5	90	-4.529 ± 0.032	91.538 ± 0.008
11	10	90	-9.476 ± 0.032	91.506 ± 0.000
12	15	90	-14.519 ± 0.038	91.453 ± 0.009

the Nova, where absolute as well as relative tilt angles, rotations, and positions can be entered for moving the stage. The accuracy of tilting and rotating was analyzed with the reference structure F04 (fig. 4.6), an array of pyramidal structures with point-shaped nanomarkers as control points. The reference structure was mounted on the Nova sample holder and imaged by a series of 12 positions of varying tilt and rotation. Each of the 12 positions was addressed several times for a better stability when analyzing the image coordinates of the nanomarkers by photogrammetric

self-calibration, and for statistical evaluation of the mean tilt repetition error. The positioning was performed in the Nova as described, and the results were recorded using the electron beam imaging option at 5 kV, a working distance of 5 mm, and a horizontal field width of 16 μm , corresponding to a magnification of 8000x with respect to the Nova screen. Photogrammetric self-calibration was performed in order to determine the orientation of the images. To allow for optical imperfection, two distortion parameters were accounted for [3.20]. For the calculation shown in table 6.2, the scale factor of the SEM itself was used, whereas table 6.3 summarizes the most relevant settings of the photogrammetric self-calibration, including distortion parameters with the application of the scale factor from SPM measurements of the F04 array. The important numbers are expressed at the bottom of table 6.3. The

Table 6.3: Relative tilt accuracy of the Nova built-in sample stage by photogrammetric self-calibration

scale factor applied	SPM	SEM
calibration parameters	+ distortions	+ distortions
analyzed tilt steps	30	30
programmed stage positions	12	12
repetitions per position	2-4	2-4
mean deviation of mean tilt repetition error	0.0112	0.0280
mean deviation of mean rotation repetition error	0.0932	0.0894

mean deviation of mean tilt repetition error and the mean deviation of the mean rotation repetition error describe the remaining uncertainty of tilting or rotating, after having calibrated the error of a nominal setting and its actual tilt or rotation response. From table 6.2, one can extract the deviation in tilt-step repetition, say if tilting from minus 10 degrees to minus 5 degrees without rotating at rotation position 0 degrees, as 0.042 and 0.016 degrees. This corresponds to an uncertainty of 0.045. Taking the mean value of all uncertainties, the mean deviation of mean error of repetition when rotating or tilting the stage can be calculated, as shown in the bottom lines of table 6.3.

It can also be seen in table 6.3 that the mean deviation of the tilt repetition, if applying the SPM scale factor, is approximately half the mean deviation if applying the scale factor extracted from the SEM images. However, the deviation of the rotation repetition amounts to approximately the same value for both assets and is extremely low (below 0.1 degrees).

Comparison of regular tilt stage and prototype

The relevant characteristics of the microscope sample stages that were collected and applied within this thesis are summarized in table 6.4. When starting the project, it quickly became clear that the built-in stages of the XL30 series could not be used for photogrammetric analysis of SEM data, because a stable repeatability of tilting and

Table 6.4: Main characteristics of the relevant nano-positioning stages

device	XL30	Kleindiek	Nova
rotation			
rotation range [deg]	360	n. a.	360
rotation accuracy [deg]	$\approx \pm 3$	n. a.	± 0.09
tilting			
max. tilting [deg]	+75 to -15	± 70	+75 to -15
tilting accuracy [deg]	$\approx \pm 2$	$\pm 0.2 - 0.4$	± 0.03
positioning			
lateral accuracy [nm]	≈ 50	≤ 5	≤ 10
vertical accuracy [nm]	≈ 10000	≤ 5	≈ 50
application range			
working distance [mm]	10 (eucentric)	15 - 7	5 (eucentric)
max. magnification [x]	6000	80000	n.a.
specimen			
max. diameter [mm]	≈ 20	3	≈ 20
max. height [mm]	≈ 10	≈ 1	≈ 10

z positioning could not be guaranteed. The development of a special, high precision positioning tool was urgent, but had to be designed with one tilt axis only, due to limited funding. At that time, of course, the device was outstanding. However, positioning stages with all degrees of freedom necessary, and designed for highly accurate repeatable positioning, have meanwhile become commercially offered and available as an additional option to any SEM basic equipment.

6.1.2 Full SEM calibration

The accurate 3D reconstruction of SEM data by photogrammetric means requires predictable positioning, as already described, as well as calibrated instruments in terms of scaling errors and of imaging errors due to the influence of distortions, respectively. In order to demonstrate the landmark-based method, the scale factors of an XL30 FEG were determined over a broad range of magnifications by means of photogrammetric self-calibration with the reference structure array A2 (fig. 4.6).

Extensive scale factor calibration

Prior to the calibration process, the XL30 FEG was prepared for the installation of the Kleindiek nanostage (fig. 6.2). The array A2, deposited on a small piece of silicon wafer with a diameter of 2 mm, was mounted on a TEM grid and adjusted to the specimen holder of the Kleindiek stage. For all of the calibration measure-

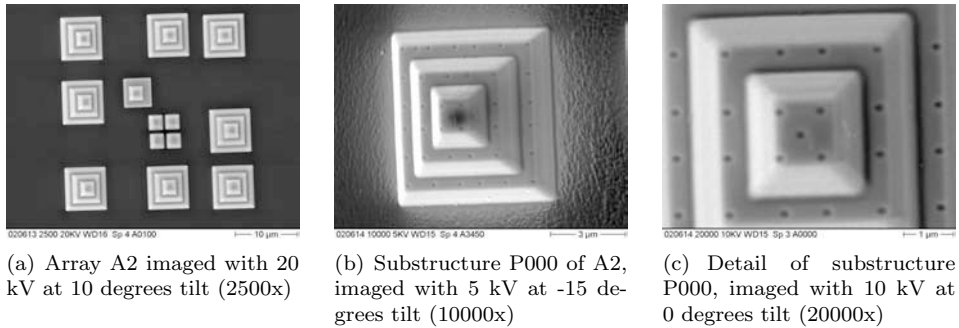


Figure 6.4: XL30 FEG calibration with Kleindiek positioning stage and reference structure A2

Table 6.5: XL30 FEG settings for a full self-calibration

nominal scale factor	spot size	5kV	10kV	20kV
0.017 (2000 x)	4	-	++	++
0.0212 (2500 x)	4	++	++	++
0.04083 (4800 x)	4	-	++	++
0.0425 (5000 x)	4	++	++	++
0.085 (10000 x)	4	++	++	++
0.17 (20000 x)	4	++	++	+
0.34 (40000 x)	3	+	+	+

ments, certain procedures were followed, in order to guarantee identical, stable and reproducible conditions:

1. when switching on the high tension of the electron beam, a minimum time of 15 minutes was given to the system to gain stable conditions for imaging;
2. the Kleindiek nano-positioning stage holder was brought to a reference position, determined by live imaging;
3. the incremental rotary motor of the positioning stage was reset by a predefined sequence of control movements.

In order to be able to calibrate the SEM instrument for daily routine work, a set of relevant parameters was chosen for imaging (fig. 6.5). The parameters chosen for the photogrammetric calibration are listed in table 6.5. Each single calibration procedure was performed using the described parameter settings for the SEM instrument, and by imaging the reference structure 10 times at tilt steps of 5 degrees, starting from 0 degrees to -20 degrees, then from +5 degrees to +20 degrees and returning to zero. For almost all of the settings, the self-calibration was used to determine the actual scale factor (indicated in table 6.5 by a “+” or a “++”) of the SEM device, for which purpose the SPM measured scale of the array A2 was used as reference.

In most of the settings, the self-calibration included the determination of distortion factors in the SEM images (indicated with a “++” in table 6.5) as well. From the

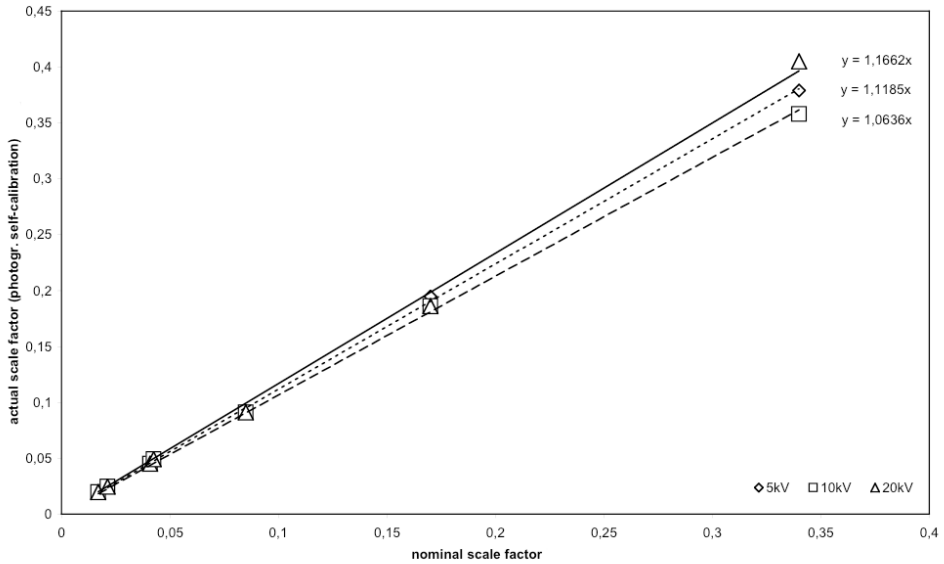


Figure 6.5: XL30 FEG scale factor calibration at broad magnification range

34 measurements, the control points of the 340 single images were determined and put together in a way so that a linear correction of the nominal scale factor could be calculated. In figure 6.5, the linear correction terms for the scale factor are shown. Those linearization data were retrieved from XL30 FEG self-calibration data without considering distortion factors. The complete linear correction terms, including those taking into account the radial and tangential distortion, are summarized in table 6.6. The best correspondence of the nominal scale factor to the actual scale is obtained at a 10 kV acceleration voltage of the electron beam. For that parameter, distortions have almost no impact on the linear correction. However, for 5 kV and 20 kV settings, the photogrammetric self-calibration results in up to 5% deviation in correction factors, when tangential and lateral distortion were considered within the parameter estimation. An additional result that can be retrieved from the pho-

Table 6.6: Linear scale correction with and without distortion parameters

linear scale correction	5kV	10kV	20kV
without distortions	1.119x	1.064x	1.166x
with distortions (r_1, r_2)	1.160x	1.063x	1.104x

togrammetric self-calibration is the standard deviation of the determination of the scale factor: the mean deviation in determining the scale factor by self-calibration without distortion is $6.72 \cdot 10^{-4}$, whereas the mean deviation of the scale factors determined by self-calibration with taking distortions into account is $1.00 \cdot 10^{-3}$.

Optical stability of SEM

It is one part of an integral device calibration to determine the actual parameters, such as the scale-factor, for various settings. Another important factor relevant to the applicability of the chosen measurement device is the stability of the system at the given settings over a certain time scale. In order to characterize the stability of the XL30 FEG SEM device, a depicted scale-factor was determined within two measurement slots with a given pitch of approximately a quarter of a year. The self-calibration was performed at nominal magnification of 10000x, with an acceleration voltage of 20 kV and a spot size of 4. For each self-calibration setup, the identical process with 10 tilt steps of 5 degrees, as described previously, was chosen. The results are summarized in table 6.6; obvious outliers were not eliminated. Within 90 days, the actual scale factor rose from 0.0913 to 0.0914, corresponding to a change of 0.2 %. Extrapolating this rise of the actual scale factor to a whole year, it is reasonable to expect a change of approximately 1 %.

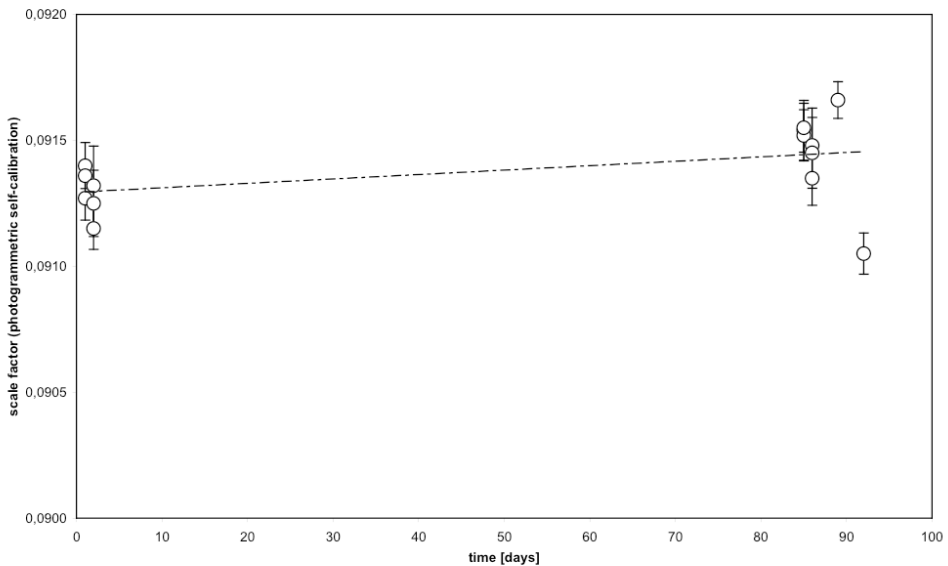


Figure 6.6: XL30 FEG scale factor stability over 90 days

6.1.3 Calibration of XL30 ESEM

The XL30 LaB₆ ESEM (FEI Company, Hillsboro, USA) is a combinatorial-device with the option for regular SEM imaging at high vacuum (HIVAC mode) conditions. However, it is also equipped with a differential pumping system and special gaseous secondary electron detectors, in order to allow imaging under water vapor or gaseous atmospheres (ESEM mode) up to approximately 40 mbar in its sample chamber (see chapter 2). The most relevant effect of using this technique is a simplified sample preparation process. The simplification is due both to the differential vacuum system, which allows aqueous samples in the sample chamber without affecting the high vacuum requirements of the electron column, and to no longer needing to metal-coat of the specimen in order to prevent electric charging of the specimen. Because the

Table 6.7: XL30 LaB₆ calibration at high vacuum (HIVAC) and high pressure (ESEM) conditions

	high vacuum mode (HIVAC)	high pressure mode (ESEM)
scale (self-calibration)	0.113	0.113
scale (calibration)	0.112	0.113
r_1	$7.600 \cdot 10^{-8}$	$5.838 \cdot 10^{-8}$
r_2	$1.827 \cdot 10^{-7}$	$1.950 \cdot 10^{-7}$

device uses the scanning system to image a specimen, in a variety of environments and with various detectors, it was the aim to estimate the influence of the latter two parameters on the resulting data. Again, the Kleindiek nano-positioning stage and a substructure of the reference array A2 were used for calibrating the microscope in both the high-vacuum and the high-pressure mode. Identical beam settings were chosen (20 kV acceleration voltage), however, to be able to cope with the relatively high magnification selected in the high-pressure mode, different spot sizes had to be adjusted for imaging. The reference scale was taken from SPM measurements of the substructure of the reference array. The results of the calibration and of the self-calibration, including distortion parameter estimation, are summarized in table 6.7. The results indicate that the device is very well adjusted for both imaging modes, because the determined scale factors, - at least for the chosen settings of the calibration - are identical. Also, eventual distortions that might have been expected if measuring with the gaseous secondary electron detector (GSED) of the ESEM mode are of similar value to the distortions arising under high-vacuum conditions. This is the first time, an SEM has been calibrated by photogrammetric means in high-pressure mode, and the method appears to be suitable for such a task. The result is not completely surprising, as the GSED is an event-sensitive detector, like the regular secondary electron detector. However, the GSE detector is situated normal to, that is, on top of, the specimen, instead of being attached at an angle, as with the classic Everhart-Thornley SE detector.

6.2 ONE-STEP 3D CALIBRATION

In the previous section, the usefulness of a landmark-based micro-range reference structure for the photogrammetric calibration of SEM has been demonstrated. Photogrammetry in combination with SEM is a powerful measurement tool, but still an underestimated and rather exotic 3D measurement method. At least, such is the status of the method for application in the micro-range, though industrially and commercially the method - in combination with light-optical sensors - is common for close-range applications, such as cultural heritage reconstruction, failure analysis of industrial products, quality assurance, and so on. It is also a wide-spread method for remote sensing. In the micro-range, however, photogrammetric 3D analysis and object reconstruction has to compete with powerful measurement methods like scanning probe microscopy (SPM), confocal laser scanning microscopy (CLSM), interference microscopy, and various others.

The concept based on calibration using control points with known 3D coordinates instead of pitch features, however, is much more comprehensive than just to be applied to photogrammetric analysis of SEM data. As already theoretically presented in chapter 3, using landmark-based 3D reference structures for micro-range measurements can be an alternative to pitch feature calibration procedures, and would allow a simpler handling of the calibration routine at specific settings, with only one calibration measurement involved. In the following, the landmark-based calibration procedure is applied to both SPM and CLSM. In the case of the SPM application, the landmark-based routine presented here is compared to the classic, pitch feature and step height calibration routine, as regularly applied for the calibration of scanning devices up to now.

6.2.1 SPM 3D calibration

The main reason to apply a new calibration method to SPM is not simply to switch from pitch-featured reference structures to landmark-based ones. Rather, there is also, in general, more effort involved in using two calibration structures, one 2D lattice for the lateral calibration measurement and one 1D step height structure to the vertical calibration measurement.

Using, for example, two structures for the determination of the scale factors of the 3 dimensions to be calibrated, implies first and foremost a decoupling of the lateral from the vertical dimension, a situation that does not exist at the time of the measurement itself. Also, the complete calibration is usually a mixture of histogram analysis combined with linear regression for characterizing the vertical scale, and an affine parameter estimation for the lateral scales and affine factors [Jorgensen 98]. Finally, although only a lateral coupling has been introduced to the one-step calibration parameter estimation routine applied in this specific case, the model could easily be enhanced by considering more coupling factors, whereas such an alteration is not possible for the two-step calibration routine.

In order to test the one-step 3D calibration model on SPM measurement, the reference array A2, whose control point object coordinates were already determined by a PTB measurement with the SiS-Nanostation SPM, was used again. For com-

parison, the same array was measured with a Veeco Explorer SPM (Veeco, USA). Immediately after measuring the A2 reference array, the Veeco device was calibrated by measuring the MicroMash (μ Mash, Estonia) TGX 01 reference structure consisting of a lattice with 3 μm pitch, and the step height reference structure TGZ 04 fabricated by the same company, which consists of 1D steps of 1 μm in height. For all measurements, the scan area selected for the Veeco instrument was 50 μm , and the scan speed was set to 1 second per scan line, totaling to a measurement time of 2000 seconds. The number of measurement points per line was set to 1000, resulting in a pixel size of 50 nm. In addition, 3D calibration parameter estimations, one including

Table 6.8: SPM one-step calibration by parameter estimation

number of estimated parameters	9	10	10	10
observations	228	228	228	228
scale correction factor c_x	1.162	1.163	1.163	1.163
scale correction factor c_y	1.293	1.293	1.293	1.292
scale correction factor c_z	1.269	1.269	1.269	1.271
coupling correction factor c_{xy}	-	-0.003	-	-
coupling correction factor c_{xz}	-	-	0.006	-
coupling correction factor c_{yz}	-	-	-	-0.045
mean point error $\bar{\zeta}_p$ [nm]	63 .0	59.6	60.2	58.1

lateral coupling, and one not considering the coupling, were performed using the raw Veeco measurement data being transformed to the center coordinates measured by the SiS Nanostation SPM. The results are shown in table 6.8. The estimated parameters, three linear scale correction factors for each dimension and the lateral coupling, could be determined with high accuracy, although the remaining mean point error $\bar{\zeta}_p$ is slightly larger than the size of a pixel. Introducing the possibility of lateral coupling, $\bar{\zeta}_p$ decreases to 58 nm, but still remains larger than the size of a pixel. An explanation for the remaining differences between the reference measurement by the SiS-Nanostation and the calibrated Veeco Explorer measurement is that it is most likely due to non-linearities introduced by the latter instrument, as the Veeco device is operated by a tripod scanner without closed-loop (table 2.3) scanning movement control. An option for comparing the two calibration procedures applied is given

Table 6.9: Correction factors determined by one- and two-step calibration methods

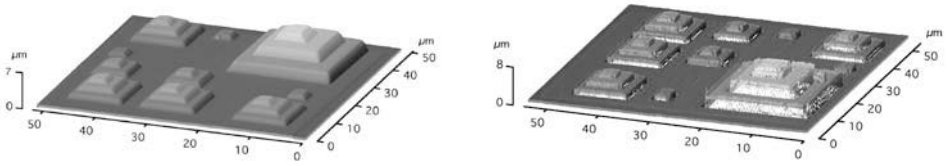
correction factor	c_x	c_y	c_z	c_{xy}
3D reference object	1.163	1.293	1.269	-0.003
2D and 1D reference objects	1.144	1.296	1.167	-0.035

in table 6.9. While the correction factors generally indicate an identical amount of scaling and coupling needed for each dimension, they differ up to 8 % from each another in the z-direction. One explanation might be the above mentioned decoupling of the dimensions in the 2D pitch and 1D step height measurements, as already mentioned. If that is the reason, no direct comparison could even be possible and the question would remain, which approach is more appropriate, in terms of representing a real measurement situation. Another possible explanation lies in prerequisites in data preparation for the two-step calibration with lateral and height pitch features. Because the vertical scaling factors are obtained by analyzing the histogram of distinct step heights, and because of choosing the height distance between peaks of the height histogram maximum (which represents the top of a step), and the minimum (which represents the bottom of the reference structure), the main plane of the step height reference structure should be oriented parallel to the measurement plane of the scanning device. This situation can often only be approximated. Any inclination of the main plane results in a broadening of the height histogram, and hence in a less accurate peak determination. Such inclinations can be corrected by most SPM software solutions, but the correction method applied is a compromise, and, strictly speaking, only corrects for very small deviations from the parallel orientation, because it simply subtracts a plane from the measurement data, instead of applying a spatial transformation consisting of 3 rotational degrees of freedom. In contrast, already implemented in the 3D calibration approach based on parameter estimation are not only three scaling factors and estimates the coupling, but also three translations and three rotations in space. Further explanations are, of course, errors in reference measurements or in reference step height structures.

6.2.2 CLSM 3D calibration

Because the landmark-based calibration should also be applicable to CLSM, the reference array F03, with larger, ring shaped nanomarkers was designed and built. Again, the nanomarker object coordinates of the F03 reference array were also determined by SiS-Nanostation SPM measurement. In the CLSM measurement, the large nanomarkers can be recognized in color-coded height maps of the measurement, as well as in projection images of the CLSM measurement, which provide better contrast. A projection image contains the projection of all CLSM z-slices to an image plane, using only the maximum z-signal of a certain lateral position. The CLSM measurements were carried out with a 488 nm laser using an N PLAN 100x objective with a numerical aperture N_A of 0.9. The size of the pinhole was 354 μm . Both a sample CLSM measurement and the SPM reference measurement are shown in figure 6.7 as a color coded, artificially illuminated 3D representation created by the “Image SXM” software by Steve Barret, a package for scanning microscopy based on NIH Image (NIH Image, National Institutes of Health, Bethesda, USA).

The object coordinates of the nanomarkers in the CLSM measurement have been determined according to the strategy shown in figure 5.2. First, from the projection image, the image coordinates were extracted by using template matching (chapter 5). Then, by knowing the lateral position, the corresponding z-value was read out from the 3D measurement data. The array F03 contains 9 substructures that altogether



(a) Array F03 reference measurement by SiS-Nanostation SPM

(b) Array F03 calibration measurement by Leica TCS CLSM

Figure 6.7: 3D reference array F03 measurements by SPM and CLSM

carry 343 nanomarkers. As each single coordinate counts as a random variable (l_i), a total of 843 observations could be used for the parameter calibration. The parameter

Table 6.10: CLSM one-step calibration: calibration parameter estimation

number of estimated parameters	9	10	10	10
observations	843	843	843	843
scale correction factor c_x	1.001	1.001	1.000	1.000
scale correction factor c_y	0.954	0.954	0.954	0.952
scale correction factor c_z	0.944	0.944	0.944	0.945
coupling correction factor c_{xy}	-	0.004	-	-
coupling correction factor c_{xz}	-	-	0.001	-
coupling correction factor c_{yz}	-	-	-	0.053
mean point error $\bar{\zeta}_p$ [nm]	44.5	43.5	49.4	40.0

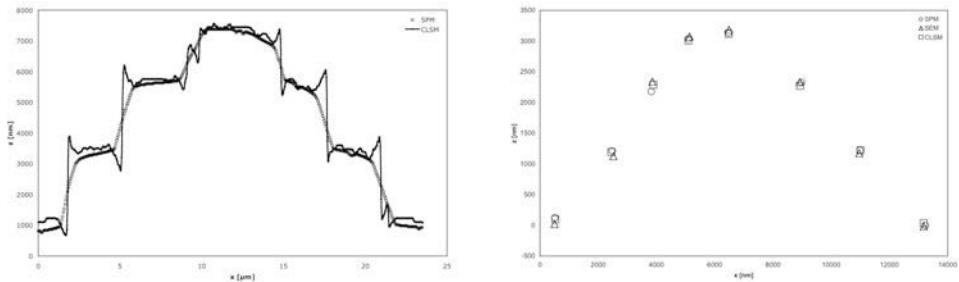
estimation was carried out with the object coordinates of the SPM measurement as given references. One parameter estimation model involved coupling, while the other one was based on non-isotropic scaling. Results are shown in table 6.10. Using lateral coupling (c_{xy}) or an allowed coupling between the x and z dimension (c_{xz}) as an additional degree of freedom does not notably affect the result expressed by the mean point error ($\bar{\zeta}_p$). However, a small coupling between the y and z dimension can be observed, improving the resulting residues of the registration to a mean point error ($\bar{\zeta}_p$) of 40 nm. Interestingly, the overall resulting $\bar{\zeta}_p$ is far below the theoretical resolution of the CLSM, which, for the laser wavelength of 488 nm applied, is about 250 nm. Instead, the detected mean point error is 45 nm for the non-isotropic scaling model, and 40 nm to the affine 3D model with a coupling correction factor for c_{yz} . The results indicate an excellent applicability of the subpixel detection method used for determining the virtual center coordinates of the nanomarkers, and also for the larger ring-shaped ones which were used for the CLSM calibration.

6.3 CORRELATIVE MEASUREMENTS

A long-term goal of the calibration method based on landmarks for the micro-range may be best described as establishing a framework for correlative measurements - that is, allowing an accurate calibration of various 3D microscopy devices by one, or an array of, versatile, scalable reference structures carrying suitably sized and shaped nanomarkers for the microscopes intended.

6.3.1 Landmark-based correlative measurements

The application of the nanomarkers guarantees calibration measurements that are as independent of the geometrical shape of the reference structure as possible. Figure 6.8a shows the profile of identically located object points measured by SPM and CLSM. The profiles are taken from the reference array F03, drawn from the center of nanomarker 11 to the center of nanomarker 21 of substructure P400. A profile from photogrammetric 3D reconstruction could not be obtained, because the texture of the reference structure in the SEM images is too low for area-based matching. The analogy of the SPM and CLSM profiles available is obvious; however, edge effects commonly introduced by CLSM measurements (fig. 6.8a) at the beginning and at the end of each pyramidal slope step do not allow direct quantitative dimensional comparison of homologous points in the two measurements. Better suited for calibra-



(a) Profile drawn along the nanomarker centers by SPM and CLSM

(b) Object coordinates of nanomarkers by SPM, SEM and CLSM

Figure 6.8: Profile and object coordinates of nanomarkers 411 to 421 of reference array F03

tion purposes and direct comparison of the object coordinates is the use of discrete control points (fig. 6.8b), in which the 3D nanomarker coordinates 11 to 21 of the F03-array substructure P400, retrieved by three measurement methods - SPM, photogrammetric SEM and CLSM - are shown. Of course, the quantitative comparison of the 3D geometry of the reference structures retrieved by correlative measurements could be used to identify the peculiarities of each method and, therefore, to conduct a more holistic approach to study the limitations and characteristics of each 3D measurement method beyond such common parameters as resolution or noise. In this section, however, the focus lies on the dimensional calibration and comparison of a discrete number of control points: the nanomarkers. Although only 50 to 300

of the control points are available for correlation of the reference structure measurement, this is sufficient for accurate calibration and for the analysis and retrieval of systematic errors of the given measurements.

6.3.2 Systematic error analysis by correlative measurements

The photogrammetric self-calibration delivers, as a byproduct, the object coordinates of the observed control points, in this case of the substructure P000 of the reference array F04. In that specific measurement, the object coordinates were extracted from the self-calibration analysis of the Nova DualBeam that was applied when testing the accuracy, repeatability and stability of the built-in eucentric stage (table 6.3). The calibration parameters obtained are shown in table 6.11. The derived object coordinates from the SEM self-calibration were registered to the measured SPM coordinates by a rigid transformation, and the remaining residues were summarized by the mean point error $\bar{\zeta}_p$ shown at the bottom line of table 6.11 for correlative analysis. The largest part of the mean point error comes from residues in the x-direction, where the mean of the absolute deviations is 114 nm, in contrast to 12 nm in the y-direction and 36 nm in the z-direction. The same phenomenon can be observed when the object

Table 6.11: Mean point error of photogrammetric SEM registered to SPM coordinates

parameters	scale	scale and distortions
nominal scale	0.0638	0.0638
scale	$0.06357 \pm 7.431 \cdot 10^{-6}$	$0.06350 \pm 1.698 \cdot 10^{-5}$
distortions r_1	-	$8.610 \cdot 10^{-10}$
distortions r_2	-	$1.058 \cdot 10^{-8}$
mean point error $\bar{\zeta}_p$ [nm]	89.05	82.96

coordinates are retrieved from SEM images of the substructure P000 of the reference array F04 by a simple forward section in space, and again registered to the object coordinates measured by SPM (tab. 6.12). It is understandable that the mean point

Table 6.12: Mean point error of coordinates from simple forward section registered to SPM coordinates

calibration parameters	scale	scale and distortions
mean point error $\bar{\zeta}_p$ [nm]	95.22	88.43

error of the simple forward section registration is larger (table 6.12) than the mean point error of the self-calibration. The forward section in space only involved two tilted SEM images with a given orientation, whereas the self-calibration involved 34 images for the bundle-adjustment. But, in the case of the forward section, the largest

part of the mean point error also comes from deviations in the x-direction, that is, 118 nm, compared to 13 nm in the y-direction and 45 nm in the z-direction. Therefore,

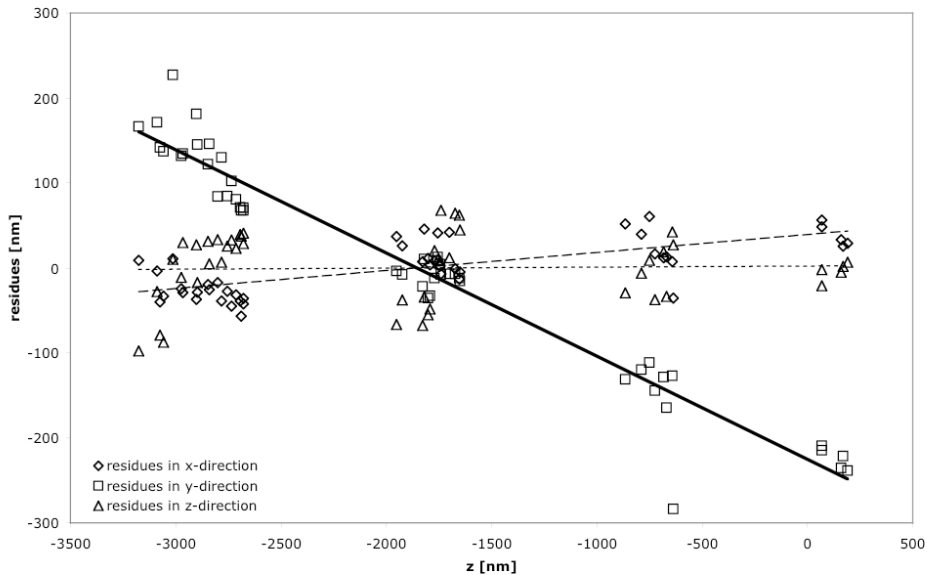


Figure 6.9: Residues after 3D transform of SEM to SPM object coordinates of F03 P000

the dependencies of the residues with respect to the three coordinate directions were analyzed. Figure 6.9 indicates that the size and direction of the residues in x-direction are linearly dependent on their z-location. By expanding the registration by parameter estimation from a rigid transformation to an affine model with 10 parameters (table 6.13), a clear dependency of the resulting mean point errors could be stated. Table 6.13 again shows the mean point errors for the rigid 3D transform in column 1, and in column 2, the mean point errors for transform by non-isotropic scaling, allowing 3 scale factors to the additional rotations and translations. No obvious improvement of the results as expressed by the mean point error could be achieved by the expansion of the rigid geometric model by 3 scaling factors. The same is true for introducing one more parameter, a shear factor allowing non-orthogonality between the two coordinate axes x and y (c_{xy}) or between y and z (c_{yz}), respectively. If, however, such coupling of the x- and z-plane is introduced to the geometric model for the 3D registration, the mean point error drops from 83 nm to 12 nm, approximately 20 % of the size of a pixel or measurement point, and a 7 fold improvement to the other transforms shown in table 6.13. Hence, c_{xz} is absolutely necessary to linearly describe, by the geometric model, an obvious systematic error in at least one of the two measurement methods. Yet, from the data shown, it cannot be concluded where this

Table 6.13: Correlative analysis of 3D object coordinates of F04 array substructure P000

SEM to SPM coordinate registration					
parameter	6	9	10	10	10
c_x	-	0.998	0.998	0.999	0.998
c_y	-	0.998	0.998	0.998	0.998
c_z	-	0.984	0.984	0.983	0.984
c_{xy}	-	-	0.001	-	-
c_{xz}	-	-	-	-0.134	-
c_{yz}	-	-	-	-	0.011
mean point error $\bar{\zeta}_p$ [nm]	83.0	82.1	82.4	12.7	82.2

systematic error is actually generated. Because the object coordinates derived from the photogrammetric self-calibration were obtained by using as many as 34 images, tilted and rotated several times, and each with up to 54 control point observations, it seemed unlikely that the error was due to the photogrammetric SEM measurement. However, there was no other actual proof, and in order to evaluate the cause of the systematic error, further data obtained from additional 3D measurement methods were necessary. Therefore, substructure P400 of the large, ring-shaped nanomar-

Table 6.14: Correlative analysis of 3D object coordinates of F03 array substructure P400

coordinate registration	SEM to SPM	CLSM to SPM	CLSM to SEM
parameter	9	9	9
c_x	1.002	1.004	1.002
c_y	0.990	0.961	0.971
c_z	1.066	0.967	0.900
mean point error $\bar{\zeta}_p$ [nm]	78.2	49.6	50.4
parameter	10	10	10
c_x	1.002	1.003	1.002
c_y	0.978	0.954	0.972
c_z	1.073	0.965	0.903
c_{yz}	0.126	0.071	-0.069
mean point error $\bar{\zeta}_p$ [nm]	26.4	32.5	38.4

ker reference array F03 was measured by SPM, CLSM and photogrammetric SEM (Nova DualBeam). The resulting object coordinates were registered to each other by a non-isotropic scaling and by a 3D affine transform, respectively. The results

are shown in table 6.14. Interestingly, when the 3D affine parameter estimation was applied, allowing a shearing between two axes of the coordinate planes, the largest coupling did not occur in the xz-plane as observed in the correlation of the SPM to SEM measurement, but in the yz-plane. If yz-shearing is allowed in the geometrical model of the registration, the mean point error drops by a factor of 3, from 78 nm to 26 nm, for the correlation of the SPM to the SEM measurement, and by a factor of 1.3 for the other two possible remaining correlations (SEM and CLSM, and SPM to CLSM). A closer look at the SPM measurement data revealed that, in the case of the correlation between SPM and SEM (table 6.13), the direction of the largest residues (x-direction) corresponds to the slow (y-axis) measurement direction of the SPM measurement. The same is true for the measurement shown in table 6.14, in which the direction of the largest residues (this time the y-direction) also corresponds to the y-axis of the SPM measurement. If registering the CLSM object coordinates to the SPM object coordinates by the 3D affine transformation, allowing yz-shearing, the coupling factor c_{yz} is only half the size of the SEM to SPM correlation. And, if registering the object coordinates retrieved by SEM to the CLSM object coordinates, the coupling factor c_{yz} changes direction, but remains half the size of the maximum shearing between SPM and SEM coordinate registration. From the results of the

Table 6.15: c_{yz} characteristics

	SPM	SEM	CLSM	SEM to SPM	CLSM to SPM	CLSM to SEM
1.	⊖	⊕⊕	⊖	⊕⊕	⊖	⊕
2.	⊖	⊖	⊕⊕	⊖	⊕⊕	⊕
3.	⊕⊕	⊖	⊖	⊕⊕	⊕	⊖
4.	⊖	⊖	⊕⊕	⊖	⊕	⊕⊕
5.	⊕⊕	⊖	⊖	⊕	⊕⊕	⊖
6.	⊖	⊕⊕	⊖	⊕	⊖	⊕⊕

affine registration with shearing allowed in the yz-plane (table 6.14), the following information can be extracted:

- no zero coupling occurs in the correlations of the measurements
- one correlation shows a negative coupling
- the sum of the absolute amount of the smaller coupling factors corresponds to the amount of the large coupling factor

From the first point it can be concluded that more than one measurement shows coupling of the yz-plane. As the shearing can become negative, one can also assume opposite directions of the coupling among the measurements. The sum of the absolute amount of the coupling of two correlations corresponds to the absolute amount of the remaining correlation. Hence, the hypothesis can be stated that one measurement does not show any coupling, one measurement shows a strong coupling in the positive

direction, and the third measurement shows a weak coupling in the negative direction. The zero coupling is indicated by a \odot , the weak negative coupling by a \ominus and the strong positive coupling by a $\oplus\oplus$. Table 6.15 lists all the 6 possibilities on the basis of the hypothesis that has been stated. Considering the coupling factor c_{yz} in table 6.14, only possibility number 3 in table 6.15 reflects the actual measured results of the correlations. Therefore, the SPM measurement must be affected by a strong positive coupling, whereas the CLSM measurement is affected by a weak coupling in the opposite direction. No other possibility corresponds to the correlated results.

DISCUSSION AND OUTLOOK

Within this thesis, a new strategy for the geometrical 3D calibration of scanning microscopes (SPM, CLSM and photogrammetric SEM) through the application of three-dimensional (3D) micrometer sized reference structures with the shape of cascade slope step pyramids and with circle or ring shaped landmarks (nanomarkers) is presented. The nanomarkers serve as the reference points for the calibration, whereas the shape of the structure is designed to fit best the needs of the chosen measurement method. The complete landmark-based calibration procedure includes a variety of methods:

1. Fabrication of versatile reference structures by focused ion beam (FIB) metal deposition.
2. Circle or ring shaped nanomarker application onto the reference structures by FIB milling.
3. Semi-automatic, sub-pixel nanomarker center coordinate determination by correlation, edge detection and ellipse fitting of the digital data.
4. Supply of nanomarker image coordinates for photogrammetric SEM, or nanomarker object coordinates for SPM and CLSM calibration.
5. Selection of adjustable geometrical models of the scanning process for SPM and CLSM through choice of appropriate scale and coupling factors, or adjustable selection of the law of projection, distortion parameters and the photogrammetric calibration model for SEM [Hemmler 01].
6. Nanomarker object coordinate reconstitution and calibration by least-squares parameter estimation.

The modeled distortions include scaling factors c_x , c_y , c_z in 3 dimensions and coupling factors c_{xy} , c_{xz} , c_{yz} of the respective coordinate planes, as well as scale and non-linear radial and spiral distortions $\Delta x'$ and $\Delta y'$ in electron optical systems (see chapter 3). With this new strategy, the most common scanning microscopes have been calibrated (see chapter 6). And, coupling effects other than lateral shear [Jorgensen 98] have been verified in the scanning process of SPM and CLSM (see table 6.14).

Benefits of FIB reference structure fabrication

Modern FIB devices offer two patterning modes for creating micrometer-sized geometrical structures on suitable substrates: milling and deposition. Milling is consistent with the removal of substrate material to create patterns, and deposition is

consistent with the addition of metal onto the substrate to build structures. The geometry and shape of the micro-structures that can be built by FIB milling or deposition is almost arbitrary [Giannuzzi 04]. However, FIB induced metal deposition allows more flexibility, because it can be applied without having to take into account structural properties of the substrate, and the problematic effect of redeposition of removed substrate material at large aspect ratios of the created geometry does not occur [Yamaguchi 85] (see chapter 4).

Another advantage in using metal as the main material for fabricating the 3D reference structures lies in its conductivity and its reflectivity. Except for environmental scanning electron microscopes (ESEM) [Danilatos 93b] or low voltage scanning electron microscopes (LVSEM) [Joy 96], a conductive sample or a conductive layer on a specimen is needed for SEM investigations. On the other hand, for CLSM surface analysis in reflective mode, the reflectance of the specimen is one of the main properties determining the signal intensity [Cheng 95]. The reflectance of platinum, for example, is 73 %, which is close to gold (95 %), and much larger than silicon (28 %) [Website 05], the main material for the fabrication of 1D and 2D reference structures by etching or electron beam lithography.

The commonly used fabrication techniques of etching smoothly lead up to the task of automatization, for it can be repetitively applied, once a so-called mask is established. For electron beam lithography or focused ion beam lithography, the formation of geometrical structures is dependent upon the accuracy of beam positioning and a fast beam on/off switch [Melngailis 93], which is referred to as beam blanking. Both properties are improved and controllable in modern FIB devices. Especially with new user software that has been developed [FEI 00b], several hundreds of basic geometric figures can be defined for one patterning process, allowing the easy fabrication of geometrical structures.

Reference structure design

The simplest 3D structure would be a cube. However, the vertical steps of a cube prevent accurate measurements by photogrammetric SEM, due to the necessary tilting of the reference structure for calibration purposes and the reconstitution of the object coordinates (see chapter 6). By introducing slope steps (fig. 4.6), covered areas on a reference object that is tilted are minimized. Additionally, slope steps that are less steep than the apex of a SPM tip can be measured by SPM without introducing artifacts to the measured data by rounding effects due to the tip geometry (see chapter 4). However, edge effects in CLSM height measurement could not be prevented (fig. 6.7a). Most likely, such overmodulation is caused by the local surface orientation of the structure, which has a profound effect on the final image contrast [Cheng 95].

In order to be able to calibrate scanning microscopes within an optimal measurement range, the lateral area covered with reference structures was expanded up to $50 \mu\text{m}^2$ (fig. 4.6) by arranging substructures in an array. In addition, several slope steps were applied on each other, resulting in a pyramidal shape of the substructures (fig. 4.6). The chosen geometry has the advantage of a large total structural height for optimum z -calibration in a large range, yet subdivided into small steps for a max-

imum of height information in case of a measurement range that is below the total height, e.g., the depth of field in SEM at very high magnification. And, not least of all, the plateaus serve perfectly as locations for a well distributed application of the nanomarkers at various heights.

Advantages of the landmark-based 3D calibration strategy

1D and 2D gratings use gratings or single step heights as prominent features with which the lateral or vertical pitch distance is defined (fig. 1.2). Calibration is then performed in sequential steps of lateral and height measurements with the appropriate reference standards. For lateral calibration, the measured pitch of the grating is compared to the nominal pitch, and coupling effects of the xy -plane are eventually also determined by analyzing non-orthogonality of the imaged grating [Jorgensen 98]. For the height calibration, the vertical pitch can be calculated by histogram analysis or by ISO 5436 [Dziomba 05]. In contrast to the use of 1D or 2D pitch features, a true 3D reference object containing circular or ring shaped landmarks (fig. 5.1) is introduced. Such reference structures allow the calibration of 3D measurement systems as CLSM and SPM in one step (see chapter 7). Also, using discrete control points with distinct 3D coordinates has the advantage of being able to detect coupling effects of lateral coordinates with respect to their height (fig. 3.3). As shown in table 6.13, such coupling effects do occur, and they can be corrected, once the device has been calibrated by a landmark-based 3D reference standard.

Furthermore, the landmark-based reference structures are well suited for photogrammetric calibration of SEM (fig. 6.5), provided that a positioning stage with high relative tilt accuracy is available (table 6.4). By photogrammetric self-calibration, not only can the scale factor of the SEM be determined, but also the positioning accuracy of the stage applied (table 6.2). Once the relative positioning accuracy of a specimen stage is determined, it could be used for quantitative photogrammetric 3D reconstruction of continuous surfaces by area-based matching [Hemmler 01]. However, a minimum of evenly distributed nanomarkers is required for a successful calibration.

Accuracy considerations of 3D calibration strategy

A major precondition of the landmark-based method for micro-range calibration of 3D scanning microscopes is the accurate determination of the control point coordinates (see chapter 5). For that purpose, control points in SEM images and color-coded images of SPM and CLSM height measurements were obtained by template matching with a cross-correlation routine (fig. 5.3). Subpixel accuracy was achieved by applying edge detection and ellipse-fitting algorithms for template centering (fig. 5.2). In synthetic test image data, a mean point error of 0.09 to 0.27 pixel, depending on the amount of synthetic noise applied, was achieved (table 5.3.1). Slightly better results were obtained if the coordinate centroid was determined in the correlation coefficient image and not in the gray value image (fig. 5.10). However, the determination of the uncertainty expressed by the mean point error in synthetic data is a rather simple task, because the true pixel positions are known. In order to obtain the control

point coordinate uncertainty in real data, 11 different templates were applied to one single image and the mean point error of the determined control point coordinates was calculated in SPM and SEM data. For both data sets, a mean point error of 0.20 to 0.25 pixel resulted (figs. 5.15 and 5.16). For the specified SPM measurement (fig. 5.12b), the height data for the correlated lateral position were retrieved according to the strategy shown in figure 5.2. The resulting uncertainty of the object coordinates was then calculated as 5 nm to 6 nm, depending on the template size used for the correlation.

The one-step calibration of a Veeco Explorer (Veeco, USA) SPM with a landmark-based 3D reference object shown in table 6.8 results in a remaining mean point error of approximately 60 nm, regardless of the couplings allowed in the geometric model, whereas the resulting mean point error in a one-step 3D calibration of a Leica CLSM was only 40 nm (table 6.10). This strongly indicates non-linear distortions in the Veeco SPM measurement shown here, that could not be corrected with the linear approach. The measurement was repeated (not shown) using an alternative reference array with the same resulting mean-point error. Edge effects, although not as prominent as in CLSM data (fig. 6.7a), are occurring to all applied 3D micro-range measurements [Reimer 87a, Gibson 97].

In correlative measurements, the mean point error of nanomarker coordinates measured by SPM and photogrammetric SEM could be reduced from 82.1 nm to 12.7 nm after parameter estimation with 3 modeled scale factors and vertical coupling factors 6.13, whereas a mean point error of 32.5 nm for SPM and CLSM data, and 38.4 nm for photogrammetric SEM and CLSM data, was determined (see table 6.14). Hence, the mean point error is below pixel size for all correlative measurements, and, most interestingly, in the case of CLSM, they are way below the theoretical and practical resolution of the microscope [Hamilton 82]. On the one hand, these results strongly indicate that the chosen geometrical model for describing the scanning process is reasonable and even necessary for calibration. On the other hand, they demonstrate the necessity of a sub-pixel accurate nanomarker coordinate determination with the chosen methods, - and, by that, the overall power of the landmark-based calibration strategy.

Outlook

This short outlook deals with two possibilities for improving this 3D calibration strategy: expanding the geometrical model for the scanning process, and altering the automatization routine for the fabrication of the reference structures by FIB metal deposition.

The array of reference structures fabricated by FIB metal consist of 50 or more single geometrical elements (fig. 4.6c,d). Manually creating such complex structures was too time consuming. In order to automatize the fabrication of the reference structures, several approaches given by the user software were tested, among them scripting with *AutoScript* [FEI 00b] and digitally coded documents, such as color-coded bitmaps (4.12). Applying bitmaps was not a solution, because of drift effects due to the parallel processing of all the substructures of the array (fig. 4.12b,c), whereas using *AutoScript* provided good results (fig. 4.13), because it allows serial

production of one structure after another. However, the results indicated that there is a strong correlation of the thickness of the deposited layers to the lateral deposition area (fig. 4.18), probably due to the limited span of beam current that should be applied for a defined patterning area (see eqn. 4.8). It should be tested whether this correlation could be reduced by adjusting a tolerable ion beam current for each single geometrical element - in other words, predefine an operational beam current with respect to the size of the area of the patterned structure. Such an approach is not possible with *AutoScript*. However, there is an expansion to the *AutoScript* module called AutoFIB [FEI 00a] that allows for each beam and patterning setting the sequential processing of numerous scripts. By applying the AutoFIB module, a better tuning of the patterning parameters seems possible, and hence a more reliable and accurate fabrication of the reference structures.

[Zhao 98] defined 21 degrees of freedom for a scanning probe microscope with high-resolution capacitive transducers, among them the scaling factors, several coupling factors, and rotations. For routine calibration, it will not be practicable to take into account all of the degrees of freedom. Moreover, such a model may prove unstable for parameter estimation, because several of the correction factors will not be independent of others. The geometric model for the description of the scanning process applied here only includes linear factors as scale, and coupling in three dimensions. Despite this linear approach, the mean point error of the correlative coordinate measurements could be reduced to approximately on fourth of a pixel size. The determination of non-linear scale correction factors as applied for the lateral case by [Jorgensen 98] for lateral SPM calibration was not implemented. The same is true for the correction of the scan bow [Bhushan 04], which is usually eliminated by subtracting a second or higher order plane that is determined by a flatness calibration [Koenders 04]. However, it will be interesting to determine whether remaining residues of the coordinate registration between the various types of measurements could be further reduced by introducing non-linear terms in the geometrical model. But when considering expansion the model, multiple factors need to be weighed - for example, whether too many parameters may cause problems to the least-square estimation, and, whether only a few, distinct non-linear parameters might be introduced that could significantly improve the result of the parameter estimation. Here the opinion is that parameters for the non-linear correction of lateral distortions for SPM and CLSM, as well as the elimination of the scan bow for SPM, should be considered in the geometrical model of the parameter estimation to further improve calibration measurements.

BIBLIOGRAPHY

- [Bell 88] A. E. Bell, K. Rao, G. A. Schwind & L. W. Swanson. *A low-current liquid metal ion source*. Journal of Vacuum Science and Technology, vol. B6, pp. 927–930, 1988.
- [Bhushan 04] B. Bhushan (ed.). Springer Handbook of Nanotechnology. Springer Verlag, Berlin, 2004.
- [Bienias 98] M. Bienias, S. Gao, K. Hasche, R. Seemann & K. Thiele. *A metrological scanning force microscope used for coating thickness and other topographical measurements*. Applied Physics A: Materials Science & Processing, vol. 66, pp. 837–842, 1998.
- [Binnig 82] G. Binnig, H. Röhler, C. Gerber & E. Weibel. *Surface studies by scanning tunneling microscopy*. Physical Review Letters, vol. 49, pp. 57–61, 1982.
- [Binnig 86] G. Binnig, C. F. Quate & C. Gerber. *Atomic force microscope*. Physical Letters Review, vol. 56, pp. 930–933, 1986.
- [Boyd 70] A. Boyd. *Practical problems and methods in the three-dimensional analysis of scanning electron images*. In Proceedings of the Third Annual Scanning Electron Microscope Symposium, pp. 105 – 112, IIT Institute, Chicago, 1970.
- [Boyd 73] A. Boyd. *Quantitative photogrammetric analysis and qualitative stereoscopic analysis of SEM images*. Journal of Microscopy, vol. 98, no. 3, pp. 452–462, 1973.
- [Büchner 99] H.-J. Büchner, G. Jäger, U. Gerhardt & K. Hasche. *Entwicklung eines 3D-laserinterferometrischen Nanomesssystems für den Abbe-fehlerfreien Einbau in Rastermikroskope*. Technisches Messen, vol. 66, no. 12, pp. 504–510, 1999.
- [Burkhardt 81] R. Burkhardt. Methodensammlung der Elektronenmikroskopie, volume 10, chapter: Die stereoskopische Ausmessung elektronenmikroskopischer Bildpaare und ihre Genauigkeit, pp. 1–59. Wissenschaftliche Verlagsgesellschaft Stuttgart, Stuttgart, 1981.
- [Canny 86] J. Canny. *A computational approach to edge detection*. IEEE Transaction on Pattern Analysis and Machine Intelligence, vol. 8, no. 6, pp. 679–698, 1986.
- [Carlsson 91] K. Carlsson & P. Lundahl. *Three-Dimensional Specimen Recording and Interactive Display Using Confocal Laser Microscopy and Digital Image Processing*. Machine Vision and Applications, vol. 4, pp. 215–225, 1991.
- [Cheng 95] P. C. Cheng & A. Kriete. Handbook of biological confocal microscopy, chapter: Image Contrast in Confocal Light Microscopy, pp. 281–309. Plenum Press, New York, 1995.

- [Clampitt 90] R. Clampitt, P. W. Mingay & S. T. Davies. *Micromachining with focused ion beams*. Sensors and Actuators A: Physical, vol. 25, no. 1-3, pp. 15–20, 1990.
- [Collins 93] S.P. Collins, R.K. Pope, R.W. Scheetz, R.I. Ray, P.A. Wagner & B.J. Little. *Advantages of environmental scanning electron microscopy in studies of microorganisms*. Microscopy Research and Technique, vol. 25, no. 5-6, pp. 398–405, 1993.
- [Cowan 96] A.J. Cowan, N.H. Wilson, M.A. Wilson & D.C. Watts. *The application of ESEM in dental materials research*. Journal of Dentistry, vol. 24, no. 5, pp. 375–7, 1996.
- [Danilatos 78] G. D. Danilatos. *Foundations of environmental scanning electron microscopy*. Advances in Electronics and Electron Physics, vol. 71, pp. 102–250, 1978.
- [Danilatos 90] G. D. Danilatos. *Theory of the gaseous detector device in the environmental scanning electron microscope*. Advances in Electronics and Electron Physics, vol. 78, pp. 1–102, 1990.
- [Danilatos 93a] G.D. Danilatos. *Bibliography of environmental scanning electron microscopy*. Microscopy Research and Technique, vol. 25, no. 5-6, pp. 529–34, 1993.
- [Danilatos 93b] G.D. Danilatos. *Introduction to the ESEM instrument*. Microscopy Research and Technique, vol. 25, no. 5-6, pp. 354–61, 1993.
- [Davies 96] ST Davies & B Khamsehpour. *Focused ion beam machining and deposition for nanofabrication*. Vacuum, vol. 47, no. 5, pp. 455–462, 1996.
- [Donald 03] A. M. Donald. *The use of environmental scanning electron microscopy for imaging wet and insulating materials*. Nature materials, vol. 2, no. 8, pp. 511–516, 2003.
- [Dougherty 98] S. Dougherty & K. W. Bowyer. Empirical evaluation technics in computer vision, chapter: Objective evaluation of edge detectors using a formally defined framework, pp. 211–234. Wiley-IEEE Computer Society Press, 1998.
- [Dziomba 05] T. Dziomba, L. Koenders & G. Wilkening. *Standardization in dimensional nanometrology: development of a calibration guideline for Scanning Probe Microscopy*. SPIE, SPIEEurope Optical Design - Optical Fabrication, Testing and Metrology II, Jena/Germany, vol. 5965-12, 2005.
- [Eisenhart 63] C. Eisenhart. *Realistic Evaluation of the precision and accuracy of instrument Calibration system*. Journal of Research of the National Bureau of Standarts, vol. 67c, 1963.
- [Elghazali 84] M. S. Elghazali. *System Calibration of Scanning Electron Microscopes*. Intern. Archives of Photogrammetry and Remote Sensing, Rio de Janeiro, vol. XXV, no. Part A5, pp. 258–266, 1984.
- [Erasmus 80] S. J. Erasmus & D. M. Holburn. *On-line computation of diffractograms for the analysis of SEM images*. Scanning, vol. 3, pp. 273–279, 1980.

- [Everhart 60] T. E. Everhart & R. F. M. Thornley. *Wide-band detector for microampere low-energy electron currents*. Journal of Scientific Instruments, vol. 37, pp. 246–248, 1960.
- [FEI 00a] FEI. *AutoFIB 2.25 Software Addendum. xP Focused Ion Beam and xP DualBeam Manual Sets*. FEI Company, 7451 NW Evergreen Parkway, Hillsboro OR, USA, 2000.
- [FEI 00b] FEI. *AutoScript Technical Note*. FEI Company, 7451 NW Evergreen Parkway, Hillsboro OR, USA, 2000.
- [FEI 00c] FEI. *RunScript User's Guide*. FEI Company, 7451 NW Evergreen Parkway, Hillsboro OR, USA, 2000.
- [FEI 00d] FEI. *xP Focused Ion Beam System User's Guide*. FEI Company, 7451 NW Evergreen Parkway, Hillsboro OR, USA, 2000.
- [FEI 04] FEI. Focused ion beam technology, capabilities and applications. 030-PB00112 05/04, FEI Company, 5350 NE Dawson Creek Drive, Hillsboro, OR, USA, 2004.
- [Fitzgibbon 95] A. W. Fitzgibbon & R. B. Fischer. *A buyer's guide to conic fitting*. In Proceedings of the British Machine Vision Conference, pp. 265–71, 1995.
- [Fitzgibbon 96] A. W. Fitzgibbon, M. Pilu & R. B. Fischer. *Direct least squares fitting of ellipses*. In Proc. of the 13th International Conference on Pattern Recognition, pp. 253–257, Vienna, 1996.
- [Fletcher 99] A. L. Fletcher, B. L. Thiel & A. M. Donald. *Signal components in the environmental scanning electron microscope*. Journal of Microscopy, vol. 196, no. 1, pp. 26–34, 1999.
- [Frase 04] C. G. Frase, B. Bodermann, W. Hässler-Grohne, S. Czerkas, W. Mirande & H. Bosse. *Metrologische Charakterisierung von neu entwickelten Photomasken-Strukturbreiten-Normalen*. PTB Mitteilungen, vol. 114, no. 1, pp. 36–43, 2004.
- [Fu 00] Yong-Qi Fu, Ngoi Kok & Ann Bryan. *Microfabrication of microlens array by focused ion beam technology*. Microelectronic Engineering, vol. 54, no. 3-4, pp. 211–221, 2000.
- [Fu 01] Y. Fu, K. A. B. Ngoi & O. N. Shing. *Characterization of focused ion beam induced deposition process and parameters calibration*. Sensors and Actuators A, vol. 88, no. 1, pp. 58–66, 2001.
- [Gamo 84] K. Gamo, N. Takakura, N. Samoto, R. Shimizu & S. Namba. *Ion Beam Assisted Deposition of Metal Organic Films Using Focused Ion Beams*. Japanese Journal of Applied Physics, vol. 23, no. 1, pp. L293–L295, 1984.
- [Giannuzzi 99] L. A. Giannuzzi & F. A. Stevie. *A review of focused ion beam milling techniques for TEM specimen preparation*. Micron, vol. 30, no. 3, pp. 197–204, 1999.
- [Giannuzzi 04] L. A. Giannuzzi, B. I. Prenitzer & B. W. Kempshall. Introduction to Focused Ion Beams, chapter: Ion-Solid Interactions, pp. 13–52. Springer Science + Business Media Inc., New York, 2004.
- [Gibson 97] C. T. Gibson, G. S. Watson & S. Myhra. *Scanning Force Microscopy - Calibrative Procedures for Best Practice*. Scanning, vol. 19, pp. 564–581, 1997.

- [Gierak 05] J. Gierak, E. Bourhis, M. N. Merat Combes, Y. Chriqui, I. Sagnes, D. Mailly, P. Hawkes, R. Jede, L. Bruchhaus, L. Bardotti, B. Prével, A. Hannour, P. Mélinon, A. Perez, J. Ferré, J.-P. Jamet, A. Mougin, C. Chappert & V. Mathet. *Exploration of the ultimate patterning potential achievable with focused ion beams*. Microelectronic Engineering, vol. 78-79, pp. 266–278, 2005.
- [Gruen 96] A. Gruen. *Least-squares matching: a fundamental measurement algorithm*, pp. 217–255. Whittles Publishing, Caithness, UK, 1996.
- [Grütter 92] P. Grütter, W. Zimmermann-Edling & D. Brodbeck. *Tip artefacts of microfabricated force sensors for atomic force microscopy*. Applied Physics Letters, vol. 60, pp. 2741–2743, 1992.
- [Haessler-Grohne 98] W. Haessler-Grohne & H. Bosse. *Electron optical metrology system for pattern placement measurements*. Measurement Science and Technology, vol. 9, pp. 1120–1128, 1998.
- [Halir 98] R. Halir & J. Flusser. *Numerically stable direct least squares fitting of ellipses*. In Proc. 6th International Conference in Central Europe on Computer Graphics and Visualization, pp. 125–132, Plzen, Czech Republic, 1998.
- [Hamilton 82] D. K. Hamilton & T. Wilson. *Three-dimensional surface measurement using the confocal microscope*. Journal of Applied Physics B, vol. 27, pp. 211–213, 1982.
- [Haycocks 05] J. Haycocks & K. Jackson. *Traceable calibration of transfer standards for scanning probe microscopy*. Precision Engineering, vol. 29, pp. 168–175, 2005.
- [Hemmler 95] M. Hemmler, J. Albertz, M. Schubert, A. Gleichmann & J. M. Köhler. *Photogrammetrische Bestimmung der Krümmung einer Mikrokantilever-Probe mittels Rasterelektronenmikroskop*. BEDO, vol. 28, pp. 65–72, 1995.
- [Hemmler 01] Matthias Hemmler. *Photogrammetrische Auswertung elektronenmikroskopischer Bilddaten*. PhD thesis, Technische Universität Berlin, 2001.
- [Henriksen 02] K. Henriksen & S. L. S. Stipp. *Image distortion in scanning probe microscopy*. American Mineralogist, vol. 87, no. 1, pp. 5–16, 2002.
- [Hermann 97] R. Hermann & M. Müller. *Limits in High-Resolution Scanning Electron Microscopy: Natural Surfaces*. Scanning, vol. 19, pp. 337–342, 1997.
- [Hoshino 03] T. Hoshino, K. Watanabe, R. Kometani, T. Morita, K. Kanda, Y. Haruyama, T. Kaito, J. Fujita, M. Ishida, Y. Ochiai & S. Matsui. *Development of three-dimensional pattern-generating system for focused-ion-beam chemical-vapor deposition*. J. Vac. Sci. Technol. B, vol. 21, no. 6, pp. 2732–2736, 2003.
- [Howell 78] P. Howell. *A theoretical approach to the errors in SEM photogrammetry*. Scanning, vol. 1, pp. 118 – 124, 1978.
- [Jähne 02] Bernd Jähne. *Digitale Bildverarbeitung*. Springer Verlag, Berlin, 2002.

- [Jalili 04] N. Jalili & K. Laxminarayana. *A review of atomic force microscopy imaging systems: application to molecular metrology and biological sciences*. Mechatronics, vol. 14, pp. 907–945, 2004.
- [Jorgensen 98] J. F. Jorgensen, C. P. Jensen & J. Garnaes. *Lateral metrology using scanning probe microscopes, 2D pitch standards and image processing*. Applied Physics, vol. A 66, pp. 847–852, 1998.
- [Joy 96] D. C. Joy & C. S. Joy. *Low Voltage Scanning Electron Microscopy*. Micron, vol. 27, pp. 247–263, 1996.
- [Joy 00] D. C. Joy, Y.-U. Ko & J. J. Hwu. *Metrics of resolution and performance for CD-SEMs*. In T. N. Sullivan (ed.), *Proceedings of SPIE: Metrology, Inspection, and Process Control for Microlithography XIV*, volume 3998, pp. 108–115. SPIE, 2000.
- [Kaito 04] T. Kaito. *Introduction to Focused Ion Beams*, chapter: Three-Dimensional Nanofabrication Using Focused Ion Beams, pp. 73–86. Springer Science + Business Media Inc., New York, 2004.
- [Kanaya 72] K. Kanaya & S. Okayama. *Penetration and energy-loss theory of electrons in solid targets*. Journal of Physics D: Applied Physics, vol. 5, pp. 43–58, 1972.
- [Ke 01] S. H. Ke, T. Uda, Stich. I. & K. Terakura. *Effect of tip morphology on AFM images*. Applied Physics A: Materials Science and Processing, vol. 72, pp. S63–S66, 2001.
- [Koenders 04] L. Koenders, T. Dziomba, P. Thomsen-Schmidt & M. Senoner. *Normale für die dimensionelle und analytische Nanometrologie*. PTB Mitteilungen, vol. 114, no. 1, pp. 16–24, 2004.
- [Koenig 87] G. Koenig, W. Nickel, J. Storl, D. Meyer & J. Stange. *Digital stereophotogrammetry for processing SEM data*. Scanning, vol. 9, no. 5, pp. 185–193, 1987.
- [Levi-Setti 74] R. Levi-Setti. *Proton scanning microscopy: feasibility and promise*. Scanning Electron Microscopy, p. 125, 1974.
- [Luhmann 00] Thomas Luhmann. *Nahbereichsphotogrammetrie*. Wichmann, Heidelberg, 2000.
- [Maas 92] H.-G. Maas. *Digitale Photogrammetrie in der dreidimensionalen Strömungsmesstechnik*. Nr. 50, ETH Zürich, Institut für Geodäsie und Photogrammetrie, 1992.
- [Manero 00] J. M. Manero, C. Aparicio, M. Nilsson, F. J. Gil & J. A. Planell. *Application of the environmental scanning electron microscope to the field of dental implants*. In EUREM 12, pp. B 609 – 610, Brno, 2000. Czechoslovak Society For Electron Microscopy.
- [Maune 75] D. F. Maune. *SEM Photogrammetric Calibration*. In *Scanning Electron Microscopy: Proceedings of the 8th Scanning Electron Microscopy Symposium*, volume 1, pp. 207–215, St. Louis, 1975.
- [Maurer 98] C. R. Maurer, R. J. Maciunas & J. M. Fitzpatrick. *Registration of head CT images to physical space using a weighted combination of points and surfaces*. IEEE Transactions on Medical Imaging, vol. 17, pp. 753–761, 1998.

- [McMullan 90] D. McMullan. *The prehistory of scanned image microscopy, Part 1: Scanned optical microscopes*. Proceedings of the Royal Microscopical Society, vol. 25, pp. 127–131, 1990.
- [McMullan 95] D. McMullan. *Scanning Electron Microscopy 1928-1965*. Scanning, vol. 17, pp. 175–185, 1995.
- [Melngailis 93] John Melngailis. *Focused ion beam lithography*. Nuclear Instruments and Methods in Physics Research Section B: Beam Interactions with Materials and Atoms, vol. 80-81, no. Part 2, pp. 1271–1280, 1993.
- [Meyer 92] E. Meyer. *Atomic force microscopy*. Progress in Surface Science, vol. 41, pp. 3–49, 1992.
- [Minsky 61] M. Minsky. *Microscopy Apparatus, U. S. Patent 3,013,467*, 1961.
- [Nanosensors 05] Nanosensors. www.nanosensors.com/Metrology.pdf, 2005.
- [Niemeier 02] Wolfgang Niemeier. *Ausgleichsrechnung, eine Einführung für Studierende und Praktiker des Vermessungs- und Geoinformationswesens*. de Gruyter, Berlin, 2002.
- [Orloff 03] Jon. Orloff, Mark. Utlaut & Lynwood Swanson. *High Resolution Focused Ion Beams: FIB and Its Applications*. Kluwer Academic / Plenum Publishers, New York, 2003.
- [Oshima 70] T. Oshima, S. Kimoto & T. Sukanuma. *Stereomicrography with a scanning electron microscope*. Photogrammetric Engineering and Remote Sensing, vol. 36, no. 8, pp. 874–879, 1970.
- [Overwijk 93] M. H. F. Overwijk & F. C. Heuvel van den. *Focused-ion-beam-induced tungsten deposition: theory and experiment*. Nuclear Instruments and Methods in Physics Research Section B: Beam Interactions with Materials and Atoms, vol. 80-81, no. Part 2, pp. 1324–1327, 1993.
- [Pawley 97] J. Pawley. *The Development of Field-Emission Scanning Electron Microscopy for Imaging Biological Surfaces*. Scanning, vol. 19, no. 5, pp. 324–336, 1997.
- [PEO 96] PEO. *Environmental Scanning Electron Microscopy. An introduction to ESEM*. Philips Electron Optics, Building AAE, P.O. Box 218, 5600MD Eindhoven, The Netherlands, 1996.
- [Pfefferkorn 84] G. E. Pfefferkorn. *The Early Days of Electron Microscopy*. Scanning Electron Microscopy, vol. 1, pp. 1–8, 1984.
- [Porrill 90] J. Porrill. *Fitting ellipses and predicting confidence envelopes using a bias corrected Kalman filter*. Image vision and computing, vol. 8, no. 1, pp. 1140–1153, 1990.
- [Postek 98] M. T. Postek & A. E. Vladar. *Image Sharpness Measurement in Scanning Electron Microscopy - Part I*. Scanning, vol. 20, pp. 1–9, 1998.
- [Prewett 84] P. D. Prewett. *Focused ion beam systems for materials analysis and modification*. Vacuum, vol. 34, no. 10-11, pp. 931–939, 1984.
- [Prewett 93] PD Prewett. *Focused ion beams—microfabrication methods and applications (invited)*. Vacuum, vol. 44, no. 3-4, pp. 345–351, 1993.
- [PTB 04] PTB. <http://www.nanoscale.de/standards.htm>, 2004.

- [Puretzt 92] J. Puretzt & L. W. Swanson. *Focused ion beam deposition of Pt containing films*. J. Vac. Sci. Technol. B, vol. 10, no. 6, pp. 2695–2698, 1992.
- [Regensburger 90] Karl Regensburger. *Photogrammetrie: Anwendungen in Wissenschaft und Technik*. VEB, Berlin, 1. edition, 1990.
- [Reimer 87a] L. Reimer, R. Böngeler & V. Desai. *Shape from Shading using multiple detector signals in Scanning Electron Microscopy*. Scanning Electron Microscopy, vol. 1, no. 3, pp. 963–973, 1987.
- [Reimer 87b] L. Reimer & D. Stelter. *Monte Carlo calculations of electron emission at surface edges*. Scanning Electron Microscopy, vol. 1, no. 3, pp. 951–962, 1987.
- [Reimer 98] L. Reimer. *Scanning Electron Microscopy. Physics of Image Formation and Microanalysis*. Springer Verlag, Berlin, 1998.
- [Ritter 05] M. Ritter & M. Hemmleb. *Geometrical Calibration of Dual Beam SEM and Accuracy of FIB Applications*. Technical report, FEI Company, Eindhoven, 2005.
- [Sänger 03] P. Sänger, M. Ritter & H. Hohenberg. *Water Reservoirs (Matrices) Prevent Rapid Dehydration of Native Samples in the Environmental Scanning Electron Microscopy (ESEM)*. In *Microscopy and Microanalysis. MC 2003*, volume 9, pp. 494–495, Dresden, 2003.
- [Schattenburg 02] Mark L. Schattenburg & Henry I. Smith. *The critical role of metrology in nanotechnology*. In Martin C. Peckerar, Michael T. Postek & Jr. (eds.), *Proceedings of SPIE*, volume 4608 of *Nanostructure Science, Metrology and Technology*, pp. 116–124. SPIE, 2002.
- [Schnarr 97] H. Schnarr & M. W. Fütting. *Some Aspects of Optimizing Contrasts for the Investigation of Joint Materials in the Environmental Scanning Electron Microscope*. Scanning, vol. 19, pp. 79–84, 1997.
- [Seiler 76] H. Seiler. *Determination of the Information Depth in SEM*. In *Scanning Electron Microsc: Proc. 9th SEM Symp.*, volume 1, pp. 9–16, IIT Institute, Chicago, 1976.
- [Sinram 02a] O. Sinram, M. Ritter, S. Kleindiek, A. Schertel, H. Hohenberg & J. Albertz. *Calibration of an SEM, using a nano positioning tilting table a microscopic calibration pyramid*. In *ISPRS Commission V Symposium 2002, Close-Range Vision Techniques*, Corfu Greece, pp. 210–215, 2002.
- [Sinram 02b] O. Sinram, M. Ritter, A. Schertel, H. Hohenberg & J. Albertz. *Ein neues Kalibrierobjekt für die Elektronenmikrophotogrammetrie*. *Photogrammetrie-Fernerkundung-Geoinformation*, no. 6, pp. 435–441, 2002.
- [Smith 97] S. W. Smith. *The Scientist and Engineer’s Guide to Digital Signal Processing*. California Technical Publishing, San Diego, 1997.
- [Stegmann 99] H. Stegmann, R. Wepf & R. R. Schröder. *Handbook of Computer Vision and Applications*, volume 1, chapter: *Electron Microscopic Image Acquisition*, pp. 347–385. Academic Press, San Diego, 1999.
- [Stevie 04a] F. A. Stevie, L. A. Gianuzzi & B. I. Prenitzer. *Introduction to Focused Ion Beams*, chapter: *The Focused Ion Beam Instrument*, pp. 1–12. Springer Science + Business Media Inc., New York, 2004.

- [Stevie 04b] F. A. Stevie, D. P. Griffis & P. E. Russell. Introduction to Focused Ion Beams, chapter: Focused Ion Beam Gases for Deposition and Enhanced Etch, pp. 53–72. Springer Science + Business Media Inc., New York, 2004.
- [Swanson 83] L. W. Swanson. *Liquid metal ion sources: mechanisms and applications*. Nuclear Instruments and Methods in Physics Research, vol. 218, pp. 347–353, 1983.
- [Tai 01] S.S. Tai & X.M. Tang. *Manipulating biological samples for environmental scanning electron microscopy observation*. Scanning, vol. 23, no. 4, pp. 267–72, 2001.
- [Tiziani 00] H. J. Tiziani, M. Wegner & D. Steudle. *Confocal principle for macro- and microscopic surface and defect analysis*. Optical Engineering, vol. 39, no. 1, pp. 32–39, 2000.
- [Tyrell 04] J. W. G. Tyrell, C. Dal Savio, R. Krüger-Sehm & H.-U. Danzebrink. *Development of a combined interference microscope objective and scanning probe microscope*. Review of Scientific Instruments, vol. 75, no. 4, pp. 1120–1126, 2004.
- [van den Heuvel 92] F. A. van den Heuvel, R. J. G. A. Kroon & R. S. Le Poole. *Digital Close Range Photogrammetry Using Artificial Targets*. In Int. Arch. of Photogrammetry and Remote Sensing, volume 29, pp. 222–229. ISPRS Commis. V., 1992.
- [Vieu 94] C. Vieu, G. Ben Assayag & J. Gierak. *Observation and simulation of focused ion beam induced damage*. Nuclear Instruments and Methods in Physics Research Section B: Beam Interactions with Materials and Atoms, vol. 93, no. 4, pp. 439–446, 1994.
- [Villarrubia 96] J. S. Villarrubia. *Scanned probe microscope tip characterization without calibrated tip characterizers*. Journal of Vacuum Science and Technology B, vol. 14, p. 1518, 1996.
- [Vladar 98] A. E. Vladar, M. T. Postek & M. P. Davidson. *Image Sharpness Measurement in Scanning Electron Microscopy - Part II*. Scanning, vol. 20, pp. 24–34, 1998.
- [Watt 85] I. M. Watt. The principles and practice of electron microscopy. Cambridge University Press, Cambridge, 1985.
- [Website 05] Website. <http://www.webelements.com>, 2005.
- [Wells 74] O. C. Wells. *Resolution of the Topographic Image in the SEM*. In Scanning Electron Microsc: Proc. 7th SEM Symp, volume 1, pp. 1–8, IIT Institute, Chicago, 1974.
- [Wendt 94] U. Wendt & D. Wagner. *Synergie von Rasterelektronenmikroskopie und konfokaler Laserrastermikroskopie bei Werkstoffuntersuchungen*. Beiträge zur Elektronenmikroskopischen Direktabbildung von Oberflächen (BEDO), vol. 27, pp. 113–116, 1994.
- [Wendt 02] U. Wendt, K. Stiebe-Lange & M. Smid. *On the influence of imaging conditions and algorithms on the quantification of surface topography*. Journal of Microscopy, vol. 207, no. Pt 3, pp. 169–79, 2002.
- [West 02] P. West & N. Starostina. *A Guide to AFM Image Artifacts*. Technical report, Pacific Nanotechnology, 3350 Scott Blvd. 29, Santa Clara, CA 95054, USA, 2002.

-
- [Wilkening 04] G. Wilkening. *Messtechnik für die Nanotechnologie - eine Herausforderung für die PTB*. PTB Mitteilungen, vol. 114, pp. 1–2, 2004.
- [Wilson 89] T. Wilson. *Techniques of optical scanning microscopy*. Journal of Physics E: Instrument Science and Technology, vol. 22, pp. 532–547, 1989.
- [Winkler 95] K. Winkler & W. Knebel. *Leica TCS 4D UV - Das Systemkonzept für die Multiparameter-Konfolalmikroskopie*. Mitteilungen für Wissenschaft und Technik, vol. 11, pp. 9–19, 1995.
- [Yamaguchi 85] H. Yamaguchi, A. Shimase, S. Haraichi & T. Miyauchi. *Characteristics of silicon removal by fine focused gallium ion beam*. J. Vac. Sci. Technol. B, vol. 3, no. 1, pp. 71–74, 1985.
- [Yan 02] H. Yan, D. Joy & M. Lei. *Convolution and Correlation: A Case Study of Scanning Imaging and Analysis Systems*. Scanning, vol. 24, pp. 6–17, 2002.
- [Yoshida 03] Wayne Yoshida & Yoram Cohen. *Topological AFM characterization of graft polymerized silica membranes*. Journal of Membrane Science, vol. 215, no. 1-2, pp. 249–264, 2003.
- [Yuen 89] H. K. Yuen, J. Illingworth & J. Kittler. *Detecting partially occluded ellipses using the Hough transform*. Pattern Recognition, vol. 7, no. 1, pp. 31–37, 1989.
- [Zhao 98] Xianbin Zhao. *Scanning Probe Microscope with High Resolution Capacitive Transducers*. Wirtschaftsverlag NW, Bremerhaven, 1998.
- [Zhou 86] G. Zhou. *Accurate determination of ellipse centers in digital imagery*. In ASPRS Annual Convention, volume 4, pp. 256–264, 1986.

ACKNOWLEDGEMENTS

Mein grösster Dank gilt meinen Eltern, die mich auf meinem Weg immer unterstützt und mir vertraut haben.

Dr. Heinrich Hohenberg, Leiter der Arbeitsgruppe Elektronenmikroskopie und Mikrotechnologie am Heinrich-Pette-Institut (HPI) in Hamburg danke ich ganz besonders für seine Betreuung, seine grosse Unterstützung, und für die Freiheit mit der ich meine wissenschaftlichen Weg verfolgen durfte. Auch möchte ich mich bei allen Mitarbeitern der Arbeitsgruppe am HPI bedanken. Es war eine bewegende und schöne Zeit.

Prof. Dr.-Ing. Olaf Hellwich hat sich sofort bereit erklärt, meinen Fachbereichswechsel zu den Ingenieurwissenschaften zu unterstützen, und die vorliegende Arbeit zu betreuen. Dafür möchte ich mich bedanken.

Ohne Dr.-Ing. Matthias Hemmleb wäre diese Arbeit nie entstanden. Für die andauernde, gute Zusammenarbeit, die fachliche Hilfe, die unzähligen Anregungen und Diskussionen, und die Freundschaft möchte ich mich herzlich bedanken.

Ein ganz spezieller Dank geht an Prof. Dr.-Ing. Jörg Albertz, der dieses interdisziplinäre Projekt von Anfang an und bis heute gefördert und mit grossem Interesse und fachlichem Rat unterstützt hat.

Danken möchte ich Herrn Dipl.-Ing. Olaf Sinram, für die gute und enge Zusammenarbeit im Rahmen des DFG Projektes "3D Rekonstruktion biologischer Oberflächen".

Weiterhin möchte ich mich bei Dr. Ludger Koenders und Dipl.-Phys. Thorsten Dziomba von der Arbeitsgruppe "Schichtdicke und Nanostrukturen" der Physikalisch-Technischen Bundesanstalt (PTB) in Braunschweig für die Referenzmessungen, den fachlichen Austausch und das grosse, und immer noch fortwährende Interesse an meiner Arbeit bedanken.

Ein weiterer Dank gilt Herrn Ben Lich und Dr. Pybe Faber von der Firma FEI Company, Eindhoven für die finanzielle Förderung und die fachliche Unterstützung zur Entwicklung der 3D Strukturen mittels der Focused Ion Beam Technologie (I am grateful to Mr. Ben Lich and Dr. Pybe Faber from FEI Company, Eindhoven for financial and professional support to develop the 3D calibration structures by focused ion beam technology). Nicht unerwähnt bleiben in diesem Zusammenhang soll Dr. Andreas Schertel, der die ersten Entwürfe der Mikrostrukturen herstellte.

Ganz besonders möchte ich mich auch für die kontinuierliche Unterstützung bei den Mitarbeitern, und insbesondere bei Dr. Roger Wepf, dem Leiter der Abteilung "Analytische Mikroskopie" der Firma Beiersdorf (BDF) in Hamburg bedanken.

Herrn Prof. Dr. Axel Kranzmann danke ich für die flexible Gestaltungsmöglichkeit meiner Arbeitszeit in der Fachgruppe V.1 der Bundesanstalt für Materialforschung und -prüfung, die es mir erlaubte, neben der Projektarbeit diese Dissertation zu schreiben.

Herrn Peter Voss ist das vielleicht nicht bewusst, aber ohne ihn gäbe es diese Arbeit in der vorliegenden Form gar nicht. Herr Voss hat mir die FIB Technologie überhaupt ins Bewusstsein gebracht. Vielen Dank!

Frau Dr. Eleanor Hoff hat die vorliegende Arbeit in Bezug auf die Korrektheit der englischen Sprache redigiert. Ihr verdanke ich nicht nur das Wissen, dass auch im englischen Kommas existieren, sondern auch eine brillante Entwirrung vieler verschrobener Satzkonstruktionen. (Dr. Eleanor Hoff not only corrected the manuscript but also provided a lot of help finding the right expressions and words. Thank you very much!).

Zu guter Letzt ein grosses Dankeschön an alle meine Freunde, die auch nach dem Verfassen dieser Doktorarbeit noch meine Freunde sind, und die in meinem Exil an mich gedacht haben.

CURRICULUM VITAE

Martin Ritter

Date and place of birth: 28.03.1970 in Grabs, Switzerland
Nationality: Principality of Liechtenstein

- 1977 - 1982 Volksschule Ruggell (primary school), Ruggell, Liechtenstein
- 1982 - 1990 Gymnasium Vaduz (secondary school), Vaduz, Liechtenstein
- 1990 - 1996 Student at the Swiss Federal Institute of Technology (ETH), Department of Biology, Zürich, Switzerland
- 1996 Diploma (Dipl. Natw. ETH), Swiss Federal Institute of Technology (ETH), Department of Biology, Zürich, Switzerland
- 1996 - 1997 IT consultant, Ingeno Computer AG, Zürich, Switzerland
- 1998 - 1999 Research Scientist in the DFG funded project “Cryo Electron Microscopy of cellular microstructures” at the Heinrich-Pette-Institute, Hamburg, Germany and Beiersdorf AG, Hamburg, Germany
- 2000 - 2003 Research Scientist in the partly DFG funded project “Photogrammetric surface reconstruction of biological SEM data” at the Heinrich-Pette-Institute, Hamburg, Germany
- 2001 - 2004 Partner of the IT services company *m2c GbR*, Hamburg, Germany
- since 2003 Doctoral candidate at the faculty VI, TU Berlin, Germany
- 2004 Research Scientist in the FEI Company funded project “Calibration of a Nova DualBeam” at the Heinrich-Pette-Institute, Hamburg, Germany
- since 2005 Research Scientist in the DFG funded project “Microcalibration structures” at the Federal Institute for Materials Research and Testing (BAM), Berlin, Germany